Research Square

Preprints are preliminary reports that have not undergone peer review.
They should not be considered conclusive, used to inform clinical practice,
or referenced by the media as validated information.

An iron-KDM3A-H3K9me2 circuit sustains stem-like prostate cancer and exposes NRF2- dependent ferroptosis vulnerability

Wanli Cheng
University of Bern
Andrea Brunello
University of Bern
Francesco Bonollo
University of Bern
Thomas Michael Marti
Inselspital, Bern University Hospital
Panagiotis Chouvardas
University of Bern
David P Labbé
McGill University
Marta Menna
University of Bern
George Thalmann
University of Bern
Beat Roth
University of Bern
Sofia Karkampouna
University of Bern
Marianna Kruithof-de Julio
marianna.kruithofdejulio@unibe.ch
University of Bern

Research Article

Keywords: Iron metabolism, Epigenetic Modification, Ferroptosis, CRPC

Posted Date: November 25th, 2026

DOI: https://doi.org/10.21203/rs.3.rs-11760152/v1

License: This work is licensed under a Creative Commons Attribution 4.0 International License.
Read Full License

Additional Declarations: No competing interests reported.

An iron-KDM3A-H3K9me2 circuit sustains stem-like prostate cancer and exposes NRF2-dependent ferroptosis vulnerability

Wanli Cheng[1,2], Andrea Brunello[1,2], Francesco Bonollo[1], Thomas Michael Marti[3,4], Panagiotis Chouvardas[1,7], David P Labbé[5,6], Marta De Menna[1,2], George Thalmann[1,7], Beat Roth[7], Sofia Karkampouna[1,7], Marianna Kruithof-de Julio[1,2,7]

[1] Department for Biomedical Research, Urology Research Laboratory, University of Bern, Switzerland
[2] Translational Organoid Resource, Department for BioMedical Research, University of Bern, Bern, Switzerland
[3] Department of General Thoracic Surgery, Inselspital, Bern University Hospital, Bern, Switzerland
[4] Department for BioMedical Research, University of Bern, Bern, Switzerland.
[5] Cancer Research Program, Research Institute of the McGill University Health Centre, Montréal, Québec, Canada
[6] Division of Urology, Department of Surgery, McGill University, Montréal, Québec, Canada
[7] Department of Urology, Inselspital, Bern University Hospital, University of Bern, Switzerland

Corresponding author: Marianna Kruithof-de Julio
marianna.kruithofdejulio@unibe.ch

Key words: Iron metabolism, Epigenetic Modification, Ferroptosis, CRPC

Abstract

Stem cell-like castration-resistant prostate cancer (CRPC-SCL) is an aggressive CRPC subtype enriched for CD44 expression with limited responsiveness to androgen deprivation therapy, yet the mechanisms that maintain this state and create therapeutic vulnerabilities remain unclear. Here, we identify an iron-loaded tumor-cell state that couples epigenetic maintenance of CRPC-SCL identity to an increased reliance on NRF2-mediated ferroptosis defense. CD44hi cells exhibited elevated intracellular labile iron and reduced H3K9me2, forming an iron-dependent epigenetic state that supported enhanced tumorigenic fitness. Mechanistically, CD44-associated iron accumulation supported the activity of the H3K9me2 demethylase KDM3A, promoting KDM3A-dependent H3K9me2 remodeling at the CD44 locus, sustaining CD44 expression and supporting a self-reinforcing regulatory circuit. Iron chelation and KDM3A inhibition suppressed MYC-associated stem-like transcriptional programs, and impaired organoid growth, whereas genetic KDM3A depletion increased H3K9me2 and reduced CD44 expression. The same iron-loaded state engaged NRF2-mediated ferroptosis defense, in part through KDM3A-dependent H3K9me2 remodeling at the NRF2 locus, enabling CD44hi cells to tolerate iron-associated lipid peroxidative stress. Genetic NRF2 depletion preferentially increased ferroptotic stress and sensitized CD44hi cells to ferroptosis induction, whereas pharmacological disruption of NRF2-associated defense with Brusatol increased labile iron, lipid peroxidation and promoted ferroptosis-associated cell death in cellular models, while reducing LAPC9 tumor growth and increasing lipid peroxidation in vivo. CRPC single-cell analyses supported the presence of a CD44-associated iron/NRF2 transcriptional program, while a related multigene FerroScore showed prognostic associations in prostate cancer cohorts. Together, these findings support a dual role for iron in maintaining the CD44-associated CRPC-SCL state while increasing reliance on NRF2-mediated ferroptosis defense, revealing a potential therapeutic vulnerability.

Introduction

Prostate cancer (PCa) is the second most common cancer among men worldwide [1]. Androgen deprivation therapy (ADT) remains the cornerstone of treatment for advanced disease, but resistance inevitably develops, leading to castration-resistant prostate cancer (CRPC), an aggressive and lethal disease stage [2,3]. Although CRPC has traditionally been studied through the lens of androgen receptor (AR) signaling, recent chromatin profiling studies have revealed substantial molecular heterogeneity and stratified CRPC into distinct subtypes, including AR-driven, Wnt-driven, neuroendocrine, and stem cell-like states [4]. Among these, the stem cell-like subtype (CRPC-SCL) accounts for approximately 30% of CRPC cases and is characterized by reduced responsiveness to ADT and aggressive clinical behavior [4]. However, the molecular mechanisms that sustain this subtype and whether they create actionable therapeutic vulnerabilities remain poorly understood.

CD44, a cell-surface glycoprotein that mediates hyaluronic acid (HA) binding and uptake, is enriched in CRPC-SCL and has been proposed as a marker of this subtype [4,5]. CD44 has been extensively characterized as a marker and functional regulator of stem-like prostate cancer cells. Previous studies have shown that CD44-positive populations are enriched for clonogenic and tumorigenic properties, can persist following androgen deprivation, and contribute to prostate cancer progression and castration resistance [6-15]. More recently, CD44 was identified as a prominent feature of the CRPC-SCL transcriptional state [4]. Thus, rather than redefining CD44 as a stem-cell marker, we sought to determine how the CD44-associated state is maintained and whether this biology creates a therapeutically exploitable vulnerability. CD44-mediated HA uptake can facilitate iron entry into cancer cells, linking CD44-associated states to intracellular iron availability [16]. Iron is essential for tumor growth and metabolism, and it also serves as a cofactor for Jumonji C domain-containing histone demethylases, thereby connecting iron metabolism to chromatin remodeling and transcriptional plasticity [17,18]. At the same time, elevated intracellular iron can promote lipid peroxidation and ferroptosis, an iron-dependent form of regulated cell death that has emerged as a therapeutic vulnerability in prostate cancer [19,20]. Thus, CD44-associated tumor states may sit at the intersection of iron metabolism, epigenetic regulation, and ferroptosis control. Whether iron-dependent chromatin regulation maintains the transcriptional identity of CD44hi CRPC-SCL cells while coordinating protection from iron-associated ferroptotic stress remains unknown.

Here, we identify an iron-rich epigenetic state that supports maintenance of the CD44-associated tumor cell state in CRPC-SCL. Mechanistically, CD44-associated iron accumulation promotes KDM3A-dependent H3K9me2 remodeling at the CD44 locus, supporting a self-reinforcing circuit that maintains CD44 expression and contributes to the associated stem-like transcriptional program. This same iron-loaded state is coupled to NRF2-mediated ferroptosis defense, and disruption of this adaptive protection preferentially sensitizes CD44hi cells to ferroptotic stress and suppresses SCL-associated model LAPC9 tumor growth in vivo.

Methods

Bioinformatics analysis

Public CRPC single-cell RNA-seq datasets were obtained from GEO, including GSE137829 and GSE210358. Seven CRPC patient samples were included for patient-wise correlation analysis, consisting of four samples from GSE137829 and three samples from GSE210358. Sample identifiers are listed in **Supplementary Table 1**. Processed gene-cell count matrices were analyzed using Seurat. Low-quality cells were excluded by retaining cells with 200-6,000 detected genes and <10% mitochondrial gene expression. Data were normalized using LogNormalize, followed by variable feature selection, scaling, PCA, UMAP dimensionality reduction, and graph-based clustering. Major cell types were annotated using SingleR and canonical lineage markers. Epithelial cells were selected for downstream analysis and re-analyzed to visualize tumor-cell heterogeneity. CD44 expression and SCL signature scores were visualized using FeaturePlot, DotPlot, and module score analysis. For GSE210358, tumor cell annotations provided by the original study were used. For GSE137829, analyses were restricted to the epithelial compartment because malignant identity could not be unambiguously assigned to all epithelial cells. Samples were included in the within-patient correlation analysis only when sufficient CD44-expressing cells were present for robust evaluation, samples with predominantly CD44-negative epithelial populations were excluded. Seven patient samples met these criteria.

Gene signature scores for SCL, iron metabolism, NRF2 activity, AR, Wnt, and neuroendocrine programs were calculated using Seurat AddModuleScore or equivalent gene set scoring approaches based on gene sets listed in **Supplementary Table 2**. The genes included in FerroScore were selected from components associated with the CD44/iron/KDM3A/NRF2-related network investigated in this study, whereas FerroScore itself was developed as a multigene prognostic model rather than a measure of pathway activity. The neuroendocrine signature was expanded to include canonical neuroendocrine markers. CD44 was excluded from the iron score to avoid circularity. For single-cell correlation analysis, Spearman correlations between CD44 expression and iron or NRF2 scores were calculated independently within epithelial cells from each patient sample to avoid correlations driven by inter-patient differences or non-tumor cell composition. Correlation coefficients and significance values were summarized using bubble plots.

Bulk RNA-seq data were aligned to the human reference genome GRCh38 using STAR, and gene-level counts were quantified using featureCounts. Differential expression analysis was performed in R using DESeq2, with adjusted $P < 0.05$ and $|\log2 \text{ fold change}| \geq 1$ used to define significantly differentially expressed genes. Pathway enrichment and GSEA were performed using clusterProfiler with Gene Ontology, KEGG, Reactome, and MSigDB Hallmark gene sets. Master regulator analysis was performed using VIPER. Data visualization was performed using ggplot2 and EnhancedVolcano. To assess whether the inverse pathway relationship was driven primarily by proliferation-associated changes, the Hallmark gene sets E2F Targets, G2M Checkpoint, MYC Targets V1, MYC Targets V2, Mitotic Spindle, and

mTORC1 Signaling were excluded before correlation analysis. Pearson correlation was then performed between the normalized enrichment scores (NES) from the CD44hi versus CD44low comparison and those from DFO or CBA-1 treated versus control organoids across the remaining Hallmark pathways.

For patient cohort analyses, gene expression and clinical annotations were obtained from TCGA-PRAD, the DKFZ prostate cancer cohort, and the SU2C/PCF metastatic CRPC cohort. Expression data were normalized as TPM and log2-transformed for downstream analyses. Spearman correlation analysis was used to assess associations between SCL score and CD44, iron score, KDM3A, or NFE2L2/NRF2 expression. The SCL signature consisted of FOSL2, CD44, ATF3, ATXN1, and TACSTD2, whereas the iron-related signature consisted of FTH1, HMOX1, TFRC, SLC40A1, CD44, NCOA4, and HAMP. To avoid mathematical circularity in analyses directly involving CD44 expression, CD44 was excluded from both signatures. The resulting CD44-independent SCL score comprised FOSL2, ATF3, ATXN1, and TACSTD2, and the CD44-independent iron score comprised FTH1, HMOX1, TFRC, SLC40A1, NCOA4, and HAMP. These CD44-independent scores were used for the relevant correlation analyses and shown in **Supplementary Table 3**.

A seven-gene FerroScore was developed in the TCGA-PRAD cohort using CD44, FTL, FTH1, SLC11A2, HMOX1, NFE2L2, and KDM3A. Gene-expression values were z-score standardized within each cohort before score calculation to harmonize expression scales across datasets. All seven genes were entered simultaneously into a Cox proportional-hazards model for biochemical recurrence, and the resulting regression coefficients were used to calculate the weighted FerroScore in **Supplementary Table 4**.

$$\text{FerroScore} = -0.103570 \times \text{CD44} - 0.412366 \times \text{FTL} + 0.196701 \times \text{FTH1} - 0.772861 \times \text{SLC11A2} + 0.478134 \times \text{HMOX1} - 0.986267 \times \text{NFE2L2} + 1.186945 \times \text{KDM3A}$$

FerroScore was developed as a multigene prognostic signature derived from genes associated with the iron/NRF2-related network investigated in this study, rather than as a direct measure of CD44 or NRF2 activity. Because all seven genes were entered simultaneously, the resulting coefficients are adjusted, conditional estimates within a collinear gene set and do not represent the marginal association of any individual gene with outcome, the sign of an individual coefficient therefore cannot be interpreted as the direction of that gene's univariable effect. The coefficients were fixed after model development in TCGA and were not re-estimated in the validation cohort. Expression values were standardized (z-scored) within each cohort before the locked coefficients were applied, using the same transformation in TCGA and DKFZ. For external validation, the locked TCGA-derived formula was applied unchanged to the independent DKFZ cohort. FerroScore was evaluated as a dichotomous variable, with patients stratified into FerroScore-high and FerroScore-low groups using the cohort-specific median as the cutoff. Hazard ratios and 95% confidence intervals were reported for the high versus low groups. FerroScore was additionally evaluated as a continuous variable in Cox regression as a complementary sensitivity analysis, TCGA

(HR 1.06, 95% CI 0.93–1.19, P = 0.395), DKFZ (HR 2.11, 95% CI 1.41–3.15, P < 0.001). Multivariable models in TCGA and DKFZ included FerroScore together with Gleason grade, PSA level, age, and T stage. Hazard ratios (HRs) and 95% confidence intervals (CIs) were reported.

Multivariable Cox proportional-hazards analyses were performed with FerroScore together with Gleason grade, PSA level, age, and T stage to assess whether FerroScore was independently associated with biochemical recurrence.

The same locked TCGA-derived formula was also applied to the SU2C metastatic CRPC cohort using overall survival as the endpoint. Because this score was not significantly associated with overall survival, the SU2C analysis was considered exploratory. In a separate exploratory analysis, the same seven-gene panel was re-fitted within SU2C using overall survival as the endpoint, this cohort-specific model was not considered an external validation of the TCGA-derived FerroScore.

Cell line culture

Human osteotropic PCa PC-3M-Pro4-luc2 [21] and 22Rv1 cells [22] were maintained as described previously [23]. PC-3M-Pro4-luc2, PC3-shCD44 and PC3-shCD44-GFP cells cultured in media (Dulbecco's modified Eagle's medium with 10% fetal calf serum II and 1% penicillin–streptomycin). 22Rv1, 22Rv1-CD44hi, 22Rv1-shCD44 and 22Rv1-shCD44-GFP cultured in media (RPMI 1640 with 10% fetal calf serum, 1% penicillin–streptomycin and 1% L-glutamate). Cells were maintained at 37 °C with 5% CO2.

Reagent conditions

BODIPY 581/591 C11 (C11-BODIPY, ThermoFisher Scientific, D3861, 10uM, 30min), Brusatol (Sigma-Aldrich, SML1868), Deferoxamine (DFO, Sigma-Aldrich, D9533, 1-60uM depending on assay), FerrOrange (Dojindo, NC1808697, 1uM, 30min), Iron(III) nitrate (Fe(NO3)3·9H2O (5uM, 72h), Liproxstatin-1 (Sigma, SML1414-5MG, 5 μM, 24h). CBA-1 (ProbChem, PC-20353, 1-50uM depending on assay), IOX1 (Medchem, HY-12304, 30-150uM depending on assay), apo-transferrin (Merck, T2036-100MG, 3ug/ml, 48h) and holo-transferrin (Merck, T0665-50MG, 3ug/ml, 48h). Reagent concentrations and treatment durations varied according to the experimental model and assay. The complete assay-specific conditions for DFO and CBA-1 are provided in **Supplementary Table 5**.

Cell viability

Cell viability was evaluated by plating 20,000 cells/well in 96-well plates (Corning, 3595-50ea) using the PrestoBlue viability assay according to the PrestoBlue Cell Viability protocol. Cells were treated with different concentrations of Brusatol as indicated for 72 h. PrestoBlue reagent (ThermoFisher, P50201) was added after 72 h treatment and cells were incubated for 1 h before recording fluorescence intensities (ex. 560 nm; em. 590 nm) using a Varioskan Lux Microplate Reader.

Colony formation assay

Cells were pretreated with DMSO, DFO, or CBA-1 as indicated and seeded at low

density in 6-well plates (Sarstedt, 833.920.300). Colonies were allowed to form for the indicated duration, fixed, and stained with crystal violet. Colony numbers were quantified using ImageJ.

Flow Cytometry and cell sorting

Single cells obtained from digested tissues or cell lines were washed using FACS buffer (0.5% BSA, 2 mM EDTA in PBS, pH 7.4). The cells were then resuspended in 100 µl of FACS buffer containing anti-CD44-APC (1:20 dilution, BD Biosciences, clone G515) and incubated for 30 minutes in the dark at room temperature. Following incubation, the cells were washed again with FACS buffer and resuspended in 500 µl of FACS buffer per tube. The suspension was supplemented with DAPI at a final concentration of 5 µg/mL and kept on ice until analysis. FACS analysis were conducted using a BD LSRII flow cytometer (BD Biosciences), whereas cell sorting was performed using a MoFlo Astrios cell sorter (Beckman Coulter Life Sciences). Cells were gated sequentially to exclude debris, doublets, and DAPI-positive cells, followed by selection of CD44hi and CD44low populations according to CD44 fluorescence intensity. Representative gating strategies for LAPC9 and 22Rv1 cells are shown in Supplementary Figure 1D and Supplementary Figure 3E, respectively.

Generation of GFP-Luciferase-labelled PDX models

For the generation of GFP-Luciferase labeled LAPC9 PDX models, MACS-purified LAPC9 human (tumor) single cells were seeded in collagen-coated plates (rat collagen 0.3mg/ml, R&D Systems, 3447-020-01) and transduced with GFP-Luc lentiviral vectors (ATG-2460; copGFP-click beetle luciferase) at a multiplicity of infection (MOI) of 1. After 2 days, LAPC9-copGFP-luc tumor cells were transferred in 3D culture conditions to allow organoid formation. Once formed, organoids were resuspended in Matrigel (Corning) and subcutaneously injected into mice (under anesthesia). Tumor growth was monitored through the IVIS Imaging System (PerkinElmer) following intraperitoneal injection of D-sodium salt luciferin (150mg/kg). To deplete potential non-transduced tumor cells, the newly generated LAPC9-copGFP-Luc tumors were collected at the endpoint, digested, and FACS was performed to select the GFP+ cells. FACS-purified GFP+ cells were then re-injected subcutaneously into new mouse hosts.

Organoid Culture

Tissues were collected in a basic medium [Advanced D-MEM/F-12 (ThermoFisher Scientific) supplemented with 1 ml Primocin (Invivogen), 1% GlutaMAX, and 10 mM HEPES (ThermoFisher Scientific)]. The tissues were finely minced with a scalpel and incubated at 37°C in a solution containing 5 mg/ml collagenase type II (Gibco), 15 µg/ml DNase I (Sigma-Aldrich), and 10 mM Y-27632, with occasional mixing for 1–3 hours until fully digested. The resulting cell suspension was centrifuged at 700 rcf for 5 minutes and washed with the basic medium. The cell pellet was subsequently incubated at 37°C in 2 ml of TripLE Express (ThermoFisher Scientific) for 15 minutes, with pipetting every 5 minutes to aid digestion. The digested suspension was passed through a 50 µm-pore size strainer (Celltrics, Sysmex) and washed with the basic

medium. When necessary, cells were treated with erythrocyte-lysing buffer for 5 minutes to remove red blood cells, followed by another wash with the basic medium. Cell counting was performed using trypan blue and an automated cell counter (TC20, Bio-Rad). Afterward, cells were centrifuged and resuspended in complete prostate cancer organoid medium (prepared as described previously [24]) at a concentration of 500,000 cells/ml. The suspension was seeded at a volume of 1.5 ml per well in 6-well ultra-low attachment plates (ULA plates, Corning). Fresh medium was added every 2–3 days until the organoids were ready for downstream applications.

LAPC9, PCa16, PM154, and BM18 patient-derived prostate cancer models were obtained from Rubin lab and have been previously described [4,24 ,25]. LAPC9 was used as an SCL-associated model, PCa16 as a Wnt-driven model, PM154 as a neuroendocrine model, and BM18 as an androgen-dependent model.

For LAPC9 and BM18, dissociated tumor cells were cultured in complete prostate cancer organoid medium in ultra-low-attachment plates as described above. PCa16 and PM154 organoids were maintained in growth factor-reduced Matrigel using established human prostate organoid culture conditions as previously described [4]. Organoids were cultured in Advanced DMEM/F12-based organoid medium supplemented with B27, N-acetylcysteine, EGF, FGF10, FGF2, A83-01, SB202190, nicotinamide, DHT, PGE2, Noggin, and R-spondin, with medium refreshed every 3 days.

Organoid drug treatment and viability assay

Organoids were dissociated into single cells and seeded in Matrigel or ultra-low attachment plates as indicated. After organoid formation, cultures were treated with DMSO, DFO, CBA-1, or Brusatol at the concentrations and durations indicated in the figure legends. For cross-model Brusatol sensitivity assays, organoids were cultured under the corresponding 3D conditions and treated with the indicated Brusatol concentrations for 48 h. N-acetylcysteine (NAC) was omitted from the treatment medium during these experiments to avoid antioxidant interference with ferroptosis-associated oxidative stress. Organoid measurements were obtained from three independent biological experiments. Multiple organoids were quantified within each experiment, and the mean value for each independent experiment was used as the statistical unit. Statistical comparisons were therefore performed using n=3 biological replicates. Organoid size was quantified from bright-field images using ImageJ. Organoid viability was measured using CellTiter-Glo 3D according to the manufacturer’s instructions, as indicated for each experiment.

Ex vivo Tissue Culture

Freshly harvested LAPC9 tissues were aseptically cut into 1 mm-thick serial slices. These tissue slices were then carefully positioned on the membrane of a 0.4 μM pore polypropylene 6-well transwell (ThinCert, Grainer Bio-one International) and cultured in 1.5 ml of DMEM supplemented with 10% FBS, 1% penicillin/streptomycin, and the specified compound at 37°C for 4 days. Before incubation, the plate containing the tissue slices was placed inside a sealed chamber and flushed with oxygen (3 L/min)

for 3 minutes. After 4 days of culture, the tissues were collected and processed for flow cytometry analysis and Western blot.

Western Blot

Cells were lysed in RIPA buffer (50 mM Tris-HCl pH 8.0, 100 mM NaCl, 5 mM EDTA, 0.2% SDS, 0.5% sodium deoxycholate, 1% Triton-X100) supplemented with protease and phosphatase inhibitors (cOmplete Mini protease inhibitor cocktail and PhosStop, both from Merck Millipore). Tissue samples were homogenized in RIPA buffer using a metallic bead and the TissueLyser II (Qiagen) for 1 cycle of 2 minutes at 20 Hz. Organoids were resuspended in 150 µl of RIPA buffer and homogenized with a 0.3 ml syringe. Homogenized samples were centrifuged at >16,000 g for 15 minutes at 4°C, and the supernatants were collected. Protein concentrations were determined using the Bradford assay, and 10–30 µg of each sample was loaded for SDS-PAGE. Proteins were then transferred onto Immobilon-PVDF membranes (Millipore). Blots were incubated overnight with primary antibodies, followed by washing with PBS-Tween (refer to **Supplementary Table 6** for details on the antibodies used). The blots were then incubated with either anti-mouse or anti-rabbit secondary antibodies. After additional PBS-Tween washes, the proteins were visualized using the Supersignal ECL detection kit (ThermoFisher) and imaged with the Amersham Imager 600 (GE).

Western blot quantifications

Western blot signals were quantified using ImageJ. Equal areas were defined for each lane and quantified using the Plot Lanes function in ImageJ. Signals arising from individual antibodies were normalized against the antibody signal of the loading control.

RNA isolation and real-time quantitative PCR

Total RNA was extracted using Trizol Reagent (Invitrogen), and cDNA was synthesized via reverse transcription following the manufacturer's protocol (Promega). For qPCR analysis, 10 ng of cDNA per reaction was amplified using the CFX Real-Time Detection System (Bio-Rad, Cressier, Switzerland) with SYBR Green Supermix reagent (BioRad). Gene expression levels were normalized to the reference transcripts HPRT and ACTB. The primer sequences used for the reactions are provided in **Supplementary Table 7.**

Suppressing CD44 with shRNAs

shRNA for CD44 (TRCN0000296191, TRCN0000289233 and TRCN0000308110) were obtained from Sigma's MISSION library and shRNA for CD44 with eGFP was from Addgene (Plasmid#9123). Lentiviral infection and selection were performed as described previously [23]. Stable shCD44 cells were used as genetically CD44-depleted derivatives of the corresponding CD44hi cells and were not considered equivalent to naturally occurring or FACS sorted CD44low populations. In all shRNA-mediated knockdown experiments, cells transduced with a non-targeting control shRNA (shCTR) were used as the corresponding control.

Suppressing KDM3A with shRNAs

shRNA for KDM3A (TRCN0000021149, TRCN0000329992 and TRCN0000329990) were obtained from Sigma's MISSION library. Lentiviral infection and selection were performed as described previously [23].

Suppressing NRF2 with shRNAs

shRNA for NRF2 (TRCN0000007555, TRCN0000007558 and TRCN0000273494) were obtained from Sigma's MISSION library. Lentiviral infection and selection were performed as described previously [23].

Bulk RNA barcoding and sequencing (BRB-seq)

Bulk transcriptomic analysis was conducted on sorted LAPC9 CD44hi and CD44low cells (n=5 biological replicates/condition) and on LAPC9 organoid treated with DMSO, DFO or CBA-1 (n=4 biological replicates/condition). RNA was extracted using Alithea Isolation Reagent. Only RNA samples with quantities between 200 ng and 1000 ng, and an RNA Integrity Number (RIN) greater than 6, were included. The samples were then sent to Alithea Genomics SA (Lausanne, Switzerland) for library preparation and sequencing. For prostate tissue samples, highly multiplexed 3'-end bulk RNA barcoding and sequencing (MERCURIUS™ BRB-seq) was used, while for organoids, extraction-free MERCURIUS™ BRB-seq was utilized. Library preparation followed the manufacturer's protocol for the MERCURIUS™ BRB-seq (organoids) kits for Illumina sequencing. Sequencing was performed on the Illumina NovaSeq 6000 platform. RNA-seq raw counts were analyzed using DESeq2, with genes retained if they had at least 3 UMI counts in at least 3 samples. Differential gene expression was determined using an adjusted p-value threshold of 0.05. Functional enrichment analysis was performed using Enrichr.

Immunohistochemistry (IHC) Stainings

Sections, 4 µm thick, were cut from FFPE blocks, stained with hematoxylin and eosin (H&E), and mounted using Entellan (Merck Millipore). For CD44 staining, the sections underwent antigen retrieval by heating in a pressure cooker for 10 minutes in citrate buffer (pH 6.0). After cooling, sections were thoroughly washed under running water. To block endogenous peroxidases, sections were incubated with 3% H2O2 at room temperature for 15 minutes, followed by two washes with PBS. Blocking was then performed using a 3% BSA solution in PBS-Tween 20 (0.1%, PBS-T) for 1 hour at room temperature. The sections were subsequently incubated overnight with 100 µl of primary antibody or IgG as a control, as listed in **Supplementary Table 8**. After overnight incubation, the sections were washed once with PBS-T and twice with PBS. They were then incubated with 100 µl of EnVision anti-mouse reagent (Agilent Technologies) for 30 minutes. Following this, sections were again washed once with PBS-T and twice with PBS before development in freshly prepared AEC solution (Dako) until the desired signal was achieved. The sections were washed with water, counterstained with hematoxylin, and mounted with Entellan. Finally, slides were digitized using the Pannoramic 250 Flash III slide scanner (3D Histech).

Immunofluorescence (IF) Staining

FFPE sections (4 μm) were deparaffinized and rehydrated using xylene and ethanol. Antigen retrieval was performed with either a citrate-based buffer (pH 6) (Adipogen, H-3300) or a 10 mM Tris (pH 9)/1 mM EDTA/0.05% Tween buffer. The slides were blocked in a blocking solution (10% donkey serum, 0.1% PBS-Tween or 1% BSA, 0.1% PBS-Tween) for 1 hour at room temperature (RT), followed by overnight incubation at 4°C with primary antibodies (**Supplementary Table 8**). Secondary antibodies (anti-rabbit/mouse/goat) conjugated to Alexa Fluor®-647, -555, -488 fluorochromes (Life Technologies) were applied for 90 minutes at a 1:250 dilution in the blocking solution. Sections were then counterstained with DAPI (1 μg/ml, ThermoFisher, 62248) for 10 minutes, washed, and mounted with Prolonged Diamond Antifade reagent (ThermoFisher, P36970). Immunofluorescence images were captured using a CellVoyager CQ1 microscope (Yokogawa) and a slide scanner (3DHistech Panoramic 250 Flash II).

Iron measurement

Intracellular chelatable iron was determined using the fluorescent probe FerroOrange from Dojindo (F374). FerroOrange is a fluorescent probe that enables live-cell fluorescence imaging of intracellular Fe2+. Cells were incubated with 1 μM for 30 min, and data were captured using FACS at PE laser.

Lipid peroxidation assay

C11-BODIPY581/591 dye (Thermo Fisher Scientific, D3861) was used to detect lipid peroxidation in live cells. For flow cytometry, 500,000 cells were seeded in 6-well plates and allowed to adhere overnight at 37°C. Then, cells were treated with dimethyl sulfoxide (DMSO) or Brusatol (0.1uM) for 24 hours. Cells were then trypsinized, washed, suspended in Hanks' balanced salt solution (HBSS) containing 2uM C11-BODIPY581/591, and incubated at 37°C for 15 min. Cells were pelleted and resuspended in HBSS. Oxidation of the polyunsaturated butadienyl portion of the dye results in a shift of the fluorescence emission peak from 590 nm to 510nm.

Chromatin Immunoprecipitation (ChIP) and qPCR

Chromatin immunoprecipitation (ChIP) was performed using a protocol modified from Silva et al. [26]. Briefly, cells were crosslinked with 1% formaldehyde for 8 minutes at room temperature, followed by quenching with 125 mM glycine for 5 minutes. Samples were washed with cold PBS and lysed to obtain nuclei. Chromatin was fragmented by sonication to an average size of 200-500 bp. For each immunoprecipitation, equal amounts of chromatin were incubated overnight at 4°C with H3K9me2 antibody [Cell signaling, 4658S, 1:100], KDM3A antibody [Proteintech, 12835-1-AP, 1:100] or normal Rbt IgG as a negative control. Antibody-chromatin complexes were captured using protein A/G magnetic beads, washed sequentially with low-salt, high-salt, LiCl, and TE buffers, and eluted according to kit instructions. Crosslinks were reversed at 65°C for 4 hours, followed by treatment with RNase A and proteinase K. DNA was purified using spin columns.

Purified ChIP DNA was analyzed by quantitative PCR (qPCR) using SYBR Green Master Mix (BioRad). Primers were designed to amplify target promoter or enhancer regions of interest, with input DNA used for normalization. Data were expressed as percent input or fold enrichment over IgG using the △Ct method. ChIP-qPCR experiments were independently repeated three times with consistent directional results. Representative data from one independent ChIP experiment are shown, with qPCR measurements performed in technical triplicate.

Animals Maintenance and in vivo Experiment

Animal experiments were carried out in accordance with Bern cantonal guidelines. Mice had unrestricted access to food and fresh water and were housed with a maximum of 5 animals per cage. For xenograft surgery, six 5-week-old male CB17/SCID mice were anesthetized via subcutaneous injection with a cocktail of medetomidine (Dorbene) 1 mg/kg, midazolam (Dormicum) 10 mg/kg, and fentanyl 0.1 mg/kg. Under sterile conditions, the sorted LAPC9 cells were grouped into 2 categories: GFP+ CD44hi, GFP+ CD44low. A total of 100,000 single cells were suspended in 50 µl of Matrigel and injected subcutaneously into the mice. Anesthesia was reversed by subcutaneous injection of atipamezol (Revertor R) 2.5 mg/kg and flumazenil (Anexate R) 0.5 mg/kg, along with buprenorphine (Temgesic) 0.1 mg/kg for analgesia. The sutured wound was disinfected using an iodopovidone solution. Mice were monitored twice a week for changes in body weight, tumor size, and any signs of acute toxicity. Tumor size was assessed by palpation and compared to standardized size beads to minimize discomfort during the experiment. Mice were euthanized as soon as signs of acute toxicity were observed or when the tumor size reached 8 mm.

The tumor growth was monitored by using an in vivo imaging system equipped with integrated micro-CT (IVIS-CT). Mice were anesthetized with 3% isoflurane in oxygen and maintained under anesthesia throughout image acquisition. Prior to imaging, animals received an intraperitoneal injection of D-luciferin potassium salt (150 mg/kg) dissolved in sterile PBS. Imaging was initiated 15 minutes post-injection to capture peak bioluminescent signal. Images were analyzed using Living Image software. Regions of interest (ROIs) were manually drawn over the site of luciferase expression, and corresponding signals were quantified as total flux (photons/sec) after background subtraction. CT images were used for anatomical reference and to ensure accurate ROI placement. Longitudinal tumor-growth data were analyzed using a mixed-effects model with treatment/group and time as fixed effects and repeated measurements from the same mouse accounted for within the model. Multiple-comparison testing was performed as indicated in the corresponding figure legends.

Ten CB17/SCID mice were subcutaneously implanted with LAPC9-GFP tumor pieces. One week after tumor implantation, mice were randomly assigned to vehicle or Brusatol treatment groups. Brusatol was administered intraperitoneally at 2 mg/kg every other day for 2 weeks. A 10 mM Brusatol stock prepared in DMSO was diluted in PBS to 0.4 mg/mL (approximately 7.7% DMSO), and mice received 5 µL/g body weight. Control mice received the matched DMSO/PBS vehicle at the same volume and schedule. Tumor progression was monitored using an IVIS-CT imaging system,

and bioluminescent signal intensity was used to assess tumor growth longitudinally. IVIS ROI definition and signal quantification were likewise performed with treatment allocation masked. When tumors reached 8 mm in diameter, all mice were euthanized and tumors were excised. Tumor size and tumor weight were measured immediately after collection. Tumors were implanted bilaterally, however, not all implantation sites formed measurable tumors. Thus, five tumors were collected from five vehicle-treated mice and seven tumors from five Brusatol-treated mice. For endpoint comparisons, tumor measurements were summarized at the mouse level to avoid treating multiple tumors from the same animal as independent biological replicates. Histological sections were coded before analysis, and staining quantification was performed with treatment allocation masked. No formal a priori power calculation was performed and group sizes were based on the approved animal protocol and prior xenograft experience.

Statistical analysis

Statistical analyses were conducted using Kaplan-Meier (K-M) analysis, unpaired t-test, chi-square test, one-way ANOVA, and two-way ANOVA with multiple comparison testing, as specified in each figure legend. All statistical analyses and data visualizations were performed using GraphPad Prism 10 software (GraphPad Software Inc.) or RStudio version 2026.09.1, unless otherwise noted. Data are expressed as mean ± SD from at least three independent experiments, unless indicated in the figure legend. Statistical significance is indicated as follows: *P < 0.05, **P < 0.01, ***P < 0.001, ****P < 0.0001.

Results

CD44hi cells exhibit SCL-associated transcriptional and tumorigenic features

CRPC has been stratified into distinct molecular subtypes, including an SCL subtype characterized by elevated CD44 expression [4]. To establish a representative model for studying this state, we profiled CRPC organoid models by RNA-seq and found that LAPC9 organoids displayed SCL-associated transcriptional features and high CD44 expression, whereas PCa16 and PM154 aligned with Wnt-driven and neuroendocrine subtypes [4], respectively (Figure 1A-C, Supplementary Figure 1A-C). These data support the use of LAPC9 as an SCL-associated model for subsequent mechanistic studies. We next isolated CD44-high (CD44hi) and CD44-low (CD44low) subpopulations from LAPC9 tumors by fluorescence-activated cell sorting (Supplementary Figure 1D). RNA-seq analysis revealed clear transcriptional differences between the two populations, with CD44hi cells showing enrichment of an SCL-associated transcriptional signature, whereas CD44low cells displayed relatively higher AR-related features (Figure 1D, Supplementary Figure 1E-F). Consistent with these findings, analysis of patient-derived CRPC single-cell RNA-seq datasets [27,28] showed that CD44 expression was enriched within a subset of epithelial cells located at one end of the UMAP manifold, and these CD44-enriched cells displayed SCL-associated features (Supplementary Figure 2A-E). Similar observations were made in an independent CRPC sample (Supplementary Figure 2F-J). These data support that CD44 marks an SCL-like tumor-cell state in CRPC.

To determine whether this transcriptional state was linked to functional tumorigenicity, sorted CD44hi and CD44low LAPC9-GFP/luciferase cells were cultured as organoids [24] or transplanted into mice (Figure 1E). CD44hi cells formed larger organoids than CD44low cells and generated tumors with faster growth and greater endpoint tumor burden in vivo (Figure 1F-I). Endpoint analysis further showed re-emergence of a CD44hi phenotype in tumors derived from CD44low cells during growth (Supplementary Figure 3A). Together, these findings identify the CD44hi subpopulation in LAPC9 as a more tumorigenic compartment with SCL-associated features and provide the basis for investigating mechanisms that maintain this aggressive cell state.

CD44hi cells exhibit elevated iron and reduced H3K9me2

To investigate the molecular basis of CD44hi cell tumorigenicity, we further analyzed the RNA-seq data comparing CD44hi and CD44low subpopulations from LAPC9 tumors. Pathway enrichment analysis revealed that CD44hi cells were characterized by the upregulation of gene sets associated with proliferation and metabolic reprogramming, including MYC targets, oxidative phosphorylation, E2F targets, and DNA repair (Supplementary Figure 3B). This coordinated enrichment of proliferative and biosynthetic programs suggests that CD44hi cells possess a distinct transcriptional identity and represent a more aggressive subpopulation, consistent with our *in vivo* data (Figure 1H-I). Notably, iron metabolism pathways were also enriched, and CD44hi cells displayed elevated iron-related transcriptional features (Figure 2A).

To validate these findings, we employed PC3 cells, a CRPC-SCL cell line characterized

by high CD44 expression [4]. CD44 was silenced in PC3 cells to generate PC3-shCD44 cells, enabling comparison between CD44-proficient and CD44-deficient states. Previous studies have shown that CD44 mediates iron uptake via hyaluronic acid (HA) [16]. Consistent with this, HA treatment increased intracellular iron levels in CD44-proficient cells (Supplementary Figure 3C-D). Consistent with the elevated iron signature, western blot analysis showed increased expression of the iron-storage protein Ferritin Light Chain (FTL) in LAPC9 CD44hi cells compared with CD44low cells (Figure 2B). FerrOrange-based flow cytometry further confirmed that CD44hi cells contained significantly higher intracellular labile Fe^{2+} levels (Figure 2C). We further validated these findings using the 22Rv1 cell line, which exhibits heterogeneous CD44 expression (Supplementary Figure 3E). CD44hi and CD44low cells were isolated by FACS to establish 22Rv1-CD44hi and 22Rv1-CD44low cell lines (Supplementary Figure 3F-G). Consistent with the observations in sorted LAPC9 CD44hi and CD44low subpopulations, genetic CD44 depletion reduced intracellular iron in both 22Rv1-CD44hi and PC3 cells (Figure 2D-G). Together, these findings show that elevated intracellular iron is consistently associated with the high CD44 state across multiple prostate cancer models, including SCL-associated models.

Given that CD44-mediated iron uptake has been shown to regulate H3K9me2 levels through iron-dependent histone demethylases [16], we asked whether elevated iron in CD44hi cells is associated with altered H3K9me2 in CRPC-SCL. We therefore compared H3K9me2 levels between CD44hi and CD44low cells. H3K9me2 was significantly enriched in LAPC9 CD44low cells relative to CD44hi cells (Figure 2H, Supplementary Figure 4A). In cell-line models, genetic CD44 depletion was similarly associated with increased H3K9me2 levels (Figure 2H). Collectively, these data support an iron-driven epigenetic feedback circuit that contributes to maintenance of the CD44-associated transcriptional state in the models examined (Figure 2I).

An iron-KDM3A-H3K9me2 circuit reinforces CD44 expression

To directly investigate whether H3K9me2 regulates CD44 transcription, we designed primer sets spanning the CD44 promoter (Figure 3A) and performed Chromatin immunoprecipitation followed by quantitative PCR (ChIP-qPCR). H3K9me2 was significantly enriched at the CD44 promoter relative to IgG control, confirming its specific occupancy at this locus (Figure 3B). Importantly, H3K9me2 occupancy was higher in CD44low cells than in CD44hi cells (Figure 3C), and this correlated with reduced CD44 mRNA levels (Figure 3D).

We next asked whether iron controls CD44 through H3K9me2. DFO treatment of 22Rv1-CD44hi cells reduced CD44 mRNA and protein while increasing global H3K9me2 (Figure 3E-F). ChIP-qPCR confirmed that DFO enhanced H3K9me2 occupancy at the CD44 locus (Figure 3G), supporting a model in which iron maintains CD44 expression by limiting H3K9me2 deposition. Given that iron activates Jumonji-domain histone demethylases [15], we treated cells with the pan-H3K9 demethylase inhibitor IOX1 [29]. IOX1 reduced CD44 mRNA and protein (Supplementary Figure 4B-C), indicating that H3K9 demethylase activity is required for CD44 expression.

We next sought to identify an iron-dependent demethylase contributing to H3K9me2

remodeling at the CD44 locus. Among the JMJC family members, KDM3A (also known as JMJD1A) is a well-established H3K9me2 demethylase that has been implicated in prostate cancer progression [30] and requires iron as a cofactor for catalytic activity [31]. Based on this prostate cancer-specific relevance and its iron dependence, we focused on KDM3A as the primary candidate. Although KDM3A protein levels were comparable between CD44-proficient and CD44-depleted cells (Supplementary Figure 4D), KDM3A activity is limited by iron availability rather than protein abundance. We therefore reasoned that elevated intracellular iron in CD44hi cells would enhance KDM3A activity even in the absence of protein upregulation. To test its role, we employed CBA-1, a KDM3A inhibitor [32]. CBA-1 reduced CD44 expression, increased global H3K9me2, and enhanced H3K9me2 occupancy at the CD44 locus (Supplementary Figure 4E-G), supporting the involvement of KDM3A in CD44 regulation. Consistently, KDM3A knockdown reduced CD44 protein and mRNA expression and increased H3K9me2 occupancy at the CD44 locus (Figure 3H-J), providing genetic evidence for this effect. KDM3A ChIP-qPCR further demonstrated significantly increased KDM3A occupancy at the CD44 regulatory region in CD44hi cells compared with CD44low cells (Figure 3K), providing additional evidence for locus-specific regulation by KDM3A. These data suggest that KDM3A-dependent H3K9me2 remodeling contributes to maintaining low H3K9me2 and high CD44 expression in CD44hi cells.

Since CD44 facilitates iron uptake, we reasoned that CD44 might also regulate H3K9me2 through iron availability. shCD44-mediated silencing of CD44 reduced intracellular iron (Figure 2D-G), which would be predicted to impair the activity of iron-dependent H3K9me2 demethylases including KDM3A. Consistent with this, shCD44 increased H3K9me2 occupancy at the CD44 promoter (Figure 3L), mirroring the effects of direct KDM3A inhibition with CBA-1. To further define the causal relationship between CD44, iron availability, and H3K9me2 regulation, we performed epistasis experiments. Iron supplementation reversed the increase in H3K9me2 caused by CD44 depletion, whereas KDM3A inhibition with CBA-1 blocked the iron induced reduction in H3K9me2 (Supplementary Figure 4H). We further examined the effect of iron supplementation in the context of KDM3A depletion. In shCTR cells, iron supplementation produced modest changes in H3K9me2 and CD44 expression, whereas in shKDM3A cells, iron addition resulted in little further change in either marker (Supplementary Figure 4I), supporting a functional role for KDM3A in the iron-dependent regulation of H3K9me2 and CD44. These findings place intracellular iron upstream of KDM3A-dependent H3K9me2 regulation in the CD44hi state.

These data support a model in which the CD44-iron-KDM3A-H3K9me2 axis operates as a self-reinforcing loop: CD44-mediated iron uptake supports KDM3A-dependent H3K9me2 remodeling at the CD44 locus, thereby contributing to maintenance of CD44 expression. Disruption of CD44 reduces iron supply, leading to H3K9me2 accumulation and further CD44 silencing (Figure 3M).

CD44low cells can regain CD44 during tumor growth in vivo (Supplementary Figure 3A). We therefore asked whether the iron-KDM3A-H3K9me2 axis contributes to the re-emergence of the CD44hi phenotype from a CD44low-enriched population. When

22Rv1-CD44low cells were cultured in 3D organoid conditions, CD44 expression increased progressively over 72 h, accompanied by a decrease in global H3K9me2 levels (Supplementary Figure 4J). These population-level changes are consistent with re-establishment of the chromatin state associated with CD44hi cells, although they do not distinguish true phenotypic conversion from selective expansion of rare residual CD44hi cells after sorting. Importantly, DFO, IOX1, and CBA-1 each suppressed the re-emergence of CD44 expression under these conditions (Supplementary Figure 4K-M), supporting a role for iron availability and KDM3A-dependent H3K9me2 remodeling in efficient re-establishment of the CD44hi phenotype in 3D culture. Although KDM3A was genetically validated in complementary experiments, the 3D re-emergence assay itself was assessed pharmacologically and therefore provides supportive rather than independent genetic evidence for KDM3A involvement in this setting.

Together, these data support a self-reinforcing epigenetic circuit in which CD44-associated iron accumulation promotes KDM3A-dependent H3K9me2 remodeling at the CD44 locus, thereby contributing to maintenance and re-establishment of the CD44hi-associated state.

The iron-KDM3A-H3K9me2 axis regulates a MYC-associated transcriptional program in CD44hi cells

We have shown that CD44 promotes iron accumulation to sustain KDM3A-dependent H3K9me2 demethylation, thereby reinforcing CD44 expression itself. We therefore asked whether this self-reinforcing epigenetic circuit functions more broadly to maintain the CD44-associated transcriptional state beyond regulation of a single marker gene. To address this, we performed RNA-seq in LAPC9 organoids treated with DFO or CBA-1, representing independent perturbations targeting distinct nodes of the iron-KDM3A-H3K9me2 axis.

Signature analysis revealed that both treatments significantly reduced SCL features (Figure 4A), suggesting disruption of the broader CD44hi transcriptional state. Consistent with our earlier pathway analysis showing that CD44hi cells are enriched for proliferative and metabolic programs—including MYC, E2F, DNA repair, and oxidative phosphorylation (Supplementary Figure 3B)—both DFO and CBA-1 treatment led to coordinated downregulation of these pathways (Figure 4B), indicating reversal of CD44-associated transcriptional programs. After excluding canonical proliferation-associated Hallmark gene sets, the inverse pathway-level relationship remained significant for both DFO and CBA-1, indicating that reduced proliferation does not fully account for the broader transcriptional changes (Supplementary Figure 5A-B). The highly concordant transcriptional responses observed across these independent perturbations further support the existence of a shared iron-dependent epigenetic mechanism maintaining the CD44-associated transcriptional state. To identify the core gene set targeted by this axis, we examined the overlap between genes upregulated in CD44hi cells and those downregulated upon treatment. Within this shared gene set, MYC target genes were prominently represented, with a substantial fraction exhibiting concordant inverse regulation across conditions (Figure 4C). Enrichment analysis further confirmed that MYC targets were significantly

overrepresented among genes co-downregulated by both treatments (Fisher's exact test, Figure 4D), indicating preferential targeting of a shared MYC-associated transcriptional program. Consistent with this, MYC target genes displayed a coordinated shift toward decreased expression following treatment (Figure 4E-F), supporting global suppression of MYC transcriptional program. Together, these data indicate that the iron-KDM3A-H3K9me2 axis maintains the CD44-associated transcriptional state, with MYC target genes representing a prominently regulated pathway.

Functionally, both DFO and CBA-1 significantly impaired organoid-forming capacity (Figure 4G-H), consistent with reduced growth and tumorigenic fitness. Western blot analysis confirmed that both treatments increased H3K9me2 levels while reducing CD44 and c-MYC expression (Figure 4I), consistent with epigenetic repression of the CD44hi program. Consistent results were observed in cell line models, where CD44hi cells exhibited enhanced tumorigenicity (Supplementary Figure 6A-D), and both DFO and CBA-1 markedly reduced colony formation and proliferation (Supplementary Figure 6E-P). Together, perturbation of iron availability or KDM3A activity suppresses SCL-associated and MYC-related transcriptional programs and impairs tumorigenic fitness, supporting a role for the iron-KDM3A-H3K9me2 axis in maintaining this state.

Elevated iron engages NRF2-mediated ferroptosis defense and increases NRF2 reliance in CD44hi cells

CD44hi cells maintain elevated intracellular iron, which supports their stem cell-like state but may also increase ferroptotic stress [33]. Consistently, CD44hi cells exhibited higher basal lipid peroxidation than matched shCD44 cells, while iron supplementation further increased lipid peroxidation in shCD44 cells (Figure 5A). However, CD44hi cells were not selectively sensitive to the ferroptosis inducers erastin, a System Xc^- inhibitor, or RSL3, a GPX4 inhibitor (Supplementary Figure 7A-B), suggesting compensatory mechanisms that buffer iron-associated ferroptotic stress.

RNA-seq and transcriptional regulatory analyses predicted increased NRF2 (NFE2L2) activity in CD44hi cells (Figure 5B, Supplementary Figure 7C). We therefore examined whether NRF2 responds to iron availability. Iron supplementation increased NRF2 expression and activity in 22Rv1-shCD44 cells, whereas DFO reversed this response (Figure 5C, Supplementary Figure 7D-E). Conversely, DFO reduced NRF2 activity in CD44hi cells, with similar results observed in PC3 cells (Supplementary Figure 7F-H). These findings support iron-sensitive regulation of NRF2 in the CD44hi state. Consistently, NRF2 and its ferroptosis-defense targets [34,35], including SLC7A11, GPX4, and FTL, were elevated in CD44hi cells compared with CD44-knockdown cells (Figure 5D, Supplementary Figure 7I).

To assess the functional role of NRF2, we depleted NRF2 in CD44hi cells. NRF2 knockdown reduced its downstream targets (Figure 5E), increased the labile iron pool and lipid peroxidation (Supplementary Figure 8A-B), and sensitized CD44hi cells to RSL3 (Supplementary Figure 8C), supporting a protective role for NRF2 against ferroptotic stress. NRF2 depletion did not appreciably alter CD44 protein expression (Supplementary Figure 8D), indicating that NRF2 loss does not substantially affect

CD44 levels under these conditions.

We next asked whether increased iron enhances the requirement for NRF2 protection in CD44low cells. Iron supplementation increased NRF2 expression and its downstream targets, whereas NRF2 remained suppressed following knockdown (Figure 5F). Under iron loading, NRF2 depletion further increased lipid peroxidation (Supplementary Figure 8E-F) and sensitized cells to RSL3 (Figure 5G), supporting an increased requirement for NRF2-mediated protection under iron-rich conditions.

Finally, we directly compared the consequences of NRF2 depletion in CD44hi and CD44low cells. NRF2 knockdown efficiency was comparable between CD44hi and CD44low cells, as confirmed by WB (Supplementary Figure 8G). NRF2 loss increased the labile iron pool in both populations, with a greater increase in CD44hi cells (Supplementary Figure 8H-I). Similarly, NRF2 depletion produced a greater increase in lipid peroxidation in CD44hi cells (Figure 5H, Supplementary Figure 8J) and more strongly sensitized CD44hi cells to RSL3 (Figure 5I). These findings support a greater reliance of CD44hi cells on NRF2-mediated ferroptosis defense.

Together, these data support a model in which elevated iron increases ferroptotic stress while engaging NRF2-dependent antioxidant defense. In CD44hi cells, NRF2 helps buffer iron-associated lipid peroxidation, resulting in an increased reliance on NRF2-mediated protection (Figure 5J). This genetic evidence of enhanced NRF2 reliance provided the rationale to test whether pharmacological disruption of NRF2-associated defense could exploit this iron-associated vulnerability.

Pharmacological targeting of NRF2-associated defense preferentially induces ferroptotic stress in CD44hi cells

Based on the greater reliance of CD44hi cells on NRF2-mediated protection, we next asked whether this vulnerability could be pharmacologically exploited. Treatment with Brusatol, an NRF2-targeting compound [36], showed that CD44hi cells were significantly more sensitive to Brusatol than CD44low cells (Figure 6A-B). In a competitive co-culture assay, CD44hi cells were preferentially eliminated over shCD44-GFP cells upon Brusatol treatment (Figure 6C-D, Supplementary Figure 9A-C). Ex vivo treatment of LAPC9 tumor tissues further confirmed that Brusatol selectively reduced the CD44hi subpopulation (Figure 6E, Supplementary Figure 9D).

We next investigated the molecular basis of this selective killing. Brusatol treatment reduced NRF2 protein levels and coordinately suppressed its downstream targets SLC7A11, GPX4, and FTL (Figure 6F, Supplementary Figure 9E). Because Brusatol has reported NRF2-independent effects [36], we further examined its activity after genetic NRF2 depletion. NRF2 knockdown markedly reduced Brusatol sensitivity and attenuated Brusatol-induced lipid peroxidation, indicating that NRF2 is a major functional mediator of the ferroptosis-associated response to Brusatol in CD44hi cells, although NRF2-independent effects cannot be excluded (Supplementary Figure 9F-G).

We then measured LIP levels following Brusatol treatment. Brusatol increased LIP to a greater extent in CD44hi cells than in shCD44 cells (Figure 6G, Supplementary Figure 9H-I). Elevated LIP drives lipid peroxidation and ferroptosis [30], and indeed, Brusatol markedly enhanced lipid peroxidation in CD44hi cells compared to shCD44

cells (Figure 6H, Supplementary Figure 9J-K). This increase was reversed by co-treatment with the iron chelator DFO or the lipid peroxidation inhibitor liproxstatin-1 (Figure 6I, Supplementary Figure 9J-K), confirming its dependence on iron-driven oxidative stress. To determine whether ferroptosis is the primary mode of cell death, we assessed whether ferroptosis inhibitors could rescue Brusatol-induced cytotoxicity. Brusatol reduced CD44hi cell viability more potently than shCD44 cells, and this effect was largely reversed by DFO and liproxstatin-1 (Figure 6J, Supplementary Figure 9L). To assess the contribution of other death pathways, we co-treated cells with inhibitors of apoptosis (Z-VAD-FMK), autophagy (chloroquine, CQ), or ferroptosis (DFO). Only DFO rescued Brusatol-induced cell death, whereas Z-VAD-FMK and chloroquine had minimal effects (Figure 6K).

Together, these results show that CD44hi cells are preferentially sensitive to pharmacological disruption of NRF2-associated ferroptosis defense. Brusatol increased the labile iron pool and lipid peroxidation and preferentially induced ferroptosis-associated cytotoxicity in CD44hi cells, supporting pharmacological exploitation of this adaptive defense while not excluding NRF2-independent effects of Brusatol.

Brusatol suppresses LAPC9 tumor growth and increases lipid peroxidation *in vivo*

To evaluate the in vivo effects of Brusatol in the LAPC9 model, we established subcutaneous LAPC9-copGFP-CBR xenografts in CB17 SCID mice. At one week post-implantation, mice were randomized by bioluminescence intensity and body weight and subsequently treated with vehicle or Brusatol (2 mg/kg every other day) for two weeks (Figure 7A). Bioluminescence imaging at week 3 revealed significantly reduced tumor signal in the Brusatol treated group compared to vehicle-treated controls (Figure 7B). Consistently, endpoint tumor volume and weights were lower in the Brusatol treated group (Figure 7C-D, Supplementary Figure 10A), indicating that pharmacological disruption of NRF2-associated ferroptosis defense suppresses LAPC9 tumor growth *in vivo*. Immunohistochemical analysis demonstrated that the expression levels of CD44 and NRF2 were markedly reduced following Brusatol treatment. In contrast, the lipid peroxidation marker 4-hydroxynonenal (4-HNE) was significantly increased in the treated group, indicating enhanced lipid peroxidation in vivo (Figure 7E-F). We next examined the CD44hi population following Brusatol treatment. Flow cytometry analysis demonstrated a marked reduction in the proportion of CD44hi cells in Brusatol-treated tumors compared with controls (Figure 7G). Western blot analysis showed that Brusatol treatment reduced FTL protein levels, consistent with suppression of the NRF2-associated ferroptosis-defense program (Supplementary Figure 10B). Brusatol also decreased CD44 expression, corroborating the reduction of the CD44hi population observed by FACS analysis. This finding is consistent with our *ex vivo* observations (Figure 6E, Supplementary Figure 9D), and is consistent with Brusatol treatment reducing the CD44hi subpopulation. Together, these results indicate that pharmacological disruption of NRF2-associated ferroptosis defense impairs tumor growth and reduces CD44hi cells in SCL-associated LAPC9

tumors, supporting NRF2-associated ferroptosis defense as a candidate therapeutic vulnerability in this aggressive prostate cancer subtype.

H3K9me2 remodeling links the CD44-associated transcriptional program with NRF2-mediated ferroptosis defense in CRPC-SCL

Having shown that disruption of NRF2-associated ferroptosis defense preferentially sensitizes CD44hi cells to ferroptotic stress, we next asked how NRF2 expression is maintained in this cell state. We previously found that iron promotes NRF2 expression (Figure 5C), but the underlying chromatin mechanism remained unclear. Because the iron-KDM3A-H3K9me2 axis sustains CD44 expression (Figure 3), we investigated whether the same chromatin mechanism also contributes to NRF2 regulation.

ChIP-qPCR confirmed H3K9me2 enrichment at the NRF2 regulatory region above IgG background (Supplementary Figure 10C). Pharmacological inhibition of KDM3A with CBA-1 further increased H3K9me2 occupancy at this locus and was accompanied by reduced NRF2 mRNA and protein expression (Supplementary Figure 10D-F). Consistently, genetic depletion of KDM3A increased H3K9me2 occupancy at the NRF2 locus and reduced NRF2 mRNA and protein levels (Figure 8A-C), providing independent genetic support for KDM3A-dependent regulation of NRF2. We next examined this relationship in the endogenous CD44-defined states. H3K9me2 occupancy at the NRF2 regulatory region was higher in CD44low than in CD44hi cells (Supplementary Figure 10G). Conversely, KDM3A ChIP-qPCR showed greater KDM3A occupancy at the NRF2 locus in CD44hi cells than in CD44low cells (Supplementary Figure 10H-I). Together, these findings support a model in which KDM3A-dependent H3K9me2 remodeling contributes to NRF2 transcriptional regulation in the iron enriched CD44hi state.

Together with our CD44 promoter analyses, these findings support a unified chromatin-regulatory model in which the iron-KDM3A-H3K9me2 axis contributes to the regulation of both CD44 expression and NRF2-mediated ferroptosis defense. In this model, CD44-associated iron accumulation supports KDM3A-dependent H3K9me2 remodeling at the CD44 and NRF2 loci, thereby favoring expression of both genes. This shared chromatin mechanism links maintenance of the CD44-associated stem-like state with NRF2-mediated protection from ferroptotic stress (Figure 8D). Although NRF2 is also regulated post-translationally through the KEAP1-proteasome pathway, our data support H3K9me2 remodeling as an additional transcriptional mechanism contributing to NRF2 expression in CD44hi cells.

We next examined whether this coupled CD44/NRF2 state is enriched in CRPC-SCL models. Analysis of the full *Tang et al* [4] dataset showed enrichment of iron and NRF2 related programs across independently derived SCL-classified models, supporting broader relevance of this molecular state beyond LAPC9 (Figure 8E-F). Consistently, analysis of our independent CRPC organoid panel showed a similar enrichment of iron- and NRF2-related transcriptional programs in the SCL-associated LAPC9 model compared with the Wnt-driven PCa16 and neuroendocrine PM154 models (Figure 8G-H). This transcriptional pattern was reflected at the protein level, with LAPC9 displaying higher KDM3A, CD44, NRF2, and FTL expression together with reduced H3K9me2

(Figure 8I). LAPC9 organoids also showed greater sensitivity to Brusatol than the other CRPC organoid models (Figure 8J), providing cross-model support for the association between the iron/NRF2 state and pharmacological vulnerability.

Together, these data reveal a double-edged role of iron in tumor cell-state control: iron-dependent H3K9me2 remodeling sustains an aggressive CD44-associated state, while the same iron-loaded state increases reliance on NRF2-mediated ferroptosis defense. Disrupting this adaptive defense unmasks the ferroptotic vulnerability associated with the iron-rich CD44hi state.

Patient analyses support a CD44-associated iron/NRF2 program and its prognostic relevance in prostate cancer

To extend our findings to patients, we first assessed the relationship between SCL features and iron-linked regulators in the TCGA prostate cancer cohort (n=418). To avoid circularity in analyses involving CD44 expression, CD44-independent versions of the SCL and iron signatures were used. The CD44-independent SCL score was positively correlated with CD44 expression (Figure 9A), CD44-independent iron score (Figure 9B), NFE2L2/NRF2 expression (Figure 9C), and KDM3A levels (Figure 9D), consistent with the coordinated upregulation of this axis in SCL-high tumors. These correlations were independently validated in the DKFZ cohort (n=242) for CD44, NFE2L2, and KDM3A. The correlation with iron score showed a positive but non-significant trend (Supplementary Figure 11A).

To further determine whether the CD44-associated iron/NRF2 state could be detected at single-cell resolution in patient tumors, we analyzed CRPC scRNA-seq datasets from GSE137829 and GSE210358. Major cell types were first annotated using the Seurat workflow, and epithelial cells were selected for downstream analysis (Supplementary Figure 11B-E). To avoid correlations driven by inter-patient differences or non-tumor cell composition, correlations between CD44 expression and iron or NRF2 scores were calculated independently within each patient sample.

Across seven CRPC patient samples, CD44 expression showed a reproducible positive association with NRF2 scores and was positively associated with iron scores in most samples (Figure 9E, Supplementary Figure 12A-C). Importantly, CD44 was excluded from the iron score to avoid circularity. These patient-wise single-cell analyses support the presence of a CD44-linked iron/NRF2 program within the epithelial compartment of CRPC samples, consistent with the iron-loaded and NRF2-dependent CD44hi state observed in our experimental models. These analyses do not directly assess the KDM3A-H3K9me2 chromatin mechanism.

We next asked whether this molecular signature carries prognostic value. We derived a FerroScore—a composite risk score based on the expression of CD44, FTL, FTH1, SLC11A2, KDM3A, HMOX1 and NFE2L2. FerroScore was developed as a multigene prognostic signature derived from genes associated with the iron/NRF2-related network and was intended to capture the integrated prognostic pattern of this network rather than the activity of any individual gene or pathway component. In the TCGA cohort, patients with high FerroScore exhibited significantly worse biochemical recurrence (BCR)-free survival compared to those with low FerroScore (Figure 9F).

The resulting FerroScore formula was then applied unchanged to the independent DKFZ cohort. Higher FerroScore was associated with shorter BCR-free survival in both cohorts, supporting external validation of the TCGA-derived score. (Figure 9G). We also evaluated FerroScore in the SU2C metastatic CRPC cohort (75 evaluable cases: 37 in the top/bottom-quartile comparison). The locked TCGA-derived FerroScore was not significantly associated with overall survival in SU2C. Given the distinct disease setting, clinical endpoint and limited sample size, we considered this analysis exploratory. In a separate exploratory analysis, refitting the same seven-gene panel within SU2C using overall survival as the endpoint yielded a cohort-specific score associated with survival (Supplementary Figure 12D). Because this model was developed and evaluated within the same cohort, it was not considered an independent validation of the TCGA-derived FerroScore. To determine whether FerroScore was independently associated with biochemical recurrence beyond established clinical parameters, we performed multivariable Cox regression analyses adjusting for Gleason grade, PSA level, age, and T stage. In both the TCGA and DKFZ cohorts, When evaluated as a dichotomous variable using the cohort-specific median cutoff, FerroScore remained significantly associated with worse biochemical recurrence (TCGA: HR 5.96, 95% CI 2.30-15.41, P=0.00023; DKFZ: HR 2.37, 95% CI 1.14-4.93, P=0.021) after adjustment for these clinicopathological variables (Figure 9H, Supplementary Figure 12E), supporting its independent prognostic association. Collectively, these analyses support FerroScore as a multigene prognostic score associated with adverse clinical outcome in prostate cancer. Importantly, FerroScore reflects the integrated prognostic contribution of genes associated with the iron/NRF2-related network and should not be interpreted as a direct measure of CD44 or NRF2 activity. Whether this score has treatment-predictive value, including for therapies targeting iron metabolism or NRF2-associated ferroptosis defense, remains to be established prospectively.

Together, these findings support a model in which iron-dependent H3K9me2 remodeling contributes to maintenance of the CD44-associated stem-like state while coupling this state to NRF2-mediated ferroptosis protection, thereby revealing a potential therapeutic vulnerability of iron-loaded CD44hi tumor cells (Figure 10).

Discussion

In this study, we identify an iron-dependent epigenetic circuit that sustains a CD44-associated stem-like tumor-cell state and links this state to NRF2-mediated ferroptosis defense. Our data support a model in which CD44-associated iron accumulation promotes KDM3A-dependent H3K9me2 remodeling at the CD44 locus, thereby supporting CD44 expression and the associated MYC-linked stem-like transcriptional program. At the same time, the iron-loaded CD44hi state is coupled to NRF2-mediated antioxidant protection, allowing these cells to tolerate iron-driven lipid peroxidative stress. Genetic disruption of NRF2-mediated defense preferentially sensitized CD44hi cells to ferroptotic challenge, whereas Brusatol treatment reduced LAPC9 tumor growth and increased lipid peroxidation in vivo.

Several individual components of this model have substantial precedent, including CD44-associated iron uptake, iron-dependent chromatin regulation, and NRF2-mediated ferroptosis defense. The principal conceptual advance of the present study is therefore not any one of these processes in isolation, but their mechanistic integration within the iron-loaded CD44hi state, in which iron-dependent H3K9me2 remodeling supports the CD44-associated transcriptional program while the same iron-loaded state creates increased reliance on NRF2-mediated ferroptosis protection.

Recent chromatin and transcriptional profiling studies have classified CRPC into distinct molecular subtypes, including a stem cell-like subtype characterized by elevated CD44 expression and reduced dependence on androgen receptor signaling [4]. However, the mechanisms that maintain this subtype have remained poorly defined. Our findings provide mechanistic insight into this question by showing that CD44hi cells are not simply a marker-defined population, but a functionally distinct tumorigenic compartment maintained by an iron-dependent chromatin regulatory circuit. The re-emergence of the CD44hi phenotype from CD44low-enriched populations during tumor growth suggests substantial phenotypic plasticity, although these experiments cannot distinguish true state conversion from selective expansion of rare residual CD44hi cells. Future lineage-tracing and single-cell multi-omic studies will be required to determine whether CD44hi cells represent a stable lineage, a reversible cell state, or both.

Our work also extends previous studies linking CD44-mediated hyaluronic acid uptake to iron-dependent epigenetic plasticity. Müller and colleagues showed that CD44-mediated iron endocytosis regulates H3K9me2 through PHF8 in breast cancer cells [16]. In contrast, our data identify KDM3A as an important mediator of iron-dependent H3K9me2 remodeling in CRPC-SCL. This difference suggests that CD44-associated iron uptake may engage distinct Jumonji-domain histone demethylases depending on tumor context. In prostate cancer, KDM3A has been implicated in androgen receptor signaling, DNA repair, and disease progression, making it a plausible chromatin effector of iron-dependent cell-state control [30]. Although KDM3A abundance was not markedly different between CD44hi and CD44low cells, its catalytic activity is iron-dependent, supporting an activity-based mechanism in which increased intracellular iron enhances KDM3A function without requiring increased KDM3A expression. Our KDM3A ChIP-qPCR further showed preferential KDM3A occupancy at the CD44 locus

in CD44hi cells, supporting KDM3A as an important mediator of this iron sensitive chromatin regulation in CRPC-SCL. A central finding of this study is that the iron-KDM3A-H3K9me2 axis links CD44-associated identity with NRF2-mediated ferroptosis defense. Elevated iron can support tumor growth and chromatin remodeling, but it also increases the risk of lipid peroxidation and ferroptotic stress. CD44hi cells appear to resolve this tension by activating NRF2-associated antioxidant and iron-homeostasis programs, including SLC7A11, GPX4, and FTL. Our ChIP-qPCR data suggest that H3K9me2 remodeling contributes to NRF2 transcriptional activation, providing a chromatin-level mechanism by which the iron-loaded state is coupled to ferroptosis defense. This finding is consistent with a recent report that H3K9 methylation regulates NRF2 expression [37]. Because NRF2 is also regulated post-translationally through the KEAP1-proteasome pathway, our findings do not exclude canonical NRF2 regulation, but instead identify H3K9me2 remodeling as an additional transcriptional mechanism supporting NRF2 expression in CD44hi cells.

Therapeutically, our data suggest that CD44hi cells are not simply more sensitive to ferroptosis because they contain more iron. Indeed, conventional ferroptosis inducers targeting individual downstream nodes, such as erastin or RSL3, did not selectively eliminate CD44hi cells. Instead, CD44hi cells appear to depend on an upstream NRF2-associated defense program that coordinates multiple ferroptosis-protective mechanisms [34,38]. Pharmacological disruption of this defense with Brusatol increased labile iron, enhanced lipid peroxidation, and selectively reduced CD44hi cell viability. These findings support the concept that iron-loaded CD44hi cells harbor a conditional vulnerability: they tolerate elevated iron under basal conditions, but become susceptible to ferroptosis when adaptive antioxidant defense is impaired.

Our patient analyses further support the clinical relevance of the CD44-iron-NRF2 state. Bulk prostate cancer cohorts showed associations between SCL features and CD44, iron-related genes, KDM3A, and NRF2. Single-cell RNA-seq analyses further indicated that the CD44-associated iron/NRF2 program can be detected within the epithelial cell compartment, reducing the likelihood that these associations are driven only by differences in stromal or immune composition. Finally, FerroScore was associated with adverse outcome in independent prostate cancer cohorts, supporting the prognostic relevance of this multigene expression pattern. These findings support the potential value of FerroScore for risk stratification, although prospective studies will be needed to determine whether FerroScore can serve as a predictive biomarker for therapies targeting iron-loaded or NRF2-dependent tumor states.

We acknowledge several limitations. First, although key molecular features were reproduced in an independently classified SCL model and supported across the Tang et al dataset, mechanistic studies were primarily performed in the experimentally tractable 22Rv1-derived CD44hi/CD44low system, whereas functional and in vivo validation of the SCL-associated phenotype was centered on LAPC9. Therefore, universal functional dependency across CRPC-SCL cannot be inferred from the present study. Second, because these experiments were performed using sorted populations rather than lineage-traced single cells, they cannot distinguish true CD44low-to-CD44hi state conversion from selective expansion of rare residual CD44hi

cells. The lineage-tracing approaches will be required to resolve these possibilities. Third, Brusatol may have NRF2-independent effects; therefore, we interpret these experiments as pharmacological disruption of NRF2-associated ferroptosis defense rather than proof of NRF2-specific inhibition, supported by complementary shNRF2 experiments. Fourth, our chromatin analyses focused on selected CD44 and NRF2 promoter regions by ChIP-qPCR, and genome-wide H3K9me2/KDM3A profiling will be needed to define the broader regulatory landscape. An additional limitation is the lack of direct validation of the KDM3A-H3K9me2 chromatin mechanism in human CRPC tissue. Although CRPC single-cell transcriptomic analyses support a coordinated CD44-iron-NRF2 state, direct assessment of KDM3A occupancy and H3K9me2 remodeling in appropriately annotated human CRPC specimens will be required to establish the clinical relevance of this epigenetic mechanism. Finally, FerroScore analyses were retrospective and primarily associative. FerroScore was developed as a multigene prognostic signature derived from genes associated with the iron/NRF2-related network and should not be interpreted as a direct measure of CD44 or NRF2 pathway activity, the positive and negative coefficients reflect the conditional contribution of individual genes within the multivariable model. Moreover, the significant prognostic associations were derived primarily from TCGA and DKFZ, which predominantly represent localized or primary prostate cancer, whereas the biological mechanism investigated here is centered on CRPC. Prospective validation in advanced CRPC cohorts and therapeutic response studies will therefore be required to establish its prognostic and potential predictive utility in this disease setting.

In summary, our study supports an iron-KDM3A-H3K9me2 circuit that contributes to maintenance of the CD44-associated stem-like state and links this state to NRF2-mediated ferroptosis defense. By integrating tumor-cell identity, iron-dependent chromatin remodeling, and ferroptosis protection, these findings identify a ferroptosis-associated vulnerability of iron-loaded CD44hi tumor cells and provide a framework for further evaluating therapeutic strategies directed against this aggressive cell state.

Reference

1. Rawla P. Epidemiology of Prostate Cancer. World J Oncol. 2019 Apr;10(2):63-89. Epub 2019 Apr 20. PMID: 31068988; PMCID: PMC6497009.
2. Perlmutter, M. A. & Lepor, H. Androgen deprivation therapy in the treatment of advanced prostate cancer. Rev Urol 9 Suppl 1, S3-8 (2007).
3. Scher, H. I. et al. Trial Design and Objectives for Castration-Resistant Prostate Cancer: Updated Recommendations From the Prostate Cancer Clinical Trials Working Group 3. J Clin Oncol 34, 1402-1418 (2016).
4. Tang F, Xu D, Wang S, Wong CK. Chromatin profiles classify castration-resistant prostate cancers suggesting therapeutic targets. Science. 2022 May.
5. Naor D, Nedvetzki S, Golan I, Melnik L, Faitelson Y. CD44 in cancer. Crit Rev Clin Lab Sci. 2002;39(6):527–79.
6. Chen C, Zhao S, Karnad A, Freeman JW. The biology and role of CD44 in cancer progression: therapeutic implications. J Hematol Oncol. 2018 May 10;11(1):64.
7. Patrawala L, Calhoun T, Schneider-Broussard R, Li H, Bhatia B, Tang S, Reilly JG, Chandra D, Zhou J, Claypool K, Coghlan L, Tang DG. Highly purified CD44+ prostate cancer cells from xenograft human tumors are enriched in tumorigenic and metastatic progenitor cells. Oncogene. 2006 Mar 16;25(12):1696-708.
8. Zhang L, Sha J, Yang G, Huang X, Bo J, Huang Y. Activation of Notch pathway is linked with epithelial-mesenchymal transition in prostate cancer cells. Cell Cycle. 2017 May 19;16(10):999-1007.
9. Patrawala L, Calhoun-Davis T, Schneider-Broussard R, Tang DG. Hierarchical organization of prostate cancer cells in xenograft tumors: the CD44+alpha2beta1+ cell population is enriched in tumor-initiating cells. Cancer Res. 2007 Jul 15;67(14):6796-805.
10. Bisson I, Prowse DM. WNT signaling regulates self-renewal and differentiation of prostate cancer cells with stem cell characteristics. Cell Res. 2009 Jun;19(6):683-97.
11. Liu C, Kelnar K, Liu B, Chen X, Calhoun-Davis T, Li H, Patrawala L, Yan H, Jeter C, Honorio S, Wiggins JF, Bader AG, Fagin R, Brown D, Tang DG. The microRNA miR-34a inhibits prostate cancer stem cells and metastasis by directly repressing CD44. Nat Med. 2011 Feb;17(2):211-5.
12. Saini S, Majid S, Shahryari V, Arora S, Yamamura S, Chang I, Zaman MS, Deng G, Tanaka Y, Dahiya R. miRNA-708 control of CD44(+) prostate cancer-initiating cells. Cancer Res. 2012 Jul 15;72(14):3618-30. doi: 10.1158/0008-5472.CAN-12-0540. Epub 2012 May 2. Erratum in: Cancer Res. 2018 Jun 15;78(12):3404.
13. Zeng Y, Wodzenski D, Gao D, Shiraishi T, Terada N, Li Y, Vander Griend DJ, Luo J, Kong C, Getzenberg RH, Kulkarni P. Stress-response protein RBM3 attenuates the stem-like properties of prostate cancer cells by interfering with CD44 variant splicing. Cancer Res. 2013 Jul 1;73(13):4123-33.
14. Wang X, Cai J, Zhao L, Zhang D, Xu G, Hu J, Zhang T, Jin M. NUMB suppression by miR-9-5P enhances CD44+ prostate cancer stem cell growth and metastasis. Sci Rep. 2021 May 27;11(1):11210.

15. Wang H, Cui C, Li W, Wu H, Sha J, Pan J, Xue W. AGD1/USP10/METTL13 complexes enhance cancer stem cells proliferation and diminish the therapeutic effect of docetaxel via CD44 m6A modification in castration resistant prostate cancer. J Exp Clin Cancer Res. 2025 Jan 14;44(1):12.
16. Müller, S., Sindikubwabo, F., Cañeque, T. et al. CD44 regulates epigenetic plasticity by mediating iron endocytosis. Nat. Chem. 12, 929–938 (2020).
17. Abbate, V. & Hider, R. Iron in biology. Metallomics Integr. Biometal Sci. 9, 1467–1469 (2017).
18. Farida B, Ibrahim KG, Abubakar B, Malami I, Bello MB, Abubakar MB, Abbas AY, Imam MU. Iron deficiency and its epigenetic effects on iron homeostasis. J Trace Elem Med Biol. 2023 Jul;78:127203. doi: 10.1016/j.jtemb.2023.127203.
19. Ghoochani A, Hsu EC, Aslan M, Rice MA, Nguyen HM, Brooks JD, et al. Ferroptosis inducers are a novel therapeutic approach for advanced prostate cancer. Cancer Res. 2021;81:1583–94.
20. Wang, Y., Ma, Y. & Jiang, K. The role of ferroptosis in prostate cancer: a novel therapeutic strategy. Prostate Cancer Prostatic Dis 26, 25–29 (2023).
21. Pettaway CA, Pathak S, Greene G, Ramirez E, Wilson MR, Killion JJ et al. Selection of highly metastatic variants of different human prostatic carcinomas using orthotopic implantation in nude mice. Clin Cancer Res 1996; 2: 1627–1636.
22. Woods-Burnham L, Basu A, Cajigas-Du Ross CK, Love A, Yates C, De Leon M, Roy S, Casiano CA. The 22Rv1 prostate cancer cell line carries mixed genetic ancestry: Implications for prostate cancer health disparities research using pre-clinical models. Prostate. 2017 Dec;77(16):1601-1608.
23. Zoni, E., Chen, L., Karkampouna, S. et al. CRIPTO and its signaling partner GRP78 drive the metastatic phenotype in human osteotropic prostate cancer. Oncogene 36, 4739–4749 (2017).
24. Karkampouna, S., La Manna, F., Benjak, A. et al. Patient-derived xenografts and organoids model therapy response in prostate cancer. Nat Commun 12, 1117 (2021).
25. Thienger P, Paassen I, Yao X, Rubin PD, Lehner M, Lillis N, Benjak A, Shah SR, Leung AK, de Brot S, Naveed A, Daniel B, Shi M, Tremblay J, Triscott J, Cassanmagnago GA, Bolis M, Mela L, Beltran H, Chen Y, Piscuoglio S, Yu H, Ng CKY, Quigley DA, Yauch RL, Rubin MA. A Double-Negative Prostate Cancer Subtype Is Vulnerable to SWI/SNF-Targeting Degrader Molecules. Cancer Res. 2026 Apr 2;86(7):1570-1585.
26. Macedo-Silva, C., Miranda-Gonçalves, V., Lameirinhas, A. et al. JmjC-KDMs KDM3A and KDM6B modulate radioresistance under hypoxic conditions in esophageal squamous cell carcinoma. Cell Death Dis 11, 1068 (2020).
27. Joseph M. Chan et al. , Lineage plasticity in prostate cancer depends on JAK/STAT inflammatory signaling. Science377,1180-1191(2022).
28. Dong, B., Miao, J., Wang, Y. et al. Single-cell analysis supports a luminal-neuroendocrine transdifferentiation in human prostate cancer. Commun Biol 3, 778 (2020).

29. Li, Q., Qin, K., Tian, Y. et al. Inhibition of demethylase by IOX1 modulates chromatin accessibility to enhance NSCLC radiation sensitivity through attenuated PIF1. Cell Death Dis 14, 817 (2023)
30. Wilson S, Fan L, Sahgal N, Qi J, Filipp FV. The histone demethylase KDM3A regulates the transcriptional program of the androgen receptor in prostate cancer cells. Oncotarget. 2017 May 2;8(18):30328-30343.
31. Fan, L., Xu, S., Zhang, F. et al. Histone demethylase JMJD1A promotes expression of DNA repair factors and radio-resistance of prostate cancer cells. Cell Death Dis 11, 214 (2020).
32. Wen Zhang, Vitaliy M. Sviripa, Epigenetic Regulation of Wnt Signaling by Carboxamide-Substituted Benzhydryl Amines that Function as Histone Demethylase Inhibitors, iScience, Volume 23, Issue 12, 2020, 101795, ISSN 2589-0042.
33. Zhang, S., Xin, W., Anderson, G.J. et al. Double-edge sword roles of iron in driving energy production versus instigating ferroptosis. Cell Death Dis 13, 40 (2022).
34. Zhang, D.D. Thirty years of NRF2: advances and therapeutic challenges. Nat Rev Drug Discov 24, 421–444 (2025).
35. Annadurai Anandhan et al., NRF2 controls iron homeostasis and ferroptosis through HERC2 and VAMP8.Sci. Adv.9,eade9585(2023).
36. Cai, S.J., Liu, Y., Han, S. et al. Brusatol, an NRF2 inhibitor for future cancer therapeutic. Cell Biosci 9, 45 (2019).
37. Richard D Horniblow, Prachi Pathak, Dario L Balacco, Animesh Acharjee, Eva Lles, Georgios Gkoutos, Andrew D Beggs, Chris Tselepis. Iron-mediated epigenetic activation of NRF2 targets. The Journal of Nutritional Biochemistry, Volume 101, 2022, 108929, ISSN 0955-2863. 2021.108929.
38. Jiang, X., Yu, M., Wang, Wk. et al. The regulation and function of Nrf2 signaling in ferroptosis-activated cancer therapy. Acta Pharmacol Sin 45, 2229–2240 (2024).

Declarations

Ethics approval and consent to participate

Ethics approval and consent to participate: All animal experiments were approved by the ethical committee of Canton Bern (animal license BE 67/20 and BE103/23). All authors have approved the manuscript and consent to its publication.

Consent for publication

Not applicable.

Data availability

The newly generated BRB-seq datasets will be deposited in the Gene Expression Omnibus (GEO) and made publicly available prior to publication. Analysis code, gene-signature definitions, and the exact FerroScore formula will also be deposited in a public repository prior to publication. Additional data supporting the findings of this study are available from the corresponding author upon reasonable request.

Competing interests

The authors declare no competing interests.

Funding

DPL is a William Dawson Scholar of McGill University, a Lewis Katz, Young Investigator of the Prostate Cancer Foundation and a Research Scholar, Junior 2 from The Fonds de Recherche du Québec, Santé. This study was supported by the Canadian Institutes of Health Research project grant, PJT-203949 to DPL. This work was supported by the Swiss National Science Foundation (189149 and 202297) to MKdJ Fondation Chercher et Trouver via Swiss Cancer Research (KFS-5405-08-2021), the Swiss Cancer Research (KFS-6228-08-2024), and the Swiss National Science Foundation (2127661/1) to TMM.

Acknowledgements

We thank Dr. Catarina Macedo Silva and Dr. Filipa Moreira Silva for their technical assistance and support with the ChIP experiments.

Author contributions

[W.C.] conceived and designed the study. [W.C., A.B. and F.B.] developed the methodology and performed the experiments. [W.C and P.C.] performed the bioinformatic and statistical analyses. [G.T. and B.R.] provided clinical information, experimental models, or essential research materials. [W.C., M.M., and S.K.] analyzed and interpreted the data. [W.C.] prepared the figures and drafted the manuscript. [T.M., D.L., S.K. and M.K.] critically reviewed and revised the manuscript. [M.K.] supervised the study and acquired funding. All authors read and approved the final manuscript.

Figure 1

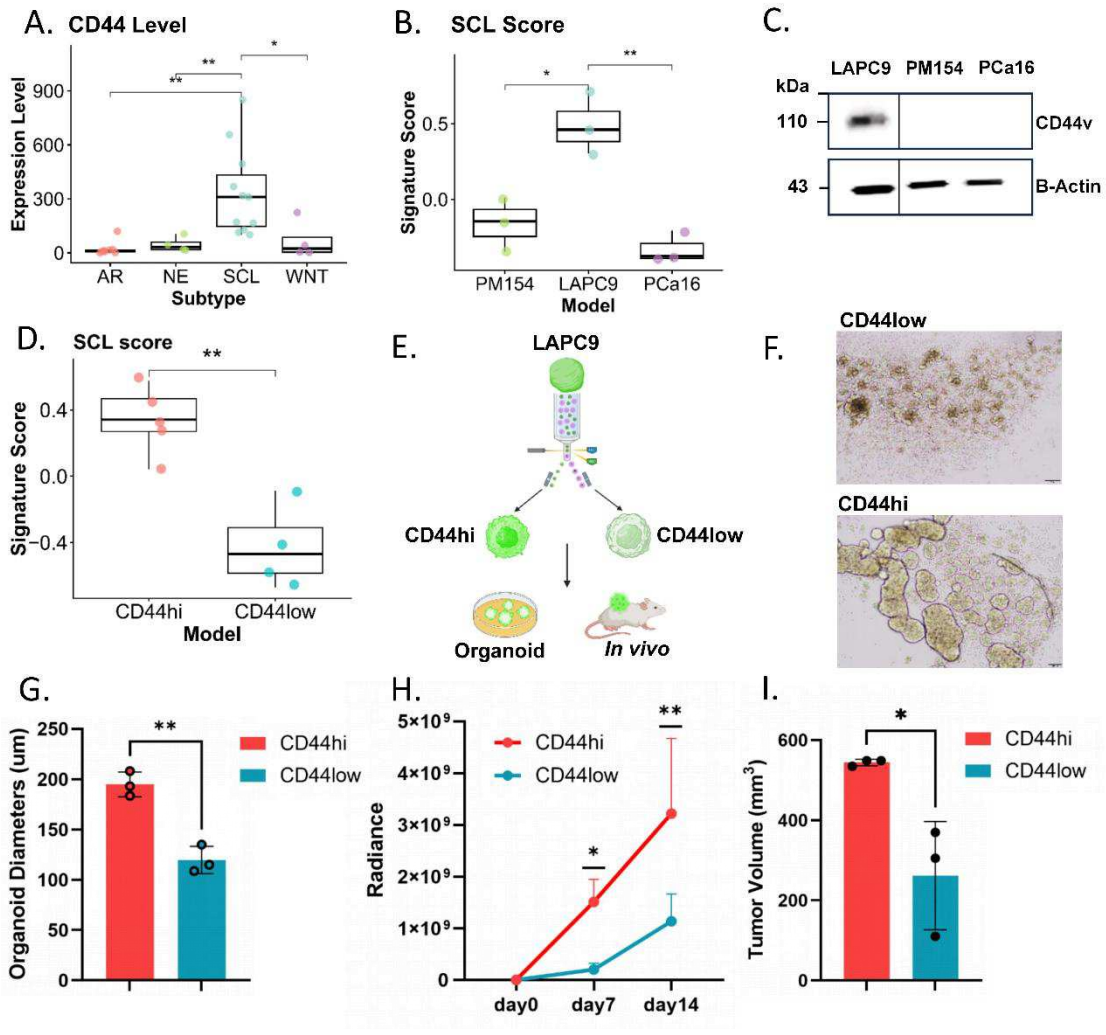


Figure 1. CD44hi cells define a tumorigenic SCL-associated compartment in CRPC.
(**A**). CD44 expression across CRPC subtype models, including androgen receptor (AR)-driven, Wnt-driven, neuroendocrine (NE), and stem cell-like (SCL) subtypes.
(**B**). SCL signature scores calculated from RNA-seq data of LAPC9, PCa16, and PM154 organoids.
(**C**). Western blot analysis of CD44 expression in LAPC9, PM154, and PCa16 organoids. Non-adjacent lanes from the same blot are separated by a vertical line.
(**D**). SCL signature scores in sorted LAPC9 CD44hi and CD44low subpopulations based on RNA-seq analysis.
(**E**). Schematic showing fluorescence-activated cell sorting of CD44hi and CD44low subpopulations from LAPC9-GFP/luciferase cells, followed by 3D organoid culture and in vivo transplantation.
(**F-G**). Representative organoid images (**F**) and quantification of organoid size (**G**) from sorted CD44hi and CD44low LAPC9 cells cultured in 3D. Each dot represents one biological replicate (n=3 independent experiments), n=3 organoids per replicate. Scale bar, 100 μm.
(**H**). Longitudinal IVIS-CT imaging and quantification of luciferase radiance showing tumor growth dynamics in CD44hi and CD44low groups. Statistical significance was assessed using a repeated-measures mixed-effects model. N=3 mice per group.
(**I**). Endpoint tumor volume at day 46, calculated as height × length × width × 0.8. n=3 mice per group. Data are shown as mean ± SD. Statistical significance was determined by unpaired two-tailed t test unless otherwise indicated. *P < 0.05, **P < 0.01, ***P < 0.001, ****P < 0.0001.

Figure 2

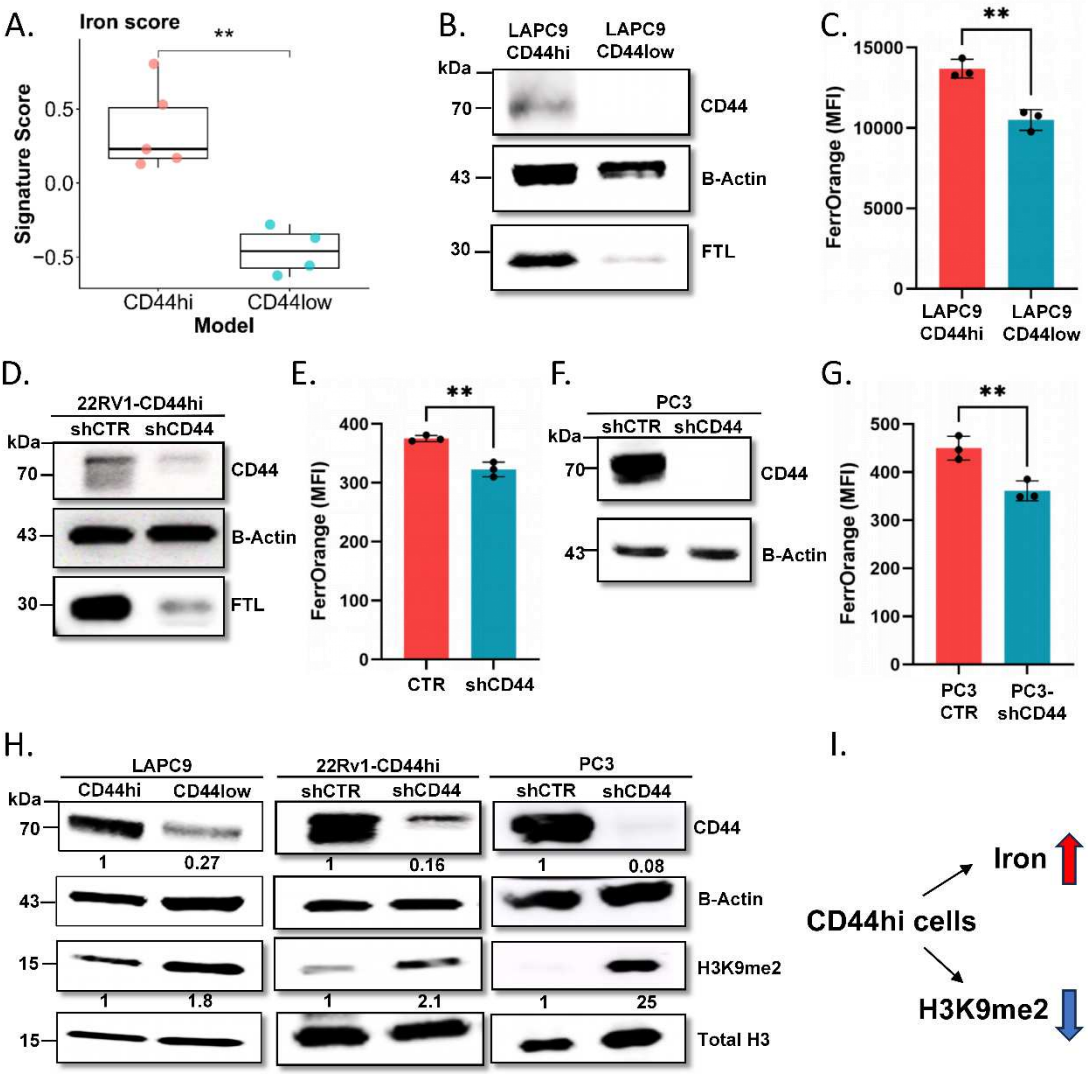


Figure 2. CD44hi cells exhibit elevated intracellular iron and reduced H3K9me2.

(**A**). Iron signature scores calculated from RNA-seq data of sorted LAPC9 CD44hi and CD44low cells, showing enrichment of iron-related programs in the CD44hi subpopulation.

(**B**). Western blot analysis of CD44 and the iron-storage protein FTL in sorted LAPC9 CD44hi and CD44low cells. β-Actin was used as a loading control.

(**C**). FerrOrange-based flow cytometry analysis showing intracellular labile Fe^{2+} levels in sorted LAPC9 CD44hi and CD44low tumor cells. n=3.

(**D**). Western blot analysis of CD44 and FTL in 22Rv1-CD44hi with non-targeting control shRNA (shCTR) and 22Rv1-shCD44 cells. β-Actin was used as a loading control.

(**E**). Flow cytometry analysis of FerrOrange staining in 22Rv1-CD44hi-shCTR and 22Rv1-shCD44 cells. n=3.

(**F**). Western blot analysis of CD44 in PC3-shCTR and PC3-shCD44 cells. β-Actin was used as a loading control.

(**G**). Flow cytometry analysis of FerrOrange staining in PC3-shCTR and PC3-shCD44 cells. n=3.

(**H**). Western blot analysis of CD44 and H3K9me2 across LAPC9 CD44hi/CD44low cells, 22Rv1-CD44hi-shCTR/22Rv1-shCD44 cells, and PC3-shCTR/PC3-shCD44 cells, showing that CD44-high or CD44-expressing cells display reduced H3K9me2. Total H3 was used as the loading control for H3K9me2.

(**I**). Schematic summary showing that the CD44hi state is characterized by elevated intracellular iron and reduced H3K9me2 modification. Data are shown as mean ± SD. Statistical significance was determined by unpaired two-tailed t test unless otherwise indicated. *P < 0.05, **P < 0.01, ***P < 0.001, ****P < 0.0001.

Figure 3

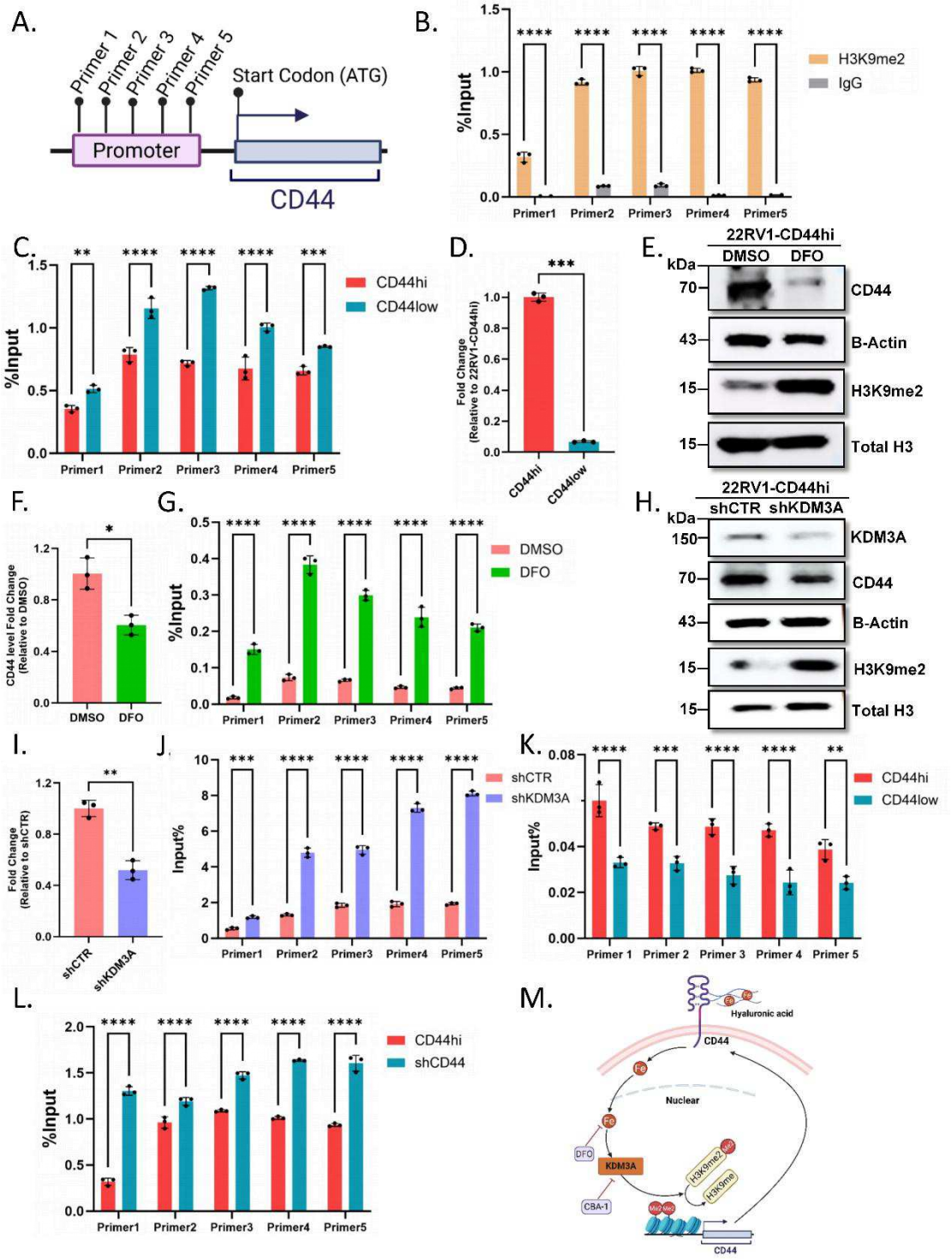


Figure 3. An iron–KDM3A–H3K9me2 circuit sustains CD44 expression.

(**A**). Schematic showing the CD44 promoter region analyzed by ChIP-qPCR. Primers were designed to amplify the upstream regulatory region of the CD44 transcription start site.

(**B**). ChIP-qPCR analysis of H3K9me2 occupancy at the CD44 promoter in 22Rv1-CD44hi cells. Signals were normalized to input, and IgG was used as a negative control.

(**C**). ChIP-qPCR analysis comparing H3K9me2 enrichment at the CD44 promoter between 22Rv1-CD44hi and 22Rv1-CD44low cells.

(**D**). qRT-PCR analysis of CD44 mRNA expression in 22Rv1-CD44hi and 22Rv1-CD44low cells.

(**E–F**). Western blot analysis of CD44 and H3K9me2 protein levels (**E**) and qRT-PCR analysis of CD44 mRNA expression (**F**) in 22Rv1-CD44hi cells treated with DFO (10 μM) for 72 h.

(**G**). ChIP-qPCR analysis of H3K9me2 enrichment at the CD44 promoter in 22Rv1-CD44hi cells treated with DFO (20 μM) for 72 h, the higher concentration was used for ChIP to achieve sufficient chromatin yield under sustained iron depletion.
(**H–I**). Western blot analysis of CD44 and H3K9me2 protein levels (**H**) and qRT-PCR analysis of CD44 mRNA expression (**I**) between 22Rv1-CD44hi shCTR and shKDM3A cells.
(**J**). ChIP-qPCR analysis of H3K9me2 enrichment at the CD44 promoter between 22Rv1-CD44hi shCTR and shKDM3A cells.
(**K**). ChIP-qPCR analysis comparing KDM3A enrichment at the CD44 promoter between 22Rv1-CD44hi and 22Rv1-CD44low cells.
(**L**). ChIP-qPCR analysis of H3K9me2 enrichment at the CD44 promoter following CD44 depletion.
(**M**). Schematic summary of the iron-KDM3A-H3K9me2 circuit regulating CD44 expression. CD44-associated iron accumulation supports KDM3A-dependent H3K9me2 remodeling at the CD44 locus, thereby contributing to maintenance of CD44 transcription. Iron chelation by DFO and KDM3A inhibition by CBA-1 disrupt this circuit, leading to H3K9me2 accumulation and reduced CD44 expression. Data are shown as mean ± SD. Statistical significance was determined by unpaired two-tailed t test unless otherwise indicated. *P < 0.05, **P < 0.01, ***P < 0.001, ****P < 0.0001.

Figure 4

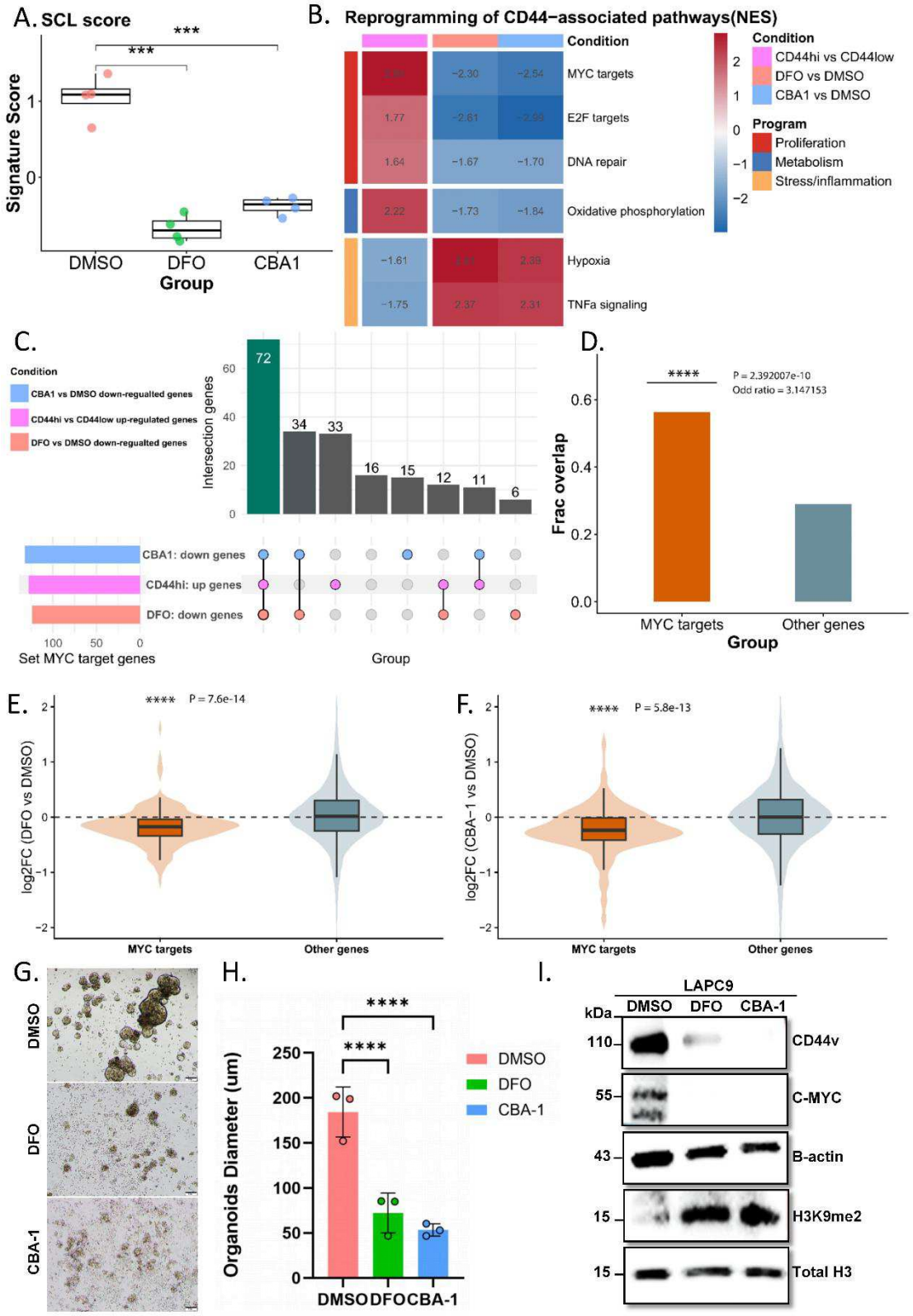


Figure 4. The iron-KDM3A-H3K9me2 axis sustains a MYC-associated CD44hi transcriptional program.

(**A**). RNA-seq analysis of LAPC9 organoids treated with DMSO, DFO (60 μM), or CBA-1 (15 μM) for 4 days. SCL signature scores show that iron chelation and KDM3A inhibition reduce the stem-like transcriptional program.

(**B**). Pathway enrichment analysis comparing LAPC9 CD44hi versus CD44low cells, DFO

versus DMSO, and CBA-1 versus DMSO. Heatmap shows normalized enrichment scores (NES) for representative pathways, highlighting reversal of CD44hi-enriched programs by DFO and CBA-1.
(**C**). UpSet plot showing the overlap between MYC target genes upregulated in CD44hi versus CD44low cells and MYC target genes downregulated after DFO or CBA-1 treatment.
(**D**). Fisher's exact test assessing enrichment of MYC target genes among CD44hi-upregulated genes that were co-downregulated by DFO and CBA-1.
(**E–F**). Distribution of log2 fold changes for MYC target genes and non-MYC genes in DFO versus DMSO (**E**) and CBA-1 versus DMSO (**F**), showing preferential downregulation of MYC-associated genes following iron chelation or KDM3A inhibition.
(**G–H**). Representative images (**G**) and quantification of organoid size (**H**) from LAPC9 organoids treated with DMSO, DFO (60 μM), or CBA-1 (15 μM) for 4 days. Organoid size was quantified using ImageJ. Each dot represents one biological replicate (n=3 independent experiments), n=6 organoids per replicate.
(**I**). Western blot analysis of CD44, c-MYC, and H3K9me2 levels in LAPC9 organoids under the indicated treatments. Data are shown as mean ± SD. Statistical significance was determined by unpaired two-tailed t test or one-way ANOVA, as appropriate. *P < 0.05, **P < 0.01, ***P < 0.001, ****P < 0.0001.

Figure 5

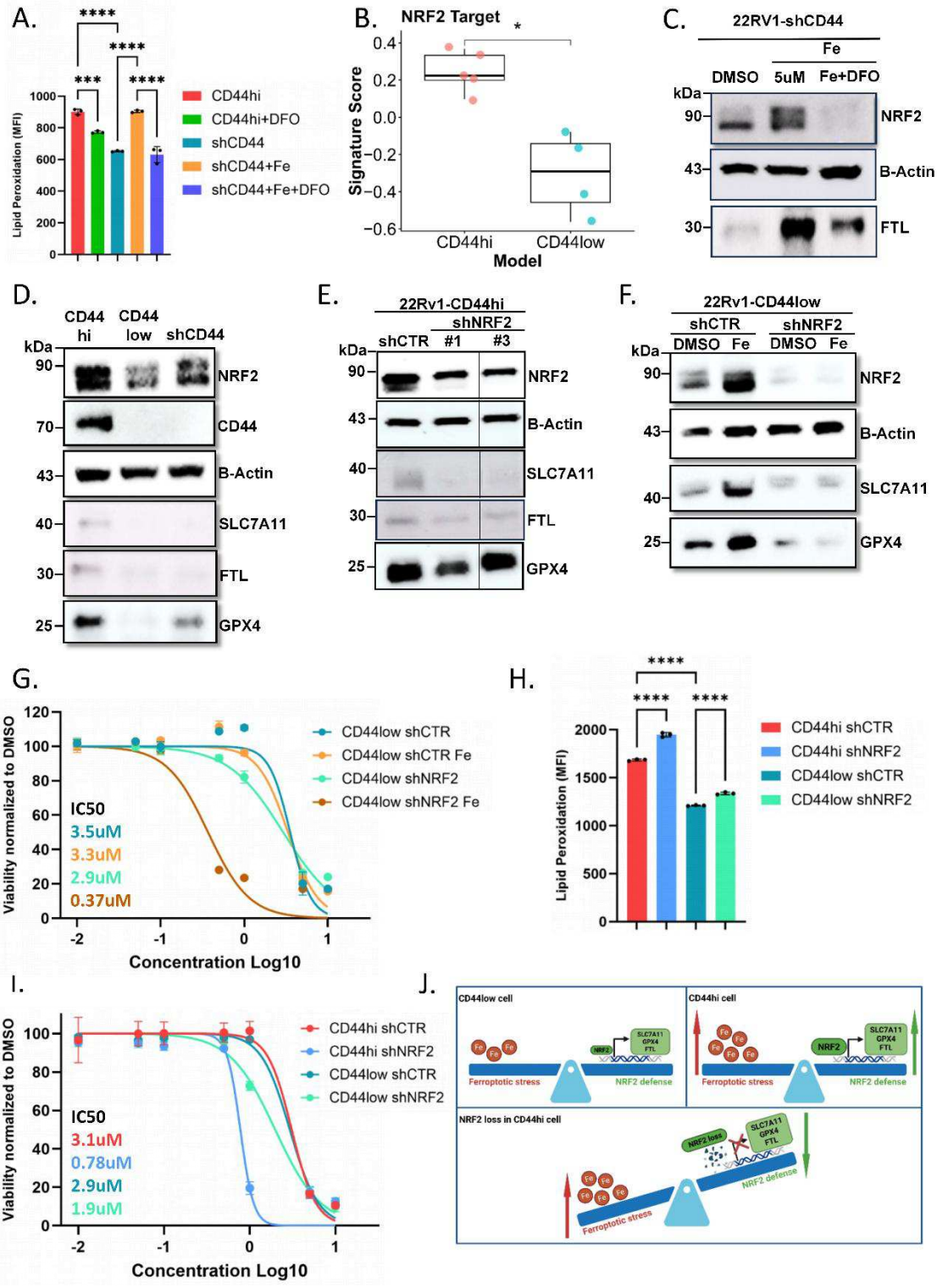


Figure 5. NRF2 enables CD44hi cells to tolerate iron-associated lipid peroxidative stress.
(**A**). Flow cytometry analysis of lipid peroxidation using C11-BODIPY staining in 22Rv1-CD44hi-shCTR and 22Rv1-CD44hi-shCD44 cells treated with iron (5 μM) or DFO (5 μM), showing that the CD44hi state is associated with increased lipid peroxidative stress.
(**B**). NRF2 target signature scores calculated from RNA-seq data of sorted LAPC9 CD44hi and CD44low cells.
(**C**). Western blot analysis of NRF2 and FTL protein levels in 22Rv1-shCD44 cells treated with iron (5 μM) or DFO (5 μM) for 72 h. Protein signals were quantified using ImageJ.

(**D**). Western blot analysis of CD44, NRF2, SLC7A11, FTL, and GPX4 in 22Rv1-CD44hi-shCTR, 22Rv1-CD44low and 22Rv1-CD44hi-shCD44 cells, showing enrichment of NRF2-associated ferroptosis-defense proteins in CD44hi cells. β-Actin was used as a loading control.
(**E**). Western blot analysis of CD44, NRF2, SLC7A11, FTL, and GPX4 in 22Rv1-CD44hi-shCTR, 22Rv1-CD44hi-shNRF2-1, and 22Rv1-CD44hi-shNRF2-3 cells, validating suppression of the NRF2-mediated ferroptosis-defense program. β-Actin was used as a loading control. Non-adjacent lanes from the same blot are separated by vertical lines.
(**F**). Western blot analysis of NRF2, SLC7A11 and GPX4 in 22Rv1-CD44low-shCTR and 22Rv1-CD44low-shNRF2 cells, treated with or without iron (5 μM) for 48h. β-Actin was used as a loading control.
(**G**). Cell viability measured by PrestoBlue assay in 22Rv1-CD44low-shCTR and shNRF2 cells, treated with or without iron (5 μM) following RSL3 treatment for 48h. n = 3.
(**H**). Flow cytometry analysis of lipid peroxidation using C11-BODIPY staining in 22Rv1-CD44hi-shCTR, 22Rv1-CD44hi-shNRF2, 22Rv1-CD44low-shCTR and 22Rv1-CD44low-shNRF2 cells. n = 3.
(**I**). Cell viability measured by PrestoBlue assay in 22Rv1-CD44hi-shCTR, 22Rv1-CD44hi-shNRF2, 22Rv1-CD44low-shCTR and 22Rv1-CD44low-shNRF2 cells following RSL3 treatment for 48h. n = 3.
(**J**). Schematic model illustrating the increased reliance of CD44hi cells on NRF2-mediated ferroptosis defense. Elevated intracellular iron increases ferroptotic stress while engaging NRF2-dependent antioxidant protection, allowing CD44hi cells to buffer lipid peroxidative stress. NRF2 depletion disrupts this protective balance, leading to increased labile iron and lipid peroxidation and enhanced sensitivity to ferroptosis induction. Data are shown as mean ± SD. Statistical significance was determined by unpaired two-tailed t test or one-way ANOVA, as appropriate. *P < 0.05, **P < 0.01, ***P < 0.001, ****P < 0.0001.

Figure 6

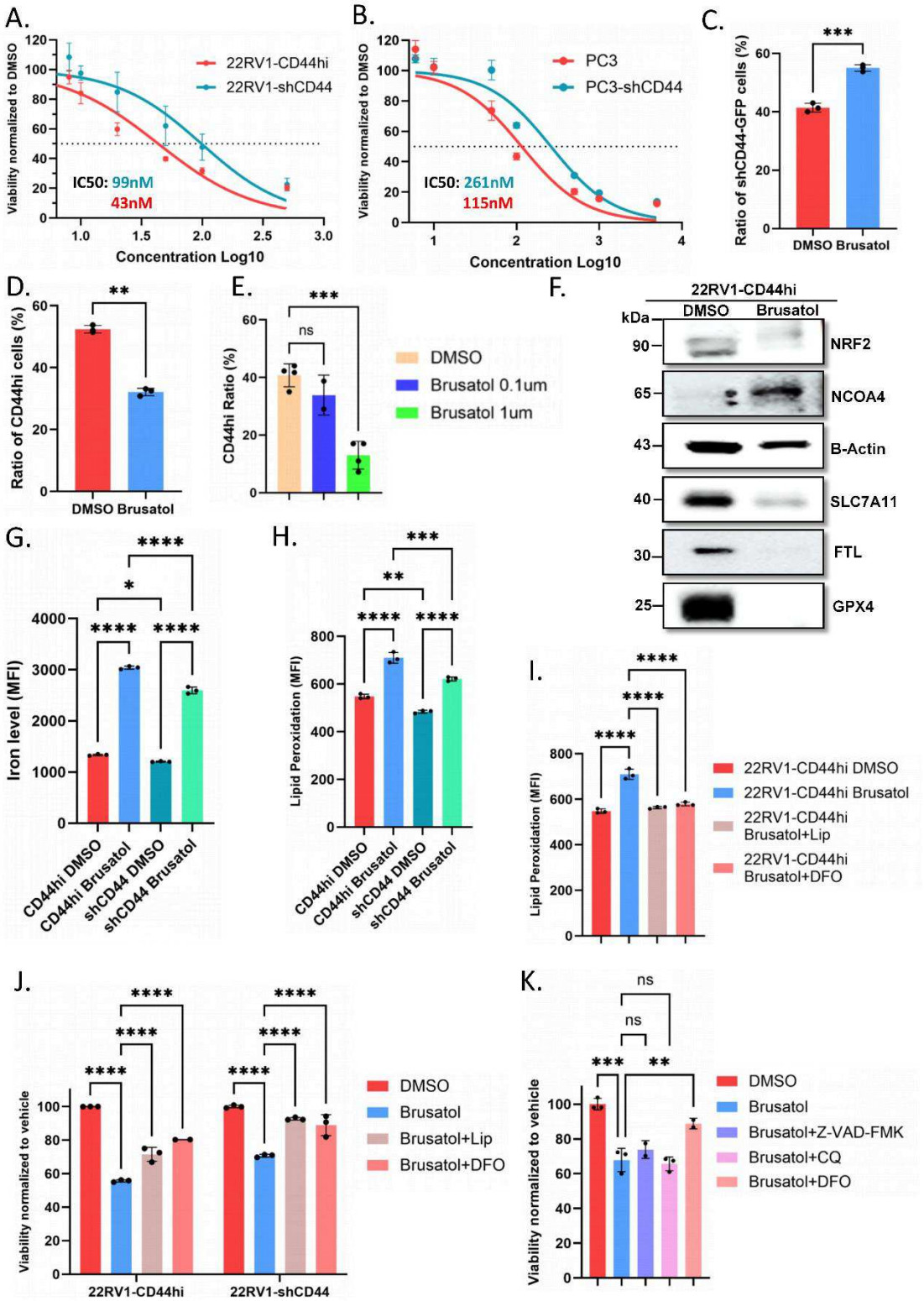


Figure 6. Pharmacological targeting of NRF2-associated defense preferentially induces ferroptotic stress in CD44hi cells

(**A**). Cell viability measured by PrestoBlue assay in 22Rv1-CD44hi-shCTR and 22Rv1-shCD44 cells following Brusatol treatment for 72 h. n=6.

(**B**). Cell viability measured by PrestoBlue assay in PC3-shCTR and PC3-shCD44 cells following Brusatol treatment for 72 h. n=6.

(**C–D**). Competitive co-culture assay in which 22Rv1-CD44hi-shCTR cells and GFP-labeled 22Rv1-CD44hi-shCD44 cells were mixed at a 1:1 ratio and treated with Brusatol (0.05 μM) or

DMSO for 72 h. The GFP-positive fraction (**C**) and CD44hi fraction (**D**) were quantified by flow cytometry to assess selective depletion of the CD44hi compartment. n=3.
(**E**). Ex vivo LAPC9 tumor tissue slices were cultured and treated with Brusatol for 4 days, followed by flow cytometric analysis of CD44 expression using an APC-conjugated anti-CD44 antibody.
(**F**). Western blot analysis of NRF2, NCOA4, SLC7A11, FTL, and GPX4 in 22Rv1-CD44hi cells treated with Brusatol (0.1 μM) for 72 h. β-Actin was used as a loading control.
(**G**). Flow cytometry analysis of intracellular labile Fe^{2+} levels using FerrOrange staining in 22Rv1-CD44hi-shCTR and 22Rv1-CD44hi-shCD44 cells treated with Brusatol (0.05 μM) for 72 h. n=3.
(**H**). Flow cytometry analysis of lipid peroxidation using C11-BODIPY staining in 22Rv1-CD44hi-shCTR and 22Rv1-CD44hi-shCD44 cells treated with Brusatol (0.1 μM) for 24 h. n=3.
(**I**). Flow cytometry analysis of C11-BODIPY staining in 22Rv1-CD44hi cells treated with Brusatol (0.1 μM), with or without Liproxstatin-1 (5 μM) or DFO (1 μM), for 24 h. n=3.
(**J**). Cell viability measured by PrestoBlue assay in 22Rv1-CD44hi-shCTR and 22Rv1-CD44hi-shCD44 cells treated with Brusatol (0.05 μM), with or without Liproxstatin-1 (1 μM) or DFO (1 μM), for 72 h. n=3.
(**K**). Cell viability measured by PrestoBlue assay in PC3 cells treated with Brusatol (0.03 μM), with or without the apoptosis inhibitor Z-VAD-FMK (20 μM), the autophagy inhibitor CQ (10 μM), or the ferroptosis inhibitor DFO (1 μM), for 72 h. n=3. Data are shown as mean ± SD. Statistical significance was determined by unpaired two-tailed t test, one-way ANOVA, or chi-square test, as appropriate. *P < 0.05, **P < 0.01, ***P < 0.001, ****P < 0.0001.

Figure 7

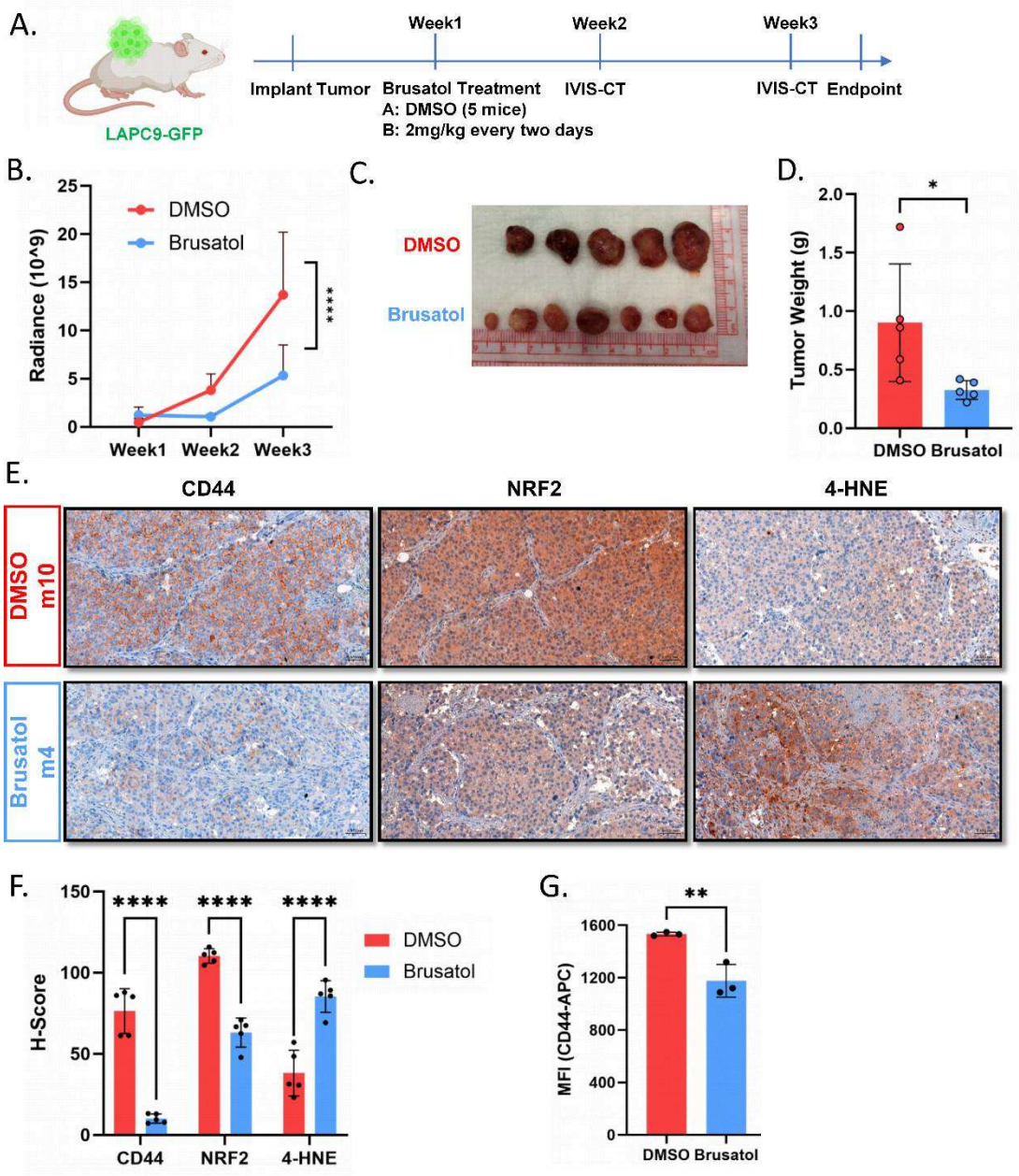


Figure 7. Brusatol suppresses LAPC9 tumor growth and increases ferroptosis-associated lipid peroxidation in vivo.

(**A**). Schematic of the in vivo Brusatol treatment experiment. Tumor-bearing mice were treated by intraperitoneal injection with vehicle, or Brusatol at 2 mg/kg every two days. n=5 mice per group.

(**B**). Longitudinal IVIS-CT imaging and quantification of luciferase radiance in vehicle and Brusatol treated tumors, showing tumor growth dynamics over time. Statistical significance was assessed using a repeated-measures mixed-effects model.

(**C–D**). Endpoint tumor volume (**C**) and tumor weight (**D**) in vehicle- and Brusatol-treated groups. n=5 mice per group.

(**E**). Representative immunohistochemical staining of NRF2, CD44, and 4-HNE in vehicle- and Brusatol-treated tumors.

(**F**). Quantification of NRF2, CD44, and 4-HNE staining by H-score analysis using ImageJ. Each dot represents one mouse. n=5 mice per group.

(**G**). Flow cytometry analysis of CD44 expression in endpoint tumors from vehicle- and Brusatol-treated groups. CD44 median fluorescence intensity (MFI) was compared between groups, Because some tumors were small and insufficient tissue remained after allocation for

histopathological analysis, flow cytometry was performed on three independent tumors per group with sufficient residual viable tissue. n=3. Data are shown as mean ± SD. Statistical significance was determined by unpaired two-tailed t test unless otherwise indicated. *P < 0.05, **P < 0.01, ***P < 0.001, ****P < 0.0001.

Figure 8

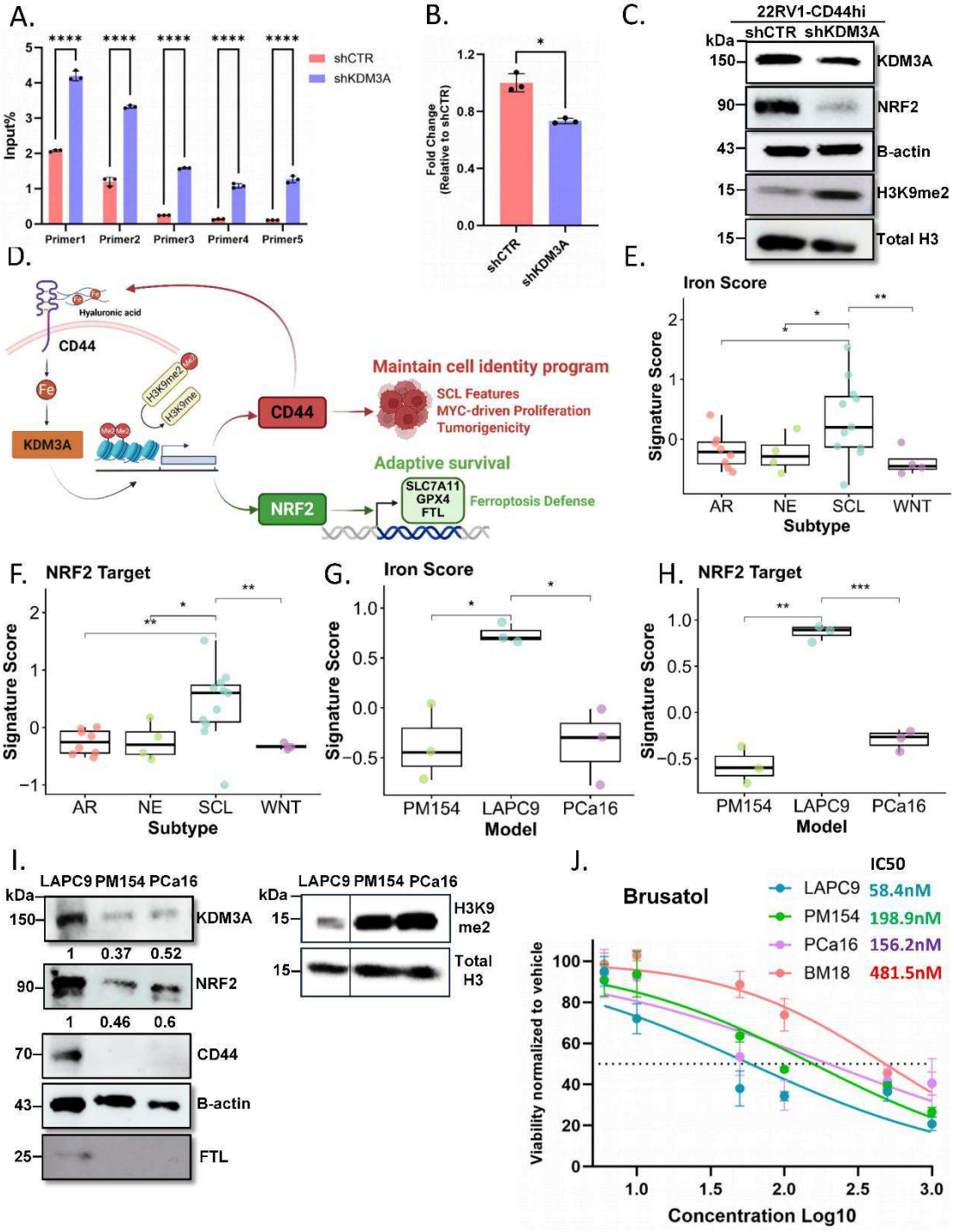


Figure 8. H3K9me2 links CD44 and NRF2 regulation and marks a Brusatol-sensitive CRPC-SCL state.

(**A**). ChIP-qPCR analysis of H3K9me2 enrichment at the NRF2 promoter in 22Rv1-CD44hi-shCTR and 22Rv1-CD44hi-shKDM3A cells.

(**B**). qRT-PCR analysis of NRF2 mRNA expression in 22Rv1-CD44hi-shCTR and 22Rv1-CD44hi-shKDM3A cells.

(**C**). Western blot analysis of NRF2 and H3K9me2 protein levels in 22Rv1-CD44hi-shCTR and 22Rv1-CD44hi-shKDM3A cells.

(**D**). Schematic summary of the iron-KDM3A-H3K9me2 axis linking CD44 expression and NRF2-mediated ferroptosis defense. CD44-associated iron accumulation supports KDM3A-dependent H3K9me2 remodeling at the CD44 and NRF2 loci. This shared chromatin-regulatory mechanism links maintenance of the CD44-associated stem-like state with NRF2-dependent

ferroptosis defense. ChIP-qPCR evidence for H3K9me2 regulation at the CD44 and NRF2 promoters is shown in Figures 3 and 8A-C.
(**E–F**). Iron signature scores (**E**) and NRF2 target signature scores (**F**) across CRPC subtype models, including AR-driven, Wnt-driven, neuroendocrine (NE), and stem cell-like (SCL) subtypes in GSE181374.
(**G-H**) Iron signature scores (**G**) and NRF2 target signature scores (**H**) across CRPC subtype models, including neuroendocrine (NE) model PM154, and stem cell-like (SCL) model LAPC9 and Wnt-driven model PCa16 organoids based on RNA-seq data.
(**I**). Baseline western blot analysis of KDM3A, NRF2, CD44, FTL, and H3K9me2 levels in LAPC9, PM154, and PCa16 organoids. Protein signals were quantified using ImageJ. Non-adjacent lanes from the same blot are separated by vertical lines.
(**J**). Cell viability of prostate cancer organoids representing distinct CRPC subtypes, including AR-dependent BM18, Wnt-driven PCa16, NE PM154, and SCL-like LAPC9, following Brusatol treatment for 48 h in NAC-free treatment medium. Data are shown as mean ± SD. Statistical significance was determined by unpaired two-tailed t test or one-way ANOVA, as appropriate. *P < 0.05, **P < 0.01, ***P < 0.001, ****P < 0.0001.

Figure 9

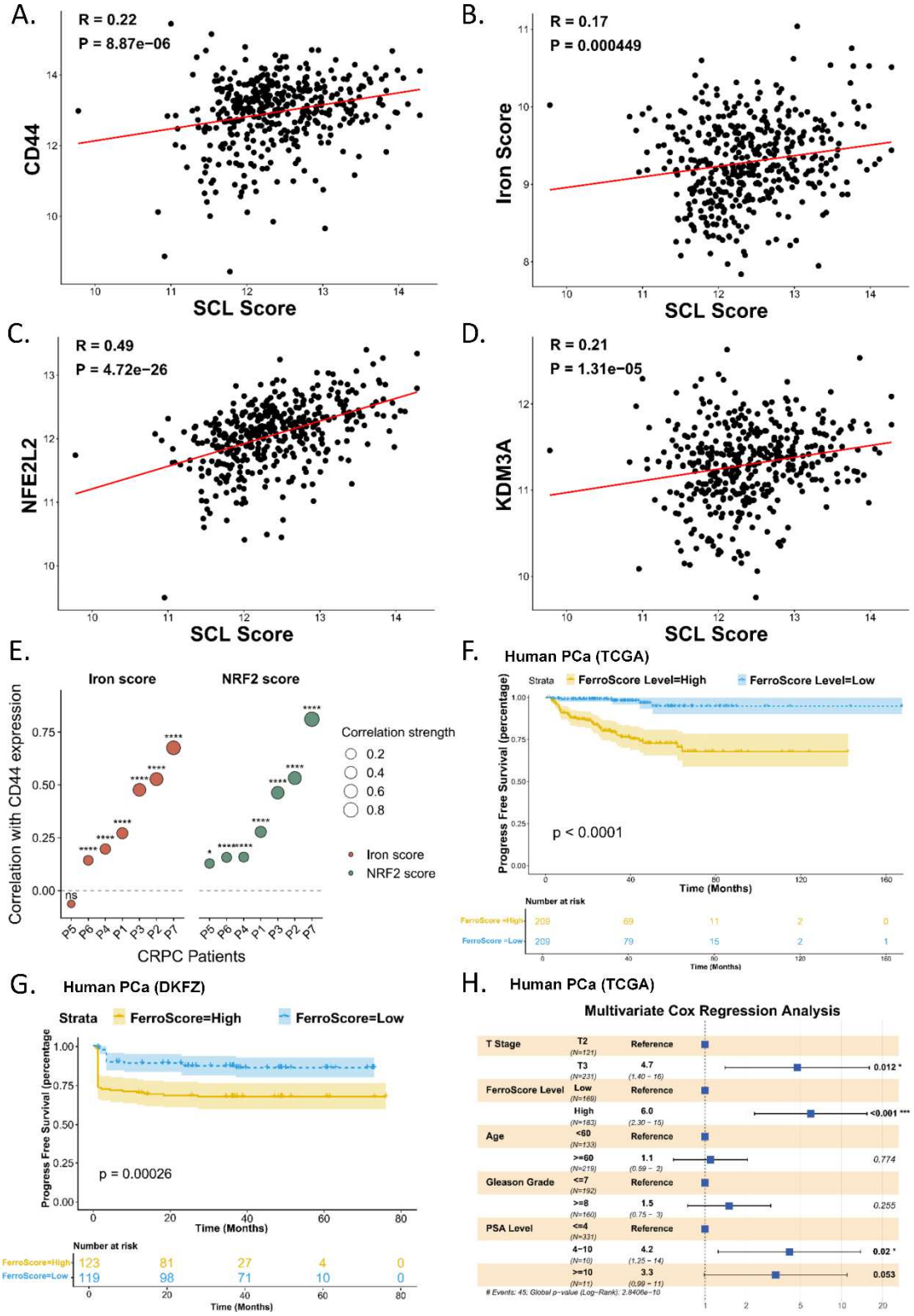


Figure 9. Patient analyses support a CD44-associated iron/NRF2 program and a related prognostic multigene score in prostate cancer.
(**A–D**). CD44 was excluded from the SCL and iron signatures for correlation analyses involving CD44 expression to avoid circularity. Spearman correlation analyses in the TCGA prostate cancer cohort (n=418) showing associations between SCL score and CD44 expression (**A**), iron score (**B**), NFE2L2/NRF2 expression (**C**), and KDM3A expression (**D**).

(**E**). Bubble plot showing sample-wise correlations between CD44 expression and iron or NRF2 scores in epithelial cells from seven CRPC scRNA-seq patient samples, including four from GSE137829 and three from GSE210358. Correlations were calculated independently within each patient sample. Bubble size indicates correlation strength, and asterisks indicate Spearman correlation significance. CD44 was excluded from the iron score to avoid circularity.
(**F**). Kaplan-Meier analysis of biochemical recurrence-free survival in the TCGA cohort stratified at the cohort-specific median into FerroScore-high and FerroScore-low groups. FerroScore-high patients showed increased biochemical recurrence compared with FerroScore-low patients.
(**G**) Kaplan–Meier analysis of biochemical recurrence-free survival in the DKFZ prostate cancer cohort (n=242) stratified at the cohort-specific median into FerroScore-high and FerroScore-low groups. FerroScore was calculated using the coefficients derived from the TCGA cohort and applied to the DKFZ dataset without refitting. FerroScore-high patients showed increased biochemical recurrence compared with FerroScore-low patients.
(**H**). Multivariate Cox regression analysis of biochemical recurrence in the TCGA cohort (n=352), adjusting for Gleason grade, PSA level, age, and T stage. FerroScore was evaluated as a dichotomous variable, with patients stratified into FerroScore-high and FerroScore-low groups using the cohort-specific median as the cutoff, remained significantly associated with worse biochemical recurrence (HR 5.96, 95% CI 2.30–15.41, P = 0.00023). Data are shown as mean ± SD where applicable. Statistical significance was determined by Spearman correlation analysis, multivariable Cox regression and log-rank test, as appropriate. *P < 0.05, **P < 0.01, ***P < 0.001, ****P < 0.0001.

Figure 10

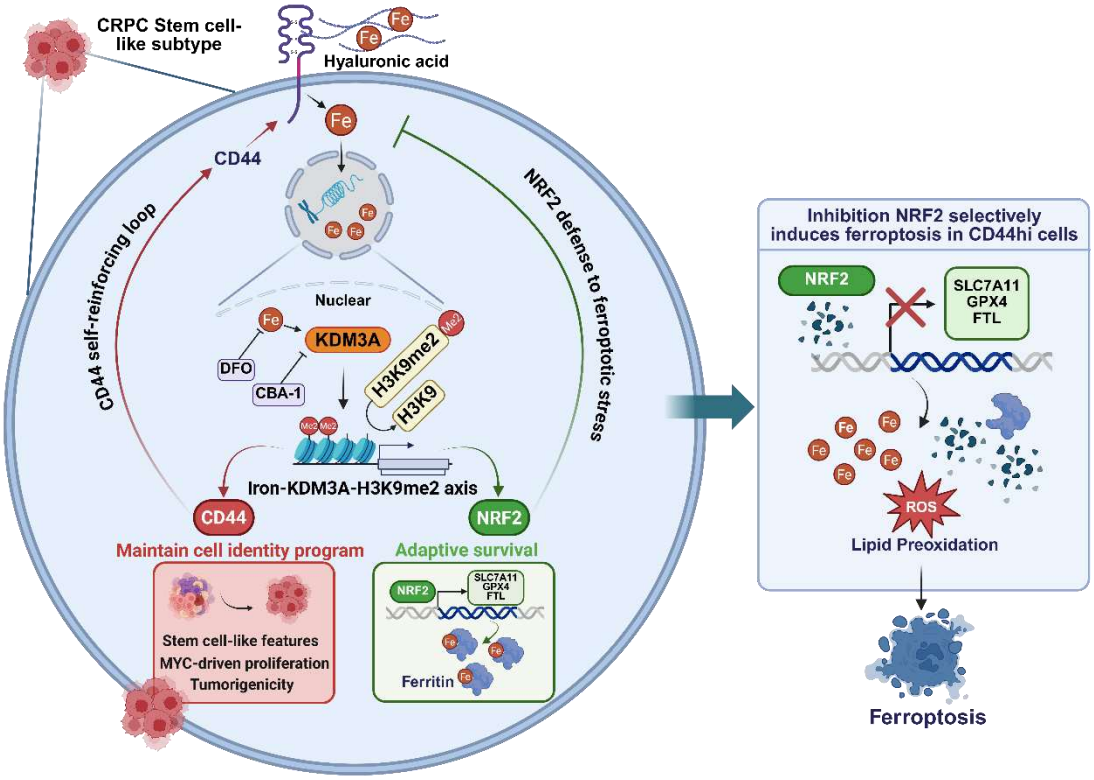
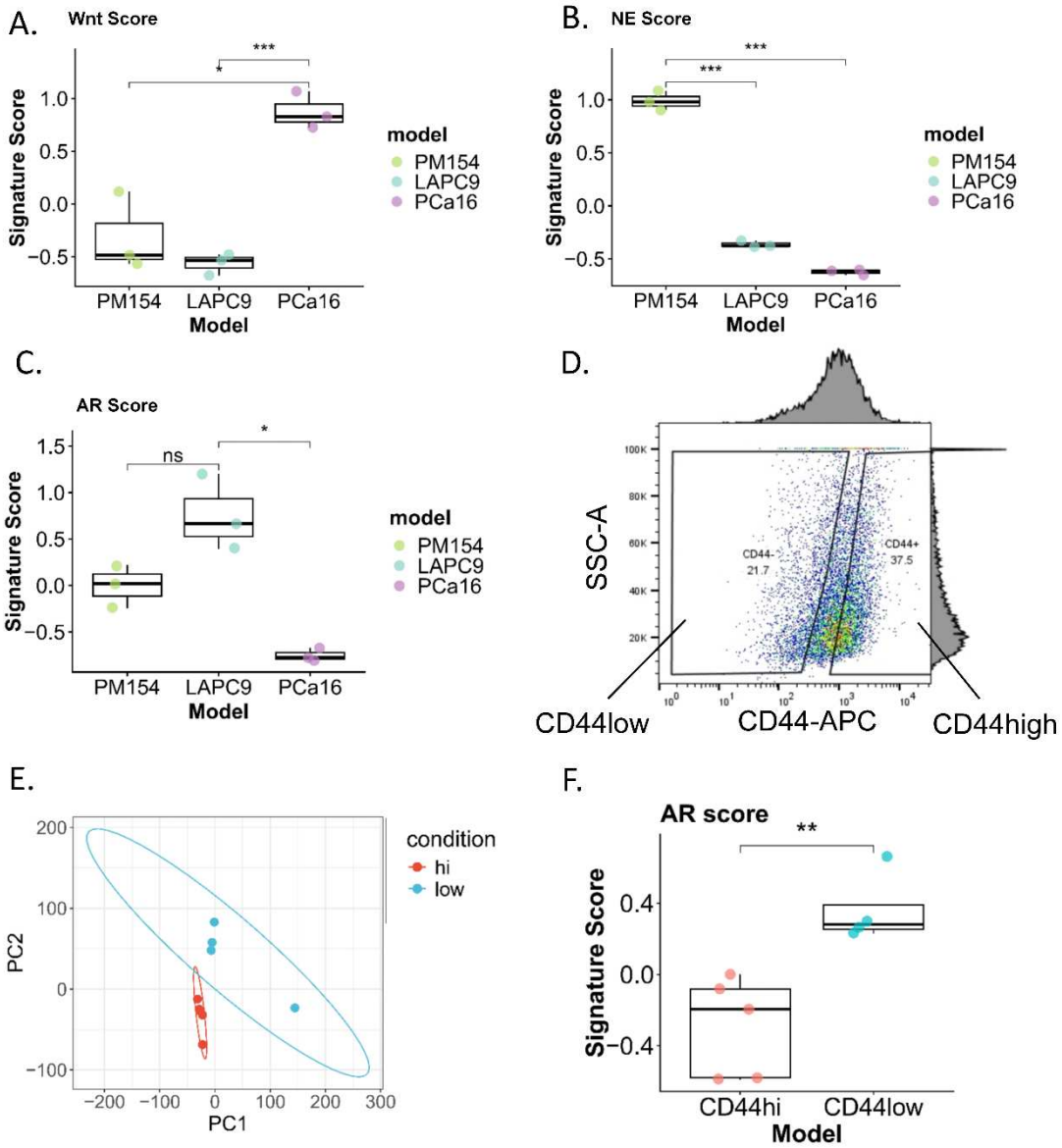


Figure 10. The iron-KDM3A-H3K9me2 axis links a CD44-associated stem-like state to ferroptosis vulnerability in aggressive prostate cancer.
CD44-associated iron accumulation provides Fe^{2+} that supports KDM3A-dependent H3K9me2 remodeling at the CD44 and NRF2 loci. This shared chromatin-regulatory mechanism contributes to maintenance of CD44 expression, the associated stem-like transcriptional program, and NRF2-mediated ferroptosis defense. At the same time, elevated intracellular iron increases ferroptotic stress, which CD44hi cells tolerate through NRF2-mediated antioxidant protection, including GPX4, SLC7A11, and FTL. Pharmacological disruption of this adaptive defense with Brusatol increases the labile iron pool, enhances lipid peroxidation, and preferentially sensitizes CD44hi cells to ferroptotic stress. Together, these findings support the iron-KDM3A-H3K9me2 axis as a mechanistic link between maintenance of the CD44-associated CRPC-SCL state and its increased reliance on NRF2-mediated ferroptosis defense.

Supplementary Figure 1



Supplementary Figure 1. CRPC subtype signature characterization and transcriptional profiling of LAPC9 CD44hi and CD44low cells.

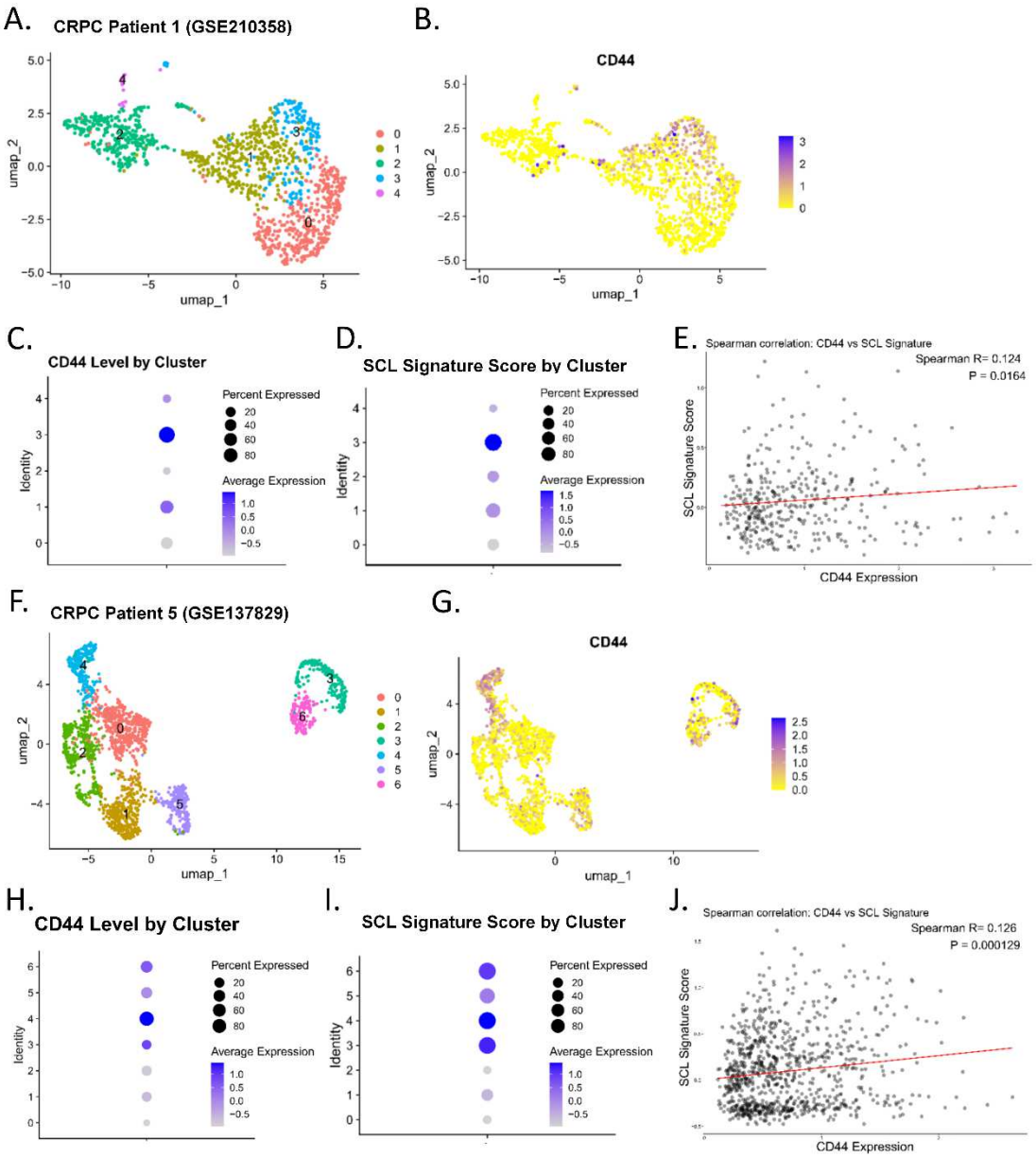
(**A–C**) NE (**A**), Wnt (**B**), and AR (**C**) signature scores calculated from RNA-seq data of LAPC9, PCa16, and PM154 organoids.

(**D**) Flow cytometry sorting strategy used to isolate CD44hi and CD44low subpopulations from LAPC9 cells.

(**E**) Principal component analysis (PCA) of RNA-seq data from FACS sored LAPC9 CD44hi and CD44low cells, showing transcriptional separation between CD44hi and CD44low subpopulations.

(**F**) AR signature scores in LAPC9 CD44hi and CD44low cells based on RNA-seq analysis. Data are shown as mean ± SD. Statistical significance was determined by unpaired two-tailed t test or one-way ANOVA, as appropriate. *P < 0.05, **P < 0.01, ***P < 0.001, ****P < 0.0001.

Supplementary Figure 2



Supplementary Figure 2. CD44-enriched epithelial cell states exhibit SCL features in CRPC patient single-cell datasets.

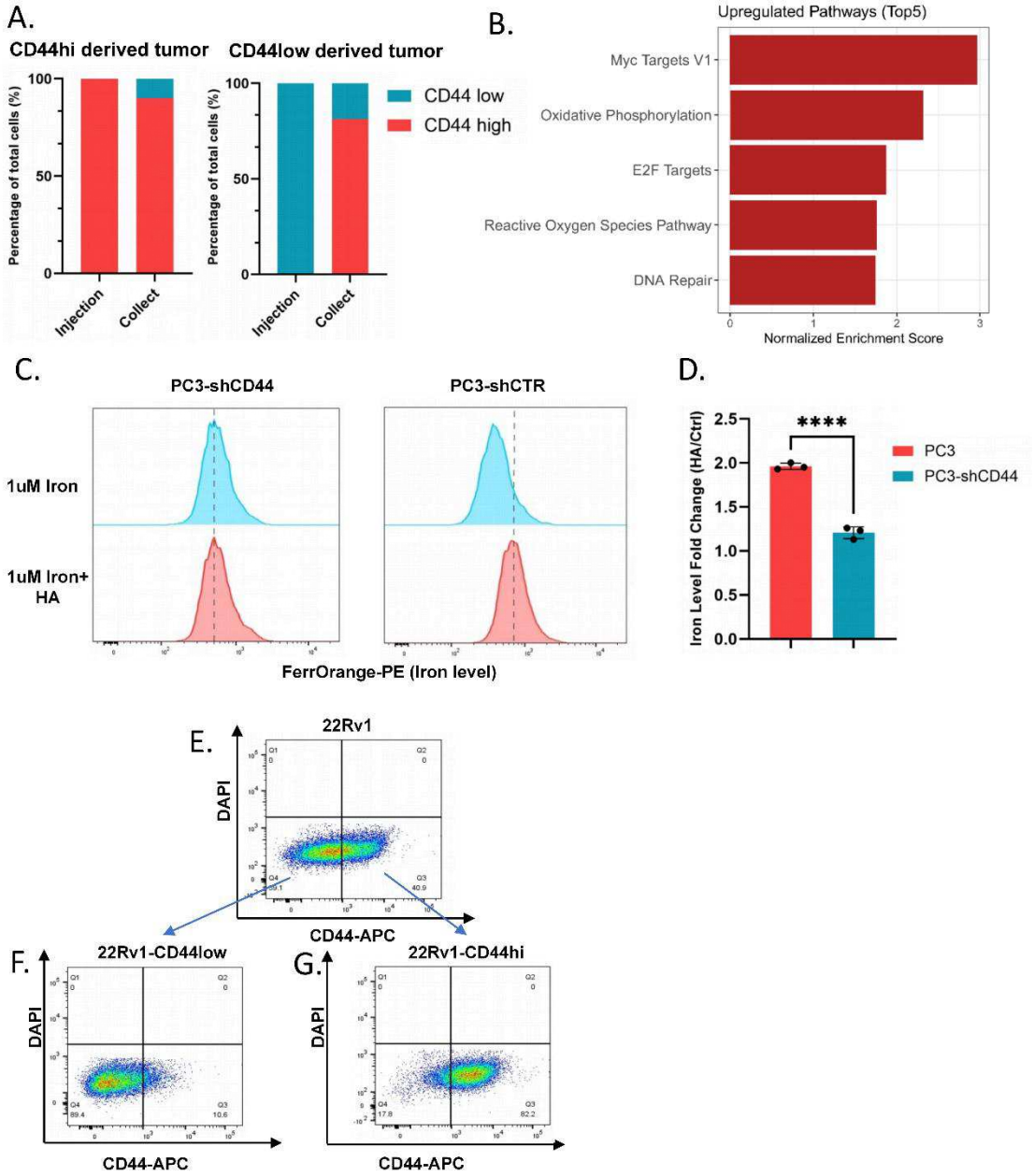
(**A**) UMAP visualization of epithelial cell clusters from CRPC patient 1 in GSE210358, analyzed using the Seurat workflow.

(**B–E**) CD44 expression and SCL signature analysis in epithelial cells from CRPC patient 1. CD44 distribution in UMAP shown in (**B**). CD44 expression across clusters is shown by dot plot (**C**), SCL signature score across clusters is shown by dot plot (**D**), and Spearman correlation analysis between CD44 expression and SCL signature score is shown in (**E**). CD44 was excluded from the SCL score to avoid circularity.

(**F**) UMAP visualization of epithelial cell clusters from CRPC patient 5 in GSE137829, analyzed using the Seurat workflow.

(**G–J**) CD44 expression and SCL signature analysis in epithelial cells from CRPC patient 5. CD44 distribution in UMAP shown in (**G**). CD44 expression across clusters is shown by dot plot (**H**), SCL signature score across clusters is shown by dot plot (**I**), and Spearman correlation analysis between CD44 expression and SCL signature score is shown in (**J**). CD44 was excluded from the SCL score to avoid circularity.

Supplementary Figure 3



Supplementary Figure 3. Additional characterization of CD44hi transcriptional features and CD44-associated iron accumulation.

(**A**) Flow cytometry analysis of CD44 expression in endpoint tumors derived from sorted LAPC9 CD44hi or CD44low cells.

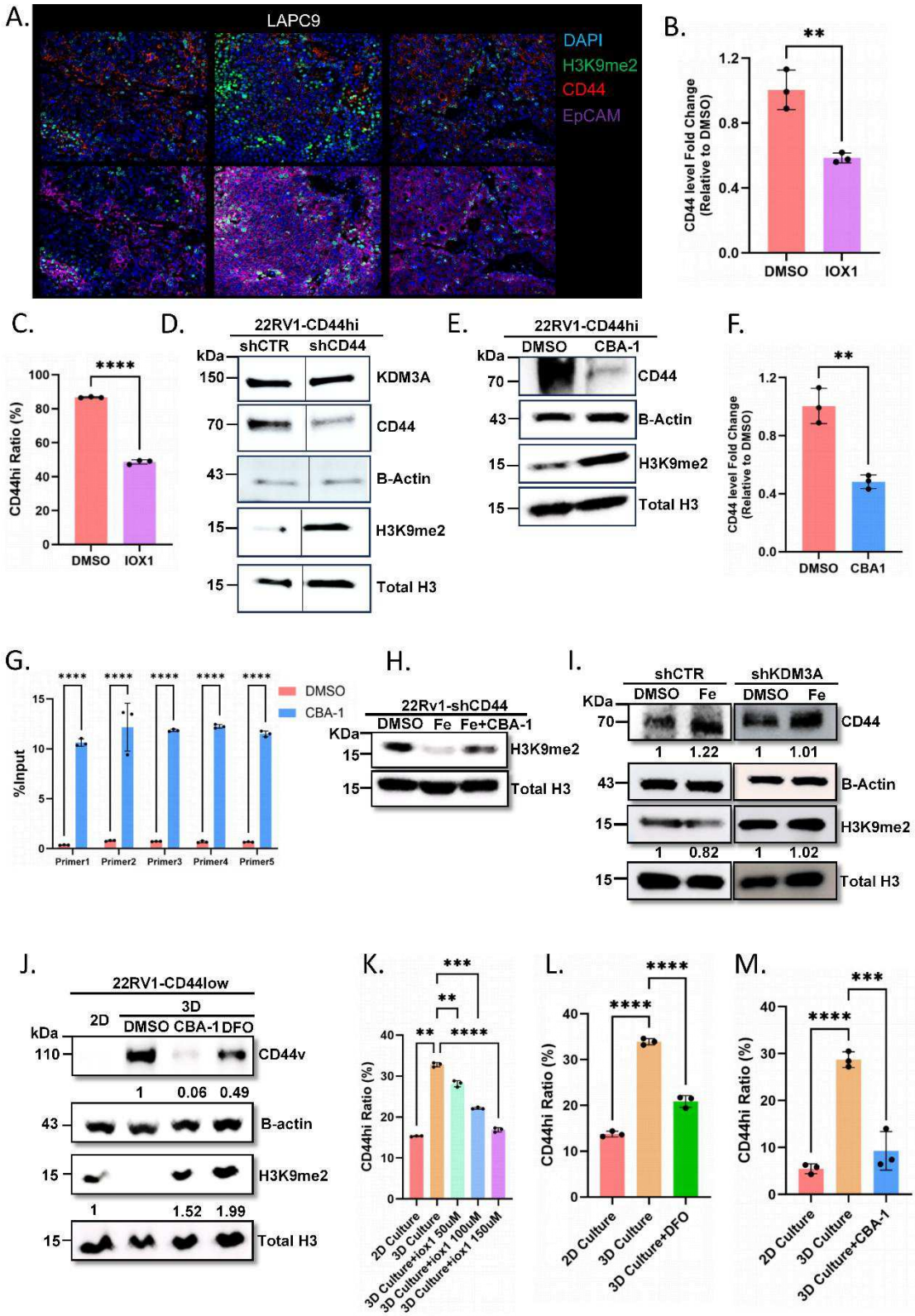
(**B**) Pathway enrichment analysis showing representative pathways enriched in the LAPC9 CD44hi subpopulation.

(**C-D**) Flow cytometry analysis of FerrOrange staining in PC3-shCTR and PC3-shCD44 cells treated with iron (1 μM), with or without hyaluronic acid (HA, 1 mg/ml), for 48 h to assess intracellular labile Fe^{2+} levels.

(**E**) Flow cytometry sorting strategy used to isolate CD44hi and CD44low subpopulations from 22Rv1 cells.

(**F–G**) Establishment and maintenance of sorted 22Rv1-CD44low (**F**) and 22Rv1-CD44hi (**G**) cell populations in culture. Data are shown as mean ± SD. Statistical significance was determined by unpaired two-tailed t test or one-way ANOVA, as appropriate. *P < 0.05, **P < 0.01, ***P < 0.001, ****P < 0.0001.

Supplementary Figure 4



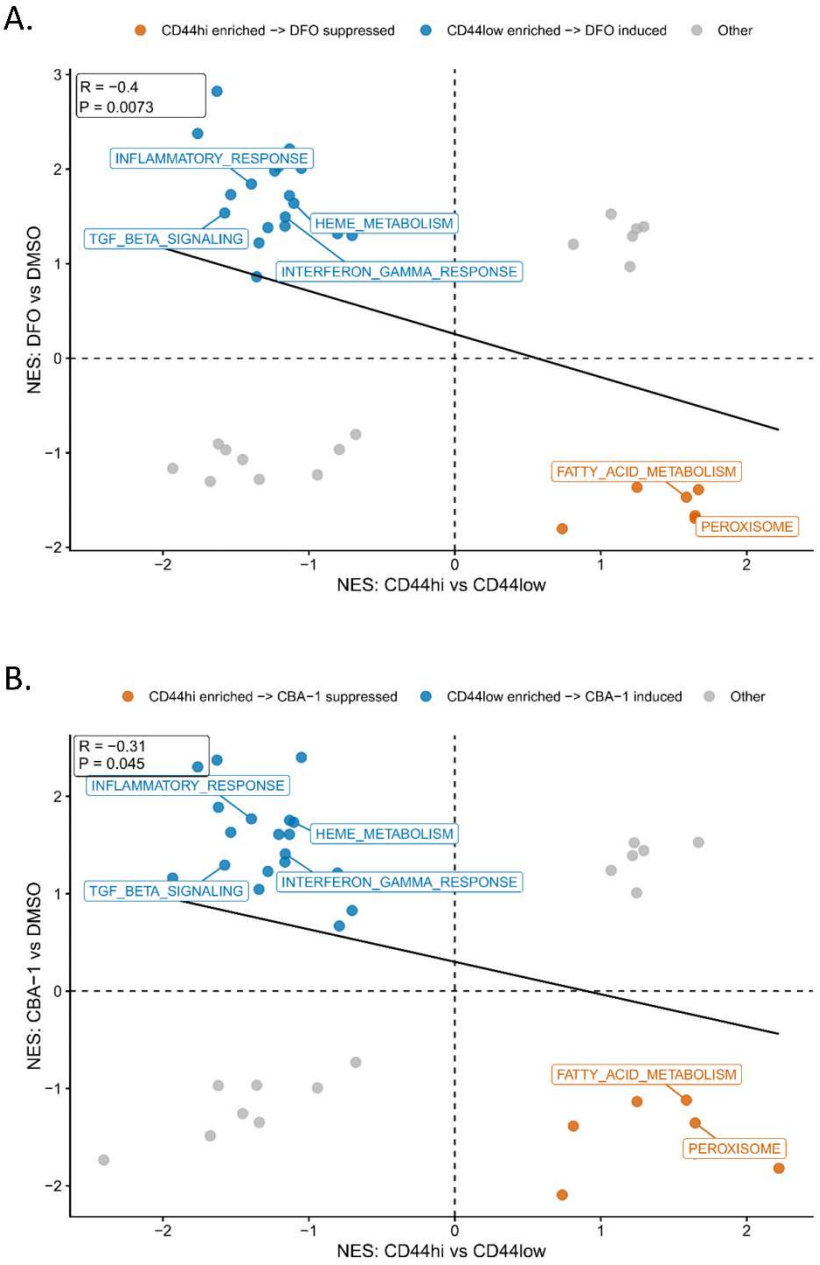
Supplementary Figure 4. Additional validation of H3K9me2 regulation and CD44 re-expression.

(**A**) Immunofluorescence co-staining of CD44 and H3K9me2 (upper row) and EpCAM and H3K9me2 (lower row) in LAPC9 tumors. The same fields are shown in both rows.

(**B**) qRT-PCR analysis of CD44 mRNA expression in 22Rv1-CD44hi cells treated with the pan-H3K9 demethylase inhibitor IOX1 (100 μM) for 72 h.

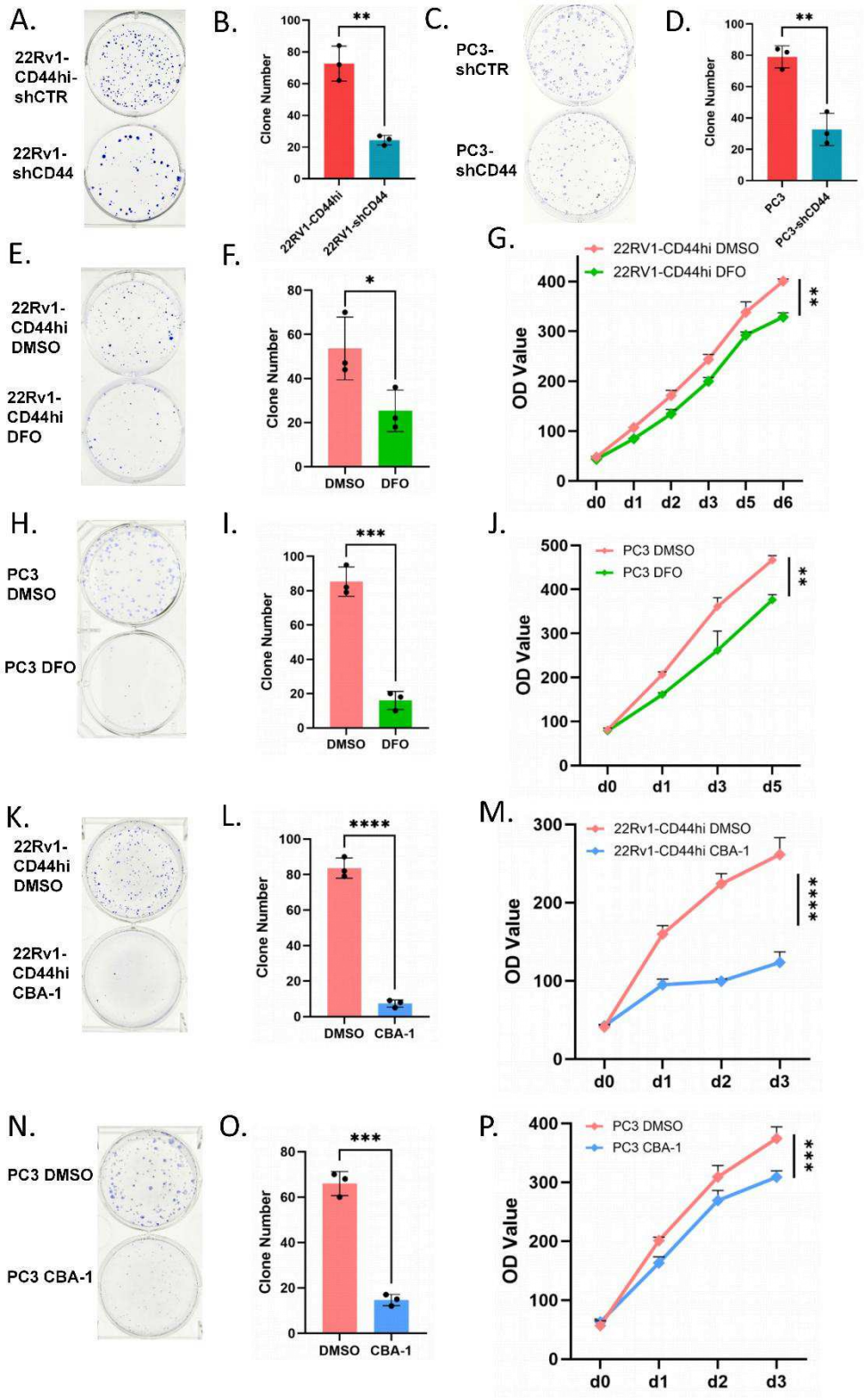
(**C**) Flow cytometry analysis of CD44 expression in 22Rv1-CD44hi cells treated with or without IOX1 (100 μM) for 72 h using an APC-conjugated anti-CD44 antibody. The percentage of CD44hi cells was compared between groups.
(**D**) Western blot analysis of KDM3A, CD44, and H3K9me2 protein levels in 22Rv1-CD44hi-shCTR and 22Rv1-shCD44 cells. Non-adjacent lanes from the same blot are separated by vertical lines.
(**E–F**) Western blot analysis of CD44 and H3K9me2 protein levels (**E**) and qRT-PCR analysis of CD44 mRNA expression (**F**) in 22Rv1-CD44hi cells treated with CBA-1 for 72 h. CBA-1 was used at 2 μM for western blot analysis and 1 μM for qRT-PCR analysis.
(**G**) ChIP-qPCR analysis of H3K9me2 enrichment at the CD44 promoter in 22Rv1-CD44hi cells treated with CBA-1 (3 μM) for 72 h.
(**H**) Western blot analysis of H3K9me2 in 22Rv1-CD44hi-shCD44 cells treated with apo-transferrin (3ug/ml)+DMSO, holo-transferrin (3ug/ml) or holo-transferrin (3ug/ml)+CBA-1 (1uM) for 48h.
(**I**) Western blot analysis of NRF2, CD44 and H3K9me2 in 22Rv1-CD44hi-shCTR and 22Rv1-CD44hi-shKDM3A cells treated with apo-transferrin (3ug/ml)+DMSO or holo-transferrin (3ug/ml) for 48h.
(**J**) Western blot analysis of H3K9me2 and CD44 in 22Rv1-CD44low cells cultured under 2D or 3D organoid conditions for 3 days, with or without CBA-1 (30 μM) or DFO (50 μM), showing that inhibition of the iron-KDM3A axis prevents CD44 reactivation under 3D culture conditions.
(**K**) Flow cytometry analysis of CD44 expression in 22Rv1-CD44low cells cultured under 2D or 3D organoid conditions for 3 days, with or without IOX1. The percentage of CD44hi cells was compared among groups. n=3.
(**L**) Flow cytometry analysis of CD44 expression in 22Rv1-CD44low cells cultured under 2D or 3D organoid conditions for 3 days, with or without DFO (30 μM). The percentage of CD44hi cells was compared among groups. n=3.
(**M**) Flow cytometry analysis of CD44 expression in 22Rv1-CD44low cells cultured under 2D or 3D organoid conditions for 3 days, with or without CBA-1 (50 μM). The percentage of CD44hi cells was compared among groups. n=3. Data are shown as mean ± SD. Statistical significance was determined by unpaired two-tailed t test or one-way ANOVA, as appropriate. *P < 0.05, **P < 0.01, ***P < 0.001, ****P < 0.0001.

Supplementary Figure 5



Supplementary Figure 5. Inverse pathway relationships persist after exclusion of proliferation-associated gene sets.
(**A-B**). Correlation of Hallmark pathway enrichment after exclusion of proliferation-associated gene sets. E2F Targets, G2M Checkpoint, MYC Targets V1, MYC Targets V2, Mitotic Spindle, and mTORC1 Signaling were excluded, and Pearson correlation was performed between the normalized enrichment scores (NES) from the CD44hi versus CD44low comparison and those from DFO-treated (**A**) or CBA-1-treated (**B**) versus control organoids across the remaining Hallmark pathways.

Supplementary Figure 6



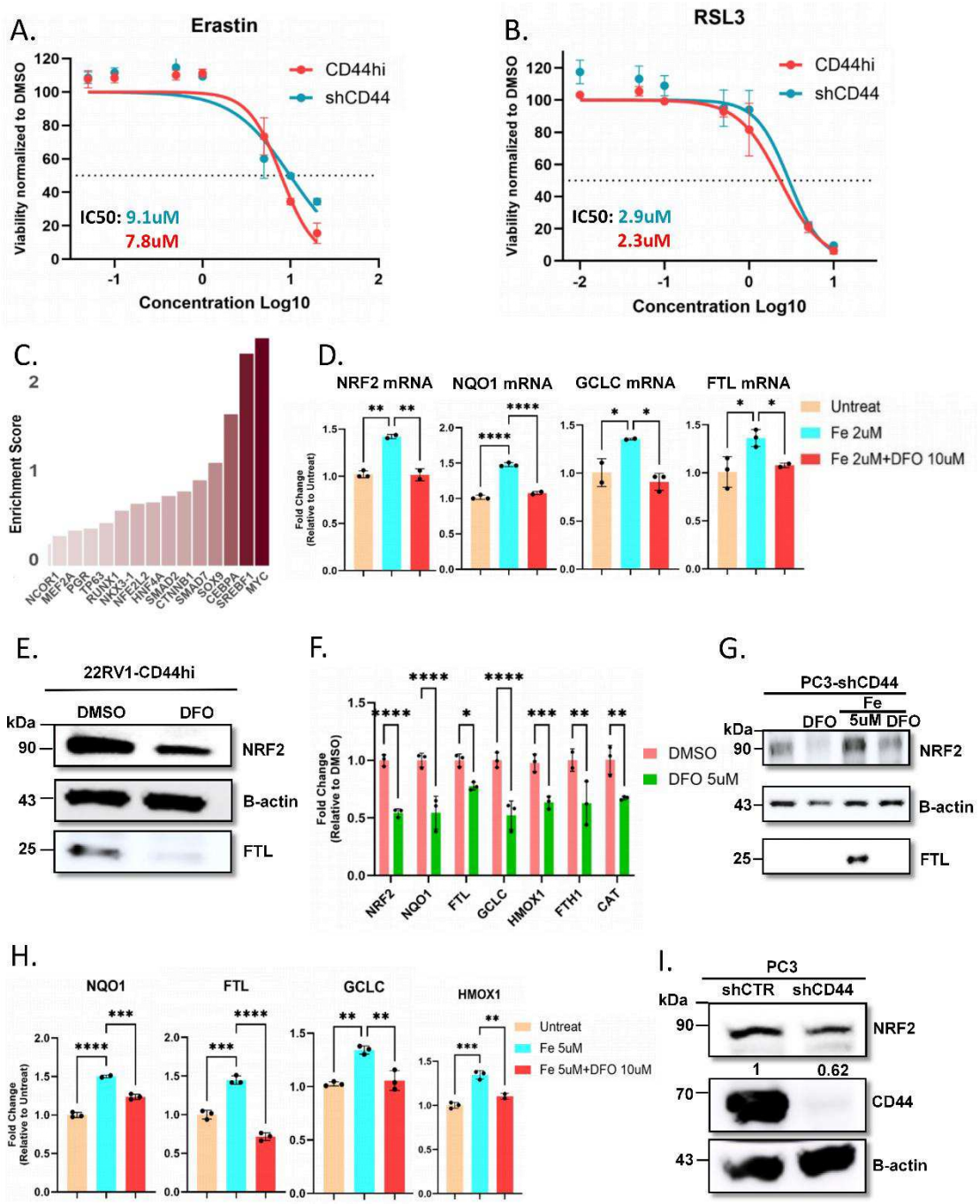
Supplementary Figure 6. CD44-associated clonogenic growth is suppressed by iron chelation and KDM3A inhibition.

(**A–B**). Representative clonogenic assay images (**A**) and quantification of colony number (**B**) in 22Rv1-CD44hi-shCTR and 22Rv1-CD44hi-shCD44 cells. Cells were seeded at 1,000 cells per well. n=3.

(**C–D**). Representative clonogenic assay images (**C**) and quantification of colony number (**D**) in

PC3-shCTR and PC3-shCD44 cells. Cells were seeded at 500 cells per well. n=3.
(**E–F**). Representative clonogenic assay images (**E**) and quantification of colony number (**F**) in 22Rv1-CD44hi cells pretreated with DMSO or DFO (10 μM) for 72 h before seeding. Cells were seeded at 1,000 cells per well. n=3.
(**G**) Growth curve of 22Rv1-CD44hi cells treated with DMSO or DFO (10 μM), measured by PrestoBlue assay. n=4.
(**H–I**) Representative clonogenic assay images (**H**) and quantification of colony number (**I**) in PC3 cells pretreated with DMSO or DFO (10 μM) for 72 h before seeding. Cells were seeded at 500 cells per well.
(**J**) Growth curve of PC3 cells treated with DMSO or DFO (10 μM), measured by PrestoBlue assay. n=4.
(**K–L**) Representative clonogenic assay images (**K**) and quantification of colony number (**L**) in 22Rv1-CD44hi cells pretreated with DMSO or CBA-1 (2 μM) for 72 h before seeding. Cells were seeded at 1,000 cells per well. n=3.
(**M**) Growth curve of 22Rv1-CD44hi cells treated with DMSO or CBA-1 (2 μM), measured by PrestoBlue assay. n=5.
(**N–O**) Representative clonogenic assay images (**N**) and quantification of colony number (**O**) in PC3 cells pretreated with DMSO or CBA-1 for 72 h before seeding. Cells were seeded at 500 cells per well.
(**P**) Growth curve of PC3 cells treated with DMSO or CBA-1, measured by PrestoBlue assay. n=5. Data are shown as mean ± SD. Statistical significance was determined by unpaired two-tailed t test unless otherwise indicated. *P < 0.05, **P < 0.01, ***P < 0.001, ****P < 0.0001.

Supplementary Figure 7



Supplementary Figure 7. Additional validation of NRF2 pathway activation and ferroptosis response in CD44-associated cells.

(**A–B**) Dose-response viability analysis of 22Rv1-CD44hi and 22Rv1-shCD44 cells following treatment with the ferroptosis inducers Erastin (**A**) or RSL3 (**B**) for 48 h. These assays show that CD44hi cells are not uniformly more sensitive to conventional ferroptosis induction, supporting the rationale for targeting the NRF2-mediated ferroptosis-defense program. n = 6.

(**C**) VIPER master regulator analysis based on RNA-seq differential expression between sorted LAPC9 CD44hi and CD44low cells under intact conditions, identifying candidate transcriptional regulators enriched in the CD44hi subpopulation.

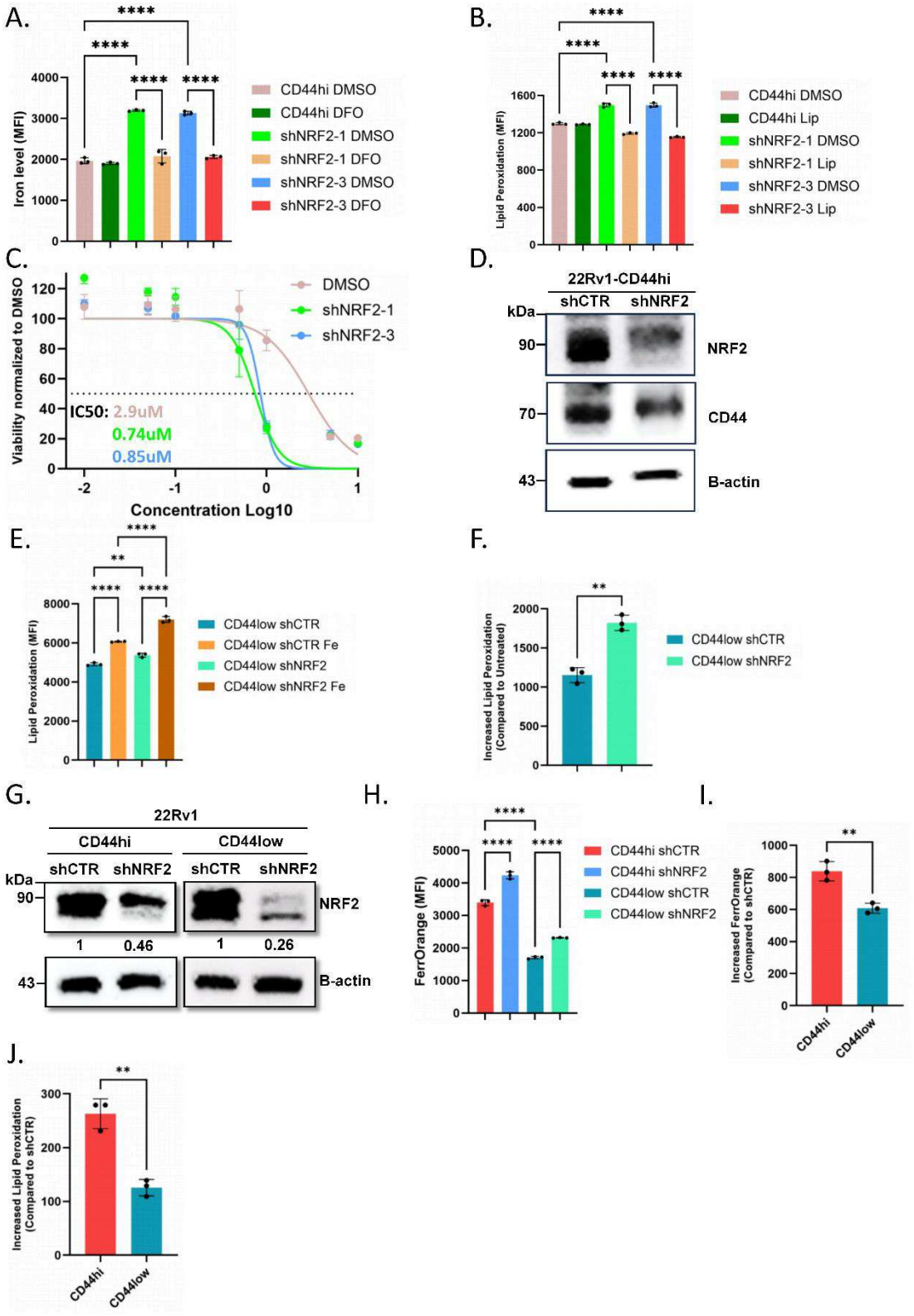
(**D**) qRT-PCR analysis of NRF2 downstream target genes in 22Rv1-shCD44 cells treated with iron (2 μM), with or without DFO (10 μM), for 72 h. n=3.

(**E**) Western blot analysis of CD44 and NRF2 protein levels in 22Rv1-CD44hi cells treated with or without DFO (10 μM) for 72 h. β-Actin was used as a loading control.

(**F**) qRT-PCR analysis of NRF2 downstream target genes in 22Rv1-CD44hi cells treated with

or without DFO (10 μM) for 72 h. n=3.
(**G**) Western blot analysis of NRF2 and FTL protein levels in PC3 cells treated with iron (5 μM), with or without DFO (10 μM), for 72 h.
(**H**) qRT-PCR analysis of NRF2 downstream target genes in PC3 cells treated with iron (5 μM), with or without DFO (10 μM), for 72 h.
(**I**) Western blot analysis of NRF2 protein levels in PC3-shCTR and PC3-shCD44 cells. Statistical significance was determined by unpaired two-tailed t test or one-way ANOVA, as appropriate. *P < 0.05, **P < 0.01, ***P < 0.001, ****P < 0.0001.

Supplementary Figure 8



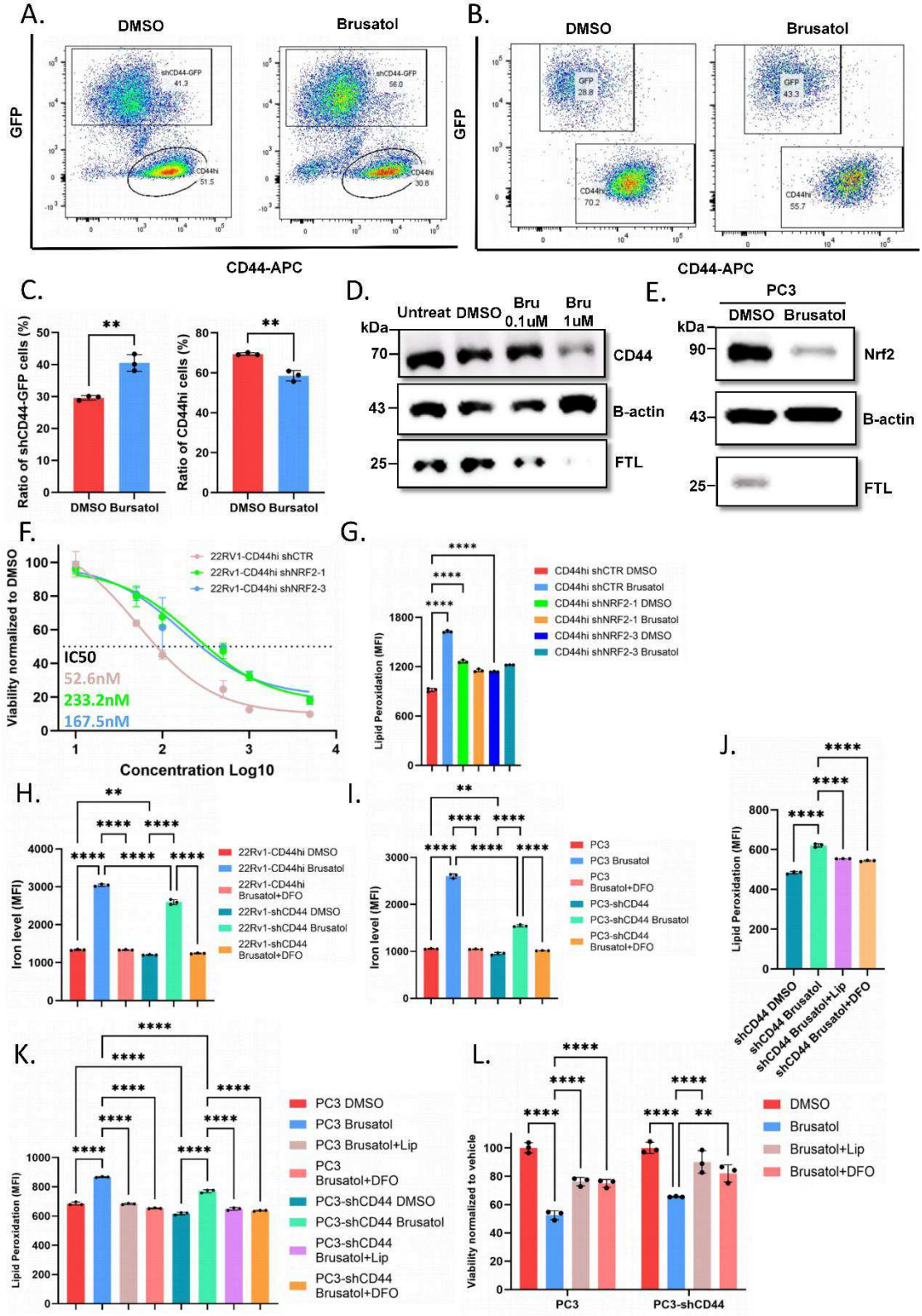
Supplementary Figure 8. Consequences of NRF2 depletion for labile iron, lipid peroxidation and ferroptosis sensitivity in CD44hi and CD44low cells.

(**A**) Flow cytometry analysis of labile Fe^{2+} levels using FerrOrange staining in 22Rv1-CD44hi-shCTR, 22Rv1-shNRF2-1, and 22Rv1-shNRF2-3 cells. n = 3.

(**B**) Flow cytometry analysis of lipid peroxidation using C11-BODIPY staining in 22Rv1-CD44hi-shCTR, 22Rv1-shNRF2-1, and 22Rv1-shNRF2-3 cells. n = 3.

(**C**) Cell viability measured by PrestoBlue assay in 22Rv1-CD44hi-shCTR, 22Rv1-shNRF2-1, and 22Rv1-shNRF2-3 cells following RSL3 treatment for 48 h. n = 4.
(**D**) Western blot analysis of CD44 and NRF2 in 22Rv1-CD44hi-shCTR and 22Rv1-CD44hi-shNRF2-3 cells, β-Actin was used as a loading control.
(**E**) Flow cytometry analysis of lipid peroxidation using C11-BODIPY staining in 22Rv1-CD44low-shCTR and shNRF2 cells, treated with or without iron (5 μM) for 24h. n = 3.
(**F**) Comparison of the increase in C11-BODIPY oxidation following iron treatment (5 μM) in CD44low-shCTR and CD44low-shNRF2 cells, calculated relative to the corresponding shCTR cells. n = 3.
(**G**). Western blot analysis of NRF2 levels between 22Rv1-CD44hi-shCTR and 22Rv1-CD44hi-shNRF2 cells; between 22Rv1-CD44low-shCTR and 22Rv1-CD44low-shNRF2 cells. Protein signals were quantified using ImageJ.
(**H**) Flow cytometry analysis of labile Fe^{2+} levels using FerrOrange staining in 22Rv1-CD44hi-shCTR, 22Rv1-CD44hi-shNRF2, 22Rv1-CD44low-shCTR and 22Rv1-CD44low-shNRF2 cells. n = 3.
(**I**) Comparison of the increase in labile Fe^{2+} levels FerrOrange staining following NRF2 depletion in CD44hi and CD44low cells, calculated relative to the corresponding shCTR cells. n = 3 biological replicates.
(**J**) Comparison of the increase in C11-BODIPY oxidation following NRF2 depletion in CD44hi and CD44low cells, calculated relative to the corresponding shCTR cells. n = 3 biological replicates. Data are shown as mean ± SD. Statistical significance was determined by unpaired two-tailed t test or one-way ANOVA, as appropriate. *P < 0.05, **P < 0.01, ***P < 0.001, ****P < 0.0001.

Supplementary Figure 9

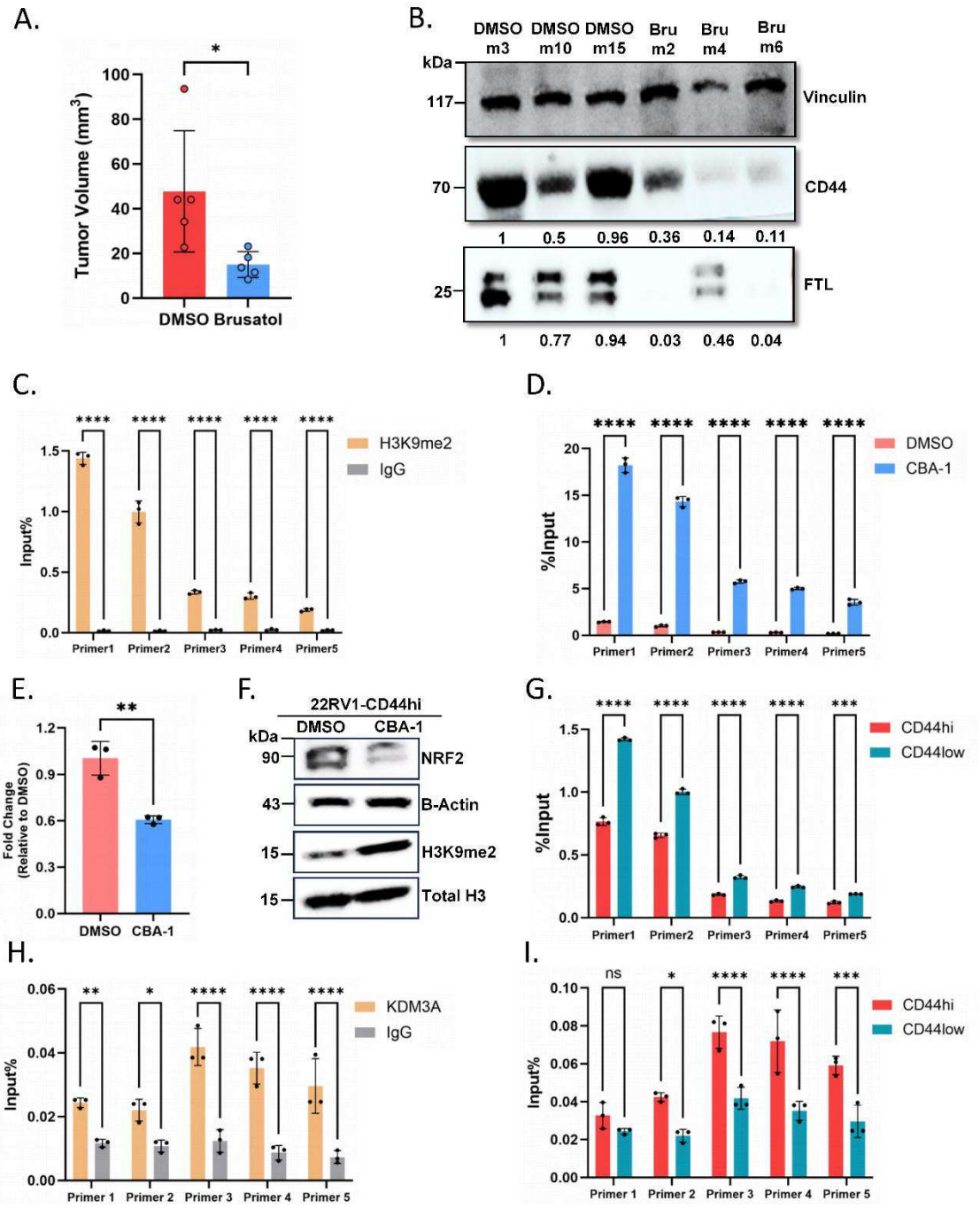


Supplementary Figure 9. Additional validation of Brusatol-induced ferroptotic stress and CD44hi cell depletion.

(**A**) Competitive co-culture assay in which 22Rv1-CD44hi cells and GFP-labeled 22Rv1-shCD44 cells were mixed at a 1:1 ratio and treated with Brusatol (0.05 μM) or DMSO for 72 h. Flow cytometry was performed to assess changes in GFP-positive and CD44hi fractions. (**B**) Competitive co-culture assay in which PC3 cells and GFP-labeled PC3-shCD44 cells were

mixed at a 1:1 ratio and treated with Brusatol (0.1 μM) or DMSO for 72 h. Flow cytometry was performed to assess changes in GFP-positive and CD44hi fractions.
(**C**) Quantification of GFP-positive and CD44hi fractions from the competitive co-culture assays shown in (A–B).
(**D**) Ex vivo LAPC9 tumor tissue slices were cultured and treated with Brusatol for 4 days, followed by western blot analysis.
(**E**) Western blot analysis of NRF2 and FTL protein levels in PC3 cells treated with Brusatol (0.1 μM) for 72 h.
(**F**) Cell viability measured by PrestoBlue assay in 22Rv1-CD44hi-shCTR, 22Rv1-shNRF2-1, and 22Rv1-shNRF2-3 cells following Brusatol treatment for 48h. n = 4.
(**G**) Flow cytometry analysis of lipid peroxidation using C11-BODIPY staining in 22Rv1-CD44hi-shCTR, 22Rv1-shNRF2-1, and 22Rv1-shNRF2-3 cells treated with Brusatol (0.1 μM) for 24 h. n = 3.
(**H**) Flow cytometry analysis of intracellular labile Fe^{2+} levels using FerrOrange staining in 22Rv1-CD44hi-shCTR and 22Rv1-CD44hi-shCD44 cells treated with Brusatol (0.05 μM), with or without DFO (1 μM), for 72 h.
(**I**) Flow cytometry analysis of intracellular labile Fe^{2+} levels using FerrOrange staining in PC3-shCTR and PC3-shCD44 cells treated with Brusatol (0.1 μM), with or without DFO (1 μM), for 72 h.
(**J**) Flow cytometry analysis of lipid peroxidation using C11-BODIPY staining in 22Rv1-CD44hi-shCD44 cells treated with Brusatol (0.1 μM), with or without Liproxstatin-1 (5 μM) or DFO (1 μM), for 24 h. n=3.
(**K)** Flow cytometry analysis of lipid peroxidation using C11-BODIPY staining in PC3-shCTR and PC3-shCD44 cells treated with Brusatol (0.1 μM), with or without Liproxstatin-1 (5 μM) or DFO (1 μM), for 24 h.
(**L**) Cell viability measured by PrestoBlue assay in PC3-shCTR and PC3-shCD44 cells treated with Brusatol (0.05 μM), with or without Liproxstatin-1 (1 μM) or DFO (1 μM), for 72 h. n=3. Data are shown as mean ± SD. Statistical significance was determined by unpaired two-tailed t test or one-way ANOVA, as appropriate. *P < 0.05, **P < 0.01, ***P < 0.001, ****P < 0.0001.

Supplementary Figure 10



Supplementary Figure 10. Additional in vivo validation of Brusatol treatment and chromatin regulation of NRF2.

(**A**) Endpoint tumor volume in vehicle- and Brusatol-treated groups. Tumor volume was calculated as height × length × width × 0.8. n=5 mice per group.

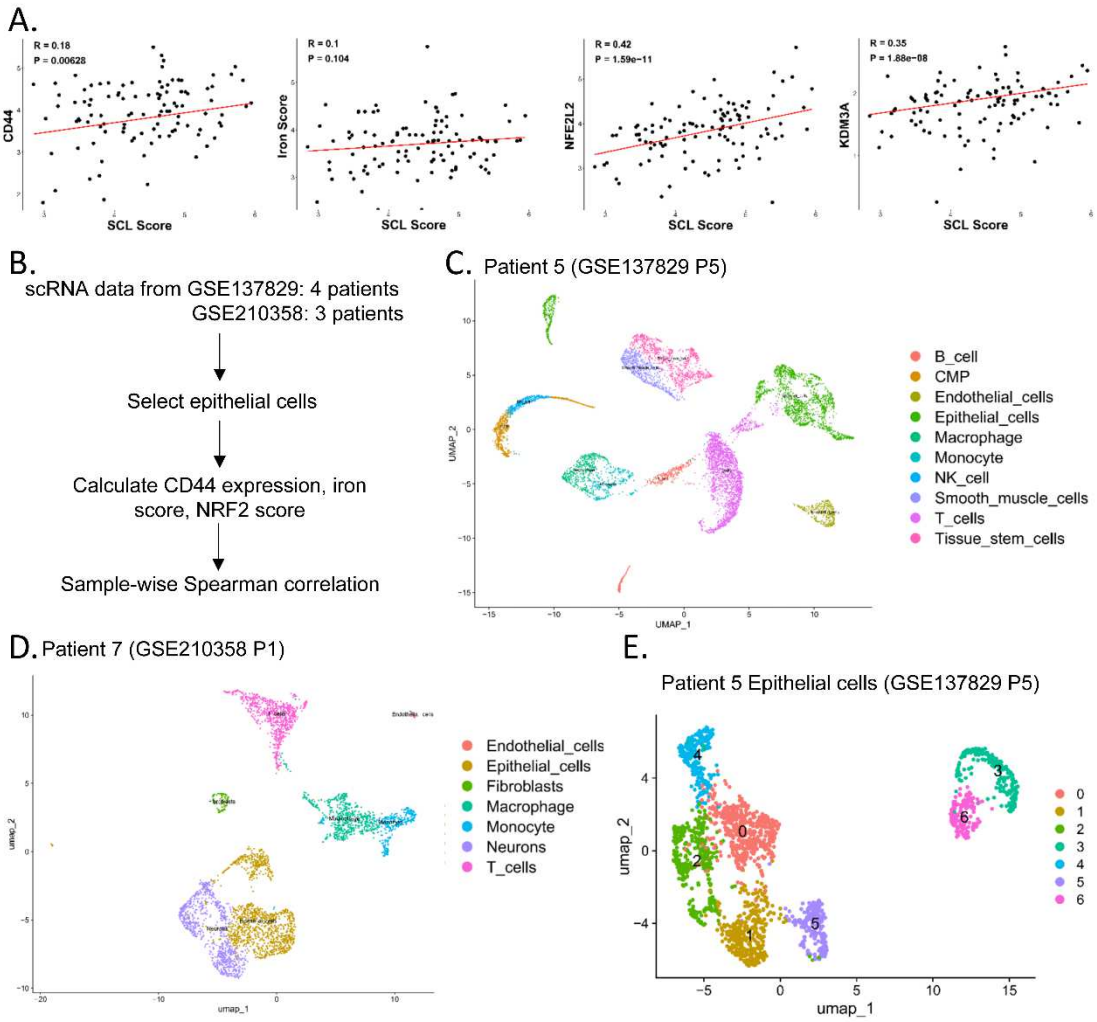
(**B**) Western blot analysis of CD44 and FTL protein levels in endpoint tumors from vehicle- and Brusatol-treated mice. Protein signals were quantified using ImageJ.

(**C**) ChIP-qPCR analysis of H3K9me2 occupancy at the NRF2 promoter in 22Rv1-CD44hi cells. Signals were normalized to input, and IgG was used as a negative control.

(**D–F**) ChIP-qPCR analysis of H3K9me2 enrichment at the NRF2 promoter in 22Rv1-CD44hi cells treated with CBA-1 (3 μM) for 72 h (**D**). qRT-PCR analysis of NRF2 mRNA expression (**E**) and Western blot analysis of NRF2 and H3K9me2 protein levels (**F**) in 22Rv1-CD44hi cells treated with CBA-1 for 72 h. CBA-1 was used at 2 μM for western blot analysis and 1 μM for qRT-PCR analysis.

(**G**) ChIP-qPCR analysis comparing H3K9me2 enrichment at the NRF2 promoter between 22Rv1-CD44hi and 22Rv1-CD44low cells.
(**H**) ChIP-qPCR analysis of KDM3A occupancy at the NRF2 promoter in 22Rv1-CD44low cells. Signals were normalized to input, and IgG was used as a negative control. CD44low cells were used for this comparison because KDM3A occupancy at the NRF2 locus was lower in this population, providing a more stringent assessment of signal above the IgG background.
(**I**) ChIP-qPCR analysis comparing KDM3A enrichment at the NRF2 promoter between 22Rv1-CD44hi and 22Rv1-CD44low cells. Data are shown as mean ± SD. Statistical significance was determined by unpaired two-tailed t test or two-way ANOVA, as appropriate. *P < 0.05, **P < 0.01, ***P < 0.001, ****P < 0.0001.

Supplementary Figure 11



Supplementary Figure 11. Patient cohort correlations and single-cell annotation workflow in CRPC/scRNA-seq analyses.

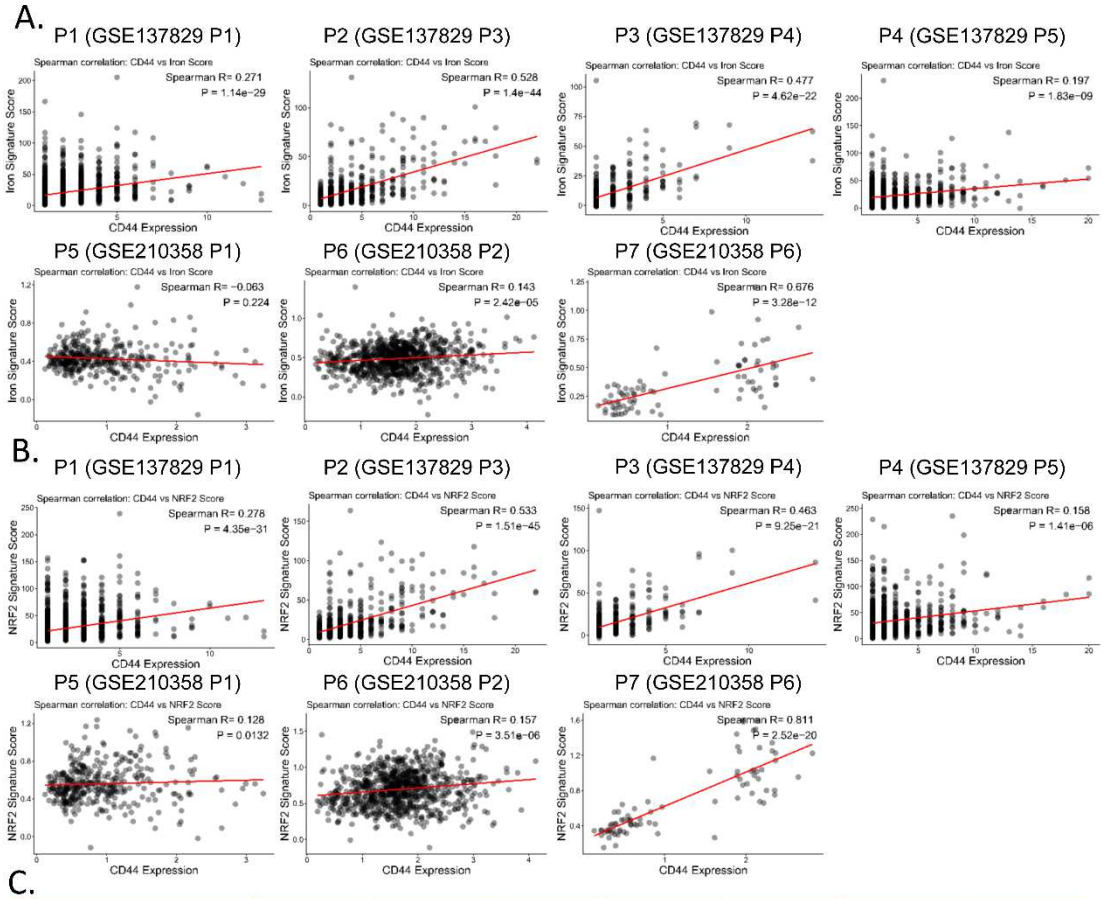
(**A**) Spearman correlation analyses in the DKFZ prostate cancer cohort (n = 242) showing associations between SCL score and CD44 expression, iron score, NFE2L2/NRF2 expression, and KDM3A expression. CD44 was excluded from the SCL and iron scores to avoid circularity.

(**B**) Schematic workflow for scRNA-seq analysis of CD44 correlations with iron and NRF2 scores in CRPC patient samples.

(**C-D**) UMAP visualization of major cell types from CRPC patient 5 in GSE137829 (**C**) and CRPC patient 1 in GSE210358 (**D**), analyzed using the Seurat workflow. Cell types are shown by color.

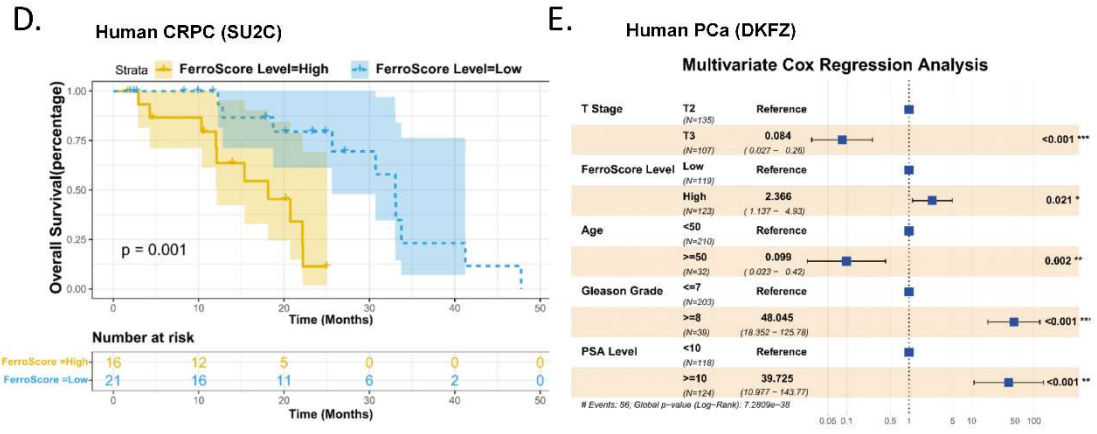
(**E**) UMAP visualization of epithelial cells from CRPC patient 5 in GSE137829. Epithelial cell clusters are shown by color. Data are shown as mean ± SD where applicable. Statistical significance was determined by Spearman correlation analysis, as appropriate. *P < 0.05, **P < 0.01, ***P < 0.001, ****P < 0.0001.

Supplementary Figure 12



C.

Patients		P1	P2	P3	P4	P5	P6	P7
Iron Score	P	1.142067e-29	1.404952e-44	4.620747e-22	1.826999e-09	2.241281e-01	2.422736e-05	3.277745e-12
	Rho	0.27139940	0.52757050	0.47681390	0.19676660	-0.0630	0.14318090	0.67577630
NRF2 Score	P	4.349395e-31	1.510164e-45	9.253832e-21	1.408497e-06	1.315002e-02	3.51e-06	2.52e-20
	Rho	0.27792760	0.53257500	0.46322100	0.15841850	0.12812120	0.157430	0.81112530



Supplementary Figure 12. Additional single-cell correlation and survival analyses supporting the clinical relevance of FerroScore.
(**A–B**) Per-sample Spearman correlation analyses between CD44 expression and iron score (**A**) or NRF2 score (**B**) in epithelial cells from seven CRPC scRNA-seq patient samples, including four from GSE137829 and three from GSE210358. Each panel shows the within-sample relationship between CD44 expression and the indicated score.

(**C**) Summary table listing Spearman correlation coefficients and P values for CD44-iron score and CD44-NRF2 score correlations across all seven patient samples.
(**D**) Kaplan-Meier analysis of overall survival based on FerroScore quartiles. Among 75 cases with complete survival data, 37 cases remained after top/bottom quartile stratification. For this exploratory analysis, the coefficients of the same seven-gene panel were re-estimated within the SU2C cohort using overall survival as the endpoint, therefore, this analysis does not represent external validation of the TCGA-derived FerroScore. P values were calculated by log-rank test.
(**E**). Multivariate Cox regression analysis for Gleason grade, PSA level, age, and T stage. FerroScore was calculated using the coefficients derived from the TCGA cohort and applied to the DKFZ dataset (n=242) without refitting. FerroScore was evaluated as a dichotomous variable, with patients stratified into FerroScore-high and FerroScore-low groups using the cohort-specific median as the cutoff, remained significantly associated with worse biochemical recurrence (HR 2.37, 95% CI 1.14–4.93, P = 0.021). Data are shown as mean ± SD where applicable. Statistical significance was determined by Spearman correlation analysis, multivariable Cox regression and log-rank test, as appropriate. *P < 0.05, **P < 0.01, ***P < 0.001, ****P < 0.0001.

Supplementary Table 1 List for scRNA-seq CRPC patients

Patients	Database	Patient Number	Patient ID
Patient 1 (P1)	GSE137829	Patient 1	GSM4089151_P1
Patient 2 (P2)		Patient 3	GSM4089153_P3
Patient 3 (P3)		Patient 4	GSM4089154_P4
Patient 4 (P4)		Patient 5	GSM4711414_P5
Patient 5 (P5)	GSE210358	Patient 1	GSM6428952_1778
Patient 6 (P6)		Patient 2	GSM6428953_1779
Patient 7 (P7)		Patient 6	GSM6428958_2284

Supplementary Table 2 Gene List for Signature Score

Signature Score	Gene List
Iron Score	"FTH1", "HMOX1", "TFRC", "SLC40A1", "CD44", "NCOA4","HAMP"
SCL Score	"FOSL2", "CD44", "ATF3", "ATXN1", "TACSTD2"
AR Score	"AR","DHCR24", "KLK3", "KLK2","NKX3-1","FOXA1"
Wnt Score	"TCF7L2", "KLF4", "SOX4", "SNAI1", "TCF7", "KLF2", "AXIN2", "RNF43", "CTNNB1"
NE Score	"NEUROD1", "ASCL1", "TCF12", "MYOG", "MSC", "NHLH1", "CHGA", "CHGB", "SCG3", "CHRNB2", "SYP", "ENO2", "SCN3A"
NRF2 Score	"NQO1", "FTL","FTH1", "CAT", "NFE2L2","HMOX1","HMOX2"

Supplementary Table 3 SCL and Iron Signature Application

Signature	Original gene set	CD44-independent version	Application
SCL	FOSL2, CD44, ATF3, ATXN1, TACSTD2	FOSL2, ATF3, ATXN1, TACSTD2	CD44-correlation analyses
Iron	FTH1, HMOX1, TFRC, SLC40A1, CD44, NCOA4, HAMP	FTH1, HMOX1, TFRC, SLC40A1, NCOA4, HAMP	CD44-correlation analyses

Supplementary Table 4 FerroScore Coefficient

Gene	Coefficient	HR
CD44	-0.10357	0.901613
FTL	-0.41237	0.662082
FTH1	0.196701	1.21738
SLC11A2	-0.77286	0.46169
HMOX1	0.478134	1.613062
NFE2L2	-0.98627	0.372966
KDM3A	1.186945	3.277055

Supplementary Table 5 Concentration for DFO, IOX1 and CBA-1

Reagent	Model	Experiments	Concentration	Duration	Figure
DFO	22Rv1/PC3	WB/qPCR	10uM	72h	Fig 3E-F, S.Fig 7D-H
DFO	22Rv1	ChIP-qPCR	20uM	72h	Fig 3G
DFO	22Rv1 (3D)	Organoid	30uM	72h	S.Fig 4L
DFO	22Rv1 (3D)	Organoid	50uM	72h	S.Fig 4J
DFO	LAPC9	RNA-seq/Org	60uM	4 days	Fig 4G
DFO	22Rv1	FACS/WB	5uM	24h/72h	Fig 5A/C
DFO	22Rv1/PC3	Rescue ferroptosis	1uM	24h/72h	Fig 6I, J and K; S.Fig 9H-L
IOX1	22Rv1	qPCR/FACS	100uM	72h	S.Fig 4B-C
IOX1	22Rv1(3D)	Organoid	150uM	72h	S.Fig 4K
CBA-1	22Rv1	WB	2uM	72h	S.Fig 4E
CBA-1	22Rv1	qPCR	1uM	72h	S.Fig 4F
CBA-1	22Rv1	ChIP-qPCR	3uM	72h	S.Fig 4G
CBA-1	22Rv1(3D)	Organoid	30uM	72h	S.Fig 4J
CBA-1	22Rv1(3D)	Organoid	50uM	72h	S.Fig 4M
CBA-1	LAPC9	RNA-seq/Org	15uM	4 days	Fig 4G

Supplementary Table 6 Antibody for Western Blot

Antibody	Company	Cat.No	Dilution
Actin	Cell signaling	4967	1:2000
CD44	BioTechne	BBA10	1:1000
c-MYC	Cell signaling	9402	1:1000
Ferritin light chain (FTL)	Proteintech	10727-1-AP	1:1000
H3K9me2	Cell signaling	4658S	1:1000
H3 Histon Antibody	Abcam	ab1791	1:2000
KDM3A	Proteintech	12835-1-AP	1:1000
NRF2	Proteintech	16396-1-AP	1:1000
SLC7A11	Proteintech	26864-1-AP	1:1000
GPX4	Abcam	ab125066	1:1000
NCOA4	Novus Biologicals	NBP3-18136	1:1000
Vinculin	Cell Signaling	4650S	1:1000
Anti-Rabbit IgG, HRP-Linked Ab	Cell signaling	7074	1:2000
Donkey anti-mouse IgG (H+L), HRP	ThermoFisher	A16011	1:2000

Supplementary Table 7 Primer for qPCR

Genes	Forward (5’-3’)	Reverse (5’-3’)
Actin	GCACAGAGCCTCGCCTT	CCTTGCACATGCCGGAG

CAT	AGGGGCCTTTGGCTACTTTG	ACCCGATTCTCCAGCAACAG
CD44	GACAAGTTTTGGTGGCACG	CACGTGGAATACACCTGCAA
FTH1	CATCAACCGCCAGATCAAC	GATGGCTTTCACCTGCTCAT
FTL	GCACGGACCCCCATCTCTG	GGCTCAGAAGGCTCTTAGTCG
GCLC	TGCCTATGTGGTGTTTGTGGT	ACCACTGCATTGCCACCTTT
HMOX1	GACGGCTTCAAGCTGGTGAT	GCTGGTGTGTAGGGGATGAC
HPRT	AGACTTTGCTTTCCTTGGTCAGG	GTCTGGCTTATATCCAACACTTCG
NQO1	TGGAGTCCCTGCCATTCTGA	ACTGCCTTCTTACTCCGGAAGG
NRF2	AGGTTGCCCACATTCCCAAA	ACGTAGCCGAAGAAACCTCATT
CD44 Chip 1	ttacagcctcagcagagcac	gagcgaaggacacacccaag
CD44 Chip 2	tgacaggccatcagtagctt	ccaagtggaaagagggagagc
CD44 Chip 3	ctgggtaggaaagatgggaga	tccattctctcatccaccca
CD44 Chip 4	tagcaccccaaacacacaca	atcttcagagccctcaccct
CD44 Chip 5	gtcacacaactaagaagcagcc	agtcatccacaggcagtacag
NRF2 Chip 1	gctaaaccaaatgccaaacagc	atgctgcaatttgctgagagtg
NRF2 Chip 2	tgcagggttttcacataacagc	tgcataatttgacactcccagg
NRF2 Chip 3	cgctttggtgggaagaggtt	caaacggagaagccccttttagg
NRF2 Chip 4	agttcagaggagggcgttca	taaagatttggacccagaccgt
NRF2 Chip 5	agctcctacaccaacgcctt	cgcccgcgagataaagagtt

Supplementary Table 8 Antibody for IHC and IF

Antibody	Company	Cat.No	Dilution
AR	Abcam	ab133273	1:100
CD44	BD Pharmingen	550988	1:100
EpCAM	R&D Systems	AF960	1:300
H3K9me2	Cell signaling	4658S	1:200
NRF2	Proteintech	16396-1-AP	1:100
4-HNE	Novus Biological	NBP2-59353	1:100
IgG Goat	Vector Laboratories	I-1000-5	1:1000
IgG Mouse	Vector Laboratories	I-2000-1	1:300
IgG Rabbit	Vector Laboratories	I-1000-5	1:400
AF488 donkey anti-rabbit	Life technolgoies	A21206	1:250
AF555 donkey anti-mouse	Life technolgoies	A31570	1:250

	AF647 donkey anti-goat	Life technolgoies	A21447	1:250

1802

Supplementary Files

This is a list of supplementary files associated with this preprint. Click to download.

- MCv2SupplementaryUncroppedGelsandBlots.pdf